# STUDY ON NOVEL COMPOSITE STRUCTURAL SUPERCAPACITORS WITH EXCELLENT MECHANICAL AND ELECTROCHEMICAL PERFORMANCE

**ZHANG JING**

**PhD**

**The Hong Kong Polytechnic University**

**2026**

**The Hong Kong Polytechnic University**

**Department of Applied Physics**

# Study on Novel Composite Structural Supercapacitors with Excellent Mechanical and Electrochemical Performance

**ZHANG Jing**

**A thesis submitted in partial fulfilment of the requirements for the degree of Doctor of Philosophy**

**Aug 2025**

# CERTIFICATE OF ORIGINALITY

I hereby declare that this thesis is my own work and that, to the best of my knowledge and belief, it reproduces no material previously published or written, nor material that has been accepted for the award of any other degree or diploma, except where due acknowledgement has been made in the text.

_____ (Signed)

ZHANG Jing (Name of student)

# Abstract

Composite structural supercapacitors (CSSs) are essential and promising multifunctional materials in a wide range of weight- and volume-reduced electric vehicles and aircraft, as they exhibit both good mechanical and electrochemical properties in a single unit. However, the study of CSSs is predominantly hindered by maintaining good mechanical and electrochemical performance simultaneously under extensive and extreme application conditions.

Research on the effect of electrochemical cycling on structural failure, particularly under applied loads, remains limited for CSSs. The electrochemical cycling-induced fatigue (electro-fatigue) failure and mechano-electrochemical coupling performance were investigated in a Zn-ion-based hybrid composite structural supercapacitor. Zn ion concentration gradient during the charge and discharge process induces alternating stress, which can be equivalent to a mechanical fatigue stress. The electro-fatigue stress gives rise to structural failure and a reduction in electrochemical performance. Moreover, for CSSs, coupling electro-fatigue stress with constant external stress results in an increased fatigue stress, significantly accelerating structural failure. These findings offer valuable insights and strategies to concurrently preserve superior electrochemical and mechanical integrity.

To enhance the electrochemical capacitance and mechanical strength of CSS, a special structure of the electrode and electrolyte interface was designed. The energy unit with the snap-on buckle structure of electrode and hydrogel electrolyte interface is integrated into a complex matrix to enhance the interlock effect. Strong bonding between the electrode and electrolyte is crucial for maintaining excellent

electrochemical performance under mechanical bending by minimizing shear movement between layers. Practical applications also indicate that the unique structure enables a new design of composite structural devices.

Under external forces, the deformation of CSSs results in an uneven distribution of electric field intensity, potentially compromising both electrochemical performance and mechanical performance. An MXene-based electrolyte for Zn-ion-based hybrid CSS was fabricated to effectively modulate the electric field distribution through a polarized electric field formed by hydrogen bonds between MXene and polymer chains. Integrating MXene into the electrolyte potentially paves the way for the design of high-performance structural power sources capable of functioning under deformation.

Low-temperature applications pose significant challenges due to electrolyte freezing and external force-induced deformation. To overcome these limitations, composite structural hybrid supercapacitors (CSSs) with enhanced mechanical strength and electrochemical performance at low temperatures were fabricated using a robust, freezing-resistant solid electrolyte. An unconventional Hofmeister effect of chaotropic $ClO_4^-$ anions was observed in anti-freezing ethylene glycol (EG)-polymer, leading to simultaneous enhancements in the stiffness and toughness of the polymer composite. The formation of strong and long hydrogen bonding (SHB) among $ClO_4^-$, EG, and the polymer matrix makes the material stiff and tough. Benefiting from the superior freeze resistance and mechanical strength, the fabricated CSS demonstrates exceptional electrochemical stability. Furthermore, this investigation deepens our understanding of CSS operation under both mechanical impact and subzero conditions, establishing design principles for CSS applications.

Overall, this thesis focuses on the balance of electrochemical and mechanical performance of CSSs under practical and extreme application conditions. Through structural design or modification, satisfactory results are obtained, paving the way for the design and development of CSSs.

# List of Publications

1. **Jing Zhang**, Ke Fan, Sha Yin, Hao Li, Huangxu Li, Junming Cao, Yulun Wu, Qian Cheng, Tiancheng Liu, Limin Zhou [*], Haitao Huang [*]. Unconventional Hofmeister Effect in Stiff and Tough Electrolyte with Strong Spring-Like Hydrogen Bonding for Multifunctional Composite Structural Hybrid Supercapacitors Working at -20 ℃. ***Advanced Energy Materials.*** **Published, https://doi.org/10.1002/aenm.202502761.**

2. **Jing Zhang**, Zihan Hu, Anchalee Duongthipthewa, Hanmo Zhou, Sha Yin, Junyi Yu, Hao Li, Xi Gong, Haitao Huang[*], Limin Zhou[*]. Electrochemical cycling-induced fatigue failure in all-solid-state composite structural supercapacitors under applied loads. ***Composites Science and Technology.*** **Under review.**

3. **Jing Zhang**[#], Liqi Bai[#], Junyi Yu, Gao Chen, Hao Li, Sha Yin, Yongbo Fan, Anchalee Duongthipthewa, Zezhou Lin, Qingqing Wang, Haitao Huang[*], Limin Zhou[*]. Stabilizing the Spatial Distribution of Electric Field by MXene-Based Electrolyte Additions for High-Performance Composite Structural Supercapacitors. ***Advanced Functional Materials*****. Under review.**

4. **Jing Zhang**, Hu Zihan, Hanmo Zhou, Zezhou Lin, Hao Li, Limin Zhou[*], Haitao Huang[*]. Novel High-Strength Composite Structural Supercapacitors Based on a Snap-On Buckle Electrode/Electrolyte Interface Structure Fabricated via In-Situ Polymerization to Enhance Interface Performance Under Load-Bearing. **Preparing for submission.**

5. **Jing Zhang**, Anchalee Duongthipthewa, Hanmo Zhou, Sha Yin, Junyi Yu, Hao Li,

Xi Gong, Haitao Huang*, Limin Zhou*. Self-healing Composite Electrolyte realize electrochemical performance recovery of multifunctional composite supercapacitors under applied loads. **Preparing for submission.**

6. Hanmo Zhou, Yiyin Su, **Jing Zhang**, Hao Li, Limin Zhou*, Haitao Huang*. A Novel Embedded All-Solid-State Composite Structural Supercapacitor Based on Activated Carbon Fiber Electrode and Carbon Fiber Reinforced Polymer Matrix. ***Chemical Engineering Journal***, **2023**, 454, 140222.

7. Hanmo Zhou, Anchalee Duongthipthewa, **Jing Zhang**, Hao Li, Luwei Peng, Yu Fu, Haitao Huang*, Limin Zhou*. A composite structural supercapacitor based on Ni-Co-layered double hydroxide–coated carbon cloth electrodes. ***Composites Science and Technology***, **2023**, 240, 110068.

8. Hanmo, Zhou, **Jing Zhang**, Jiannan Ren, Xinyu Fan, Xing Wang, Chengce Yuan, Jiaxin He, Anchalee Duongthipthewa, Haitao Huang*, and Limin Zhou*. "A load-bearing/energy-storage integrated composite structural supercapacitor based on carbon nanotubes modified carbon fibers. ***Composites Communications*** 54 (2025): 102261.

9. Gong, Xi, Hao Li, Ke Fan, Zezhou Lin, **Jing Zhang**, and Haitao Huang. Mo2CT x Supported Ruthenium Nanoparticles as Efficient Cathode Catalyst for Li-CO2 Battery with High Capacity and Long Cycle Life. ***Chemical Research in Chinese Universities*** (2025): 1-8.

10. Qingqing WANG, Anchalee Duongthipthewa, Ruiyuan Zhang, Xu Liu, Jing Zhang, Xiating Li, Yiyin Su, Menglong Liu, Zhongqing Su*, Limin Zhou*. Implantable Graphene/PVA-Coated Glass Fiber for Real-time Strain Monitoring

in Structural Batteries under Electrochemical Cycling and External Loading. ***Composites Part A***. **Accepted for publication.**

11. Anchalee Duongthipthewa, Qingqing Wang, Jing Zhang, Hanmo Zhou, Yuehua Liu, Sha Yin, Limin Zhou*. Real-Time Structural Monitoring and Functional Integration in FRP Composites Enabled by Reduced Graphene Oxide/MXene Ink-Coated Sensors. ***Advanced Composites and Hybrid Materials.*** **Under review.**

# Acknowledgements

Time flies by, and it's hard to believe that my four-year PhD journey is coming to an end. Looking back, I am grateful for the opportunities and experiences that the joint training program of the Southern University of Science and Technology and the Hong Kong Polytechnic University has provided me with. I have gained a lot of knowledge, developed my skills, and grown as a person.

I would like to take this opportunity to express my heartfelt gratitude to Professor Haitao Huang and Professor Limin Zhou, who have been my mentors throughout my PhD journey. Their support and guidance have been invaluable, and I am grateful for their encouragement, advice, and patience. They have been my beacon of light during my research journey, and their insights and wisdom have helped me to overcome many challenges and obstacles.

I am also grateful to my fellow researchers, especially to Hanmo Zhou, Gao Chen, Liqi Bai, Zihan Hu, Anchalee Duongthipthewa, Qingqing Wang, Hao Li, Xi Gong, Huangxu Li, Zezhou Lin, Tiancheng Liu, Yongbo Fan, Qian Cheng, Xiating Li and Yulun Wu. Your warm and friendly support, your willingness to share your knowledge and experiences, and your teamwork have made my research journey much easier and enjoyable. In addition, I would like to thank Dr. Gao Chen, Prof. Sha Yin, Dr. Liqi Bai, and Dr Hao Li for their suggestions and assistance. I could not have achieved my goals without your help.

I would also like to express my appreciation to all the laboratory teachers who have taught and guided me during my PhD journey. Their patience, expertise, and dedication have helped me to develop my experimental skills and have been

instrumental in my success.

Last but not least, I would like to thank my family, especially my parents. Their support and companionship have given me the strength and motivation to overcome challenges and pursue my dreams. I am grateful for the values and principles they have instilled in me, which have shaped who I am today.

In conclusion, I am honored to have had the opportunity to pursue my PhD degree, and I am grateful for all the support, especially the financial support of the Southern University of Science and Technology. And the help I have received from my mentors, colleagues, friends, and family. I hope to use the knowledge and skills I have gained to contribute to the society and make a positive impact on the world.

# Table of Contents

# List of Figures

**Figure 2.6** (a) photographs of quaternary ammonium functionalized polyvinyl alcohol (QUPA)/aramid nanofibers (ANFs) composite electrolyte membrane in different states. (b) Tensile strength values, Young's modulus, and elongation at break of QUPA/ANF with various ANF concentrations. (c) Comparison of ionic conductivity of the PVA, QUPA, and QUPA/ANF-2.0 membranes [71]. (d) Schematic illustration and measurements of ionic conductivity of composite electrolyte with various PEO/epoxy ratios. (e) A cross-sectional schematic of the electrolyte with gradient composition: the edge part electrode region had a higher concentration of salt and PEO than the middle part to enhance the device kinetics. (f) A nacre-like "brick-and-mortar" microstructure composite electrolyte with (g) enhanced Young's moduli

**Figure 5.8** The SEM images of the middle part (a, c) and edge part (b, d) of fractured three-point bending PAM-I-CSS and PAM-S-CSS devices. The SEM images of the middle area (e, g) and side area (f, h) of fractured PAM-I-CSS and PAM-S-CSS devices after a short beam test. (i) Shear stress profiles of the PAM-I-CSS and PAM-S-CSS devices. (j) The three-point bending test curves of the PAM-I-CSS and PAM-S-CSS devices. .....80

Moreover, the three-point bending test results highlight the importance of interfacial adhesion in determining the flexural strength of composite structures. The observed delamination, especially in the intralayer between the carbon fiber electrode and the hydrogel electrolyte, appears to be the governing failure mechanism after the three-point bending test in PAM-S-CSS, as exhibited in the middle area (Fig. 5.8e) and side area (Fig. 5.8f). High flexural strength is corroborated by the layers of the reinforcement unit (the matrix-fiber) in the middle part (Fig. 5.8g), along with the lack of obvious delamination between the electrode and electrolyte (Fig. 5.8h). This indicates that the locked structure between the carbon fiber electrode and the hydrogel electrolyte can affect load transfer in multiple layers, which fairly conforms to the simulation results, leading to higher mechanical strength of PAM-I-CSS. Moreover, the locked interface was too strong to be delaminated, which altered the main failure mechanism for the PAM-I-CSS. This enhanced the flexural stress and flexural modulus, which increased considerably from 282.21 MPa and 26.34 GPa, respectively,

The effect of the additive amount of MXene on the ionic conductivity of electrolytes was systematically investigated by preparing 0.00 wt.%, 0.01 wt.%, 0.02 wt.%, 0.03 wt.%, and 0.04 wt.% MXene-containing electrolytes. As illustrated in Fig. 6.4a, the electrolyte resistances tend to increase at first and then decrease with the increased content of MXene. When the addition of the MXene is 0.03 wt.%, the optimum ionic conductivity of the electrolyte is 23.5 mS $cm^{-1}$, attributed to the enhanced ion transport facilitated by MXene additives (Fig. 6.4b). The surface-terminating groups of MXene

# List of Tables

# Chapter 1 Introduction

## 1.1 Background and Research Motivation

The increasing requirement on energy density of the battery remains a critical challenge in the advancement of electric transportation, significantly influencing the mileage of electric vehicles and the industrialization of electric aircraft [1, 2]. A weight saving strategy is feasible for augmenting energy density, thereby inspiring research focus on multifunctional batteries [3, 4]. Consequently, composite structural energy storage devices (CSESDs) have drawn increasing interest across various fields as multifunctional energy storage devices [5]. CSESDs can effectively substitute traditional load-bearing components by simultaneously providing energy storage and structural support, thereby minimizing the overall mass of the device [6-8]. Thus, the CSESDs are essential for the development of volume- and weight-restricted applications such as electric vehicles, unmanned planes, and civil structures. Compared with composite structural batteries, composite structural supercapacitors (CSSs) demonstrate higher power density due to enhanced ion diffusion and more stable cycling performance, leading to a more suitable integrated structural system without unfeasible and undesirable frequent replacement [3]. This advantage makes CSSs a potential candidate for industrial applications.

The architectural strategies of CSSs can be broadly classified into two main approaches [5]. The first one is called cell-level design, which involves supercapacitors being sandwiched between reinforced carbon fiber composites [6-9]. Herein, the external reinforcement assumes a significant proportion of the load-bearing responsibilities without contributing to energy storage, while the

supercapacitor primarily functions as a power source and supports only minimal loads. For instance, Thomas et al. used a wet hand lay-up method to fabricate a carbon fiber (CF) laminate sandwich with LIB pouch cells embedded in a foam core and achieved a specific energy of 45 Wh $Kg^{-1}$ and a flexural rigidity of 985 N $m^{-2}$ [9]. It is believed that cell-level designs yield limited enhancements in multifunctional efficiency, as both supercapacitors and reinforcements operate in a monofunctional capacity. Consequently, the potential for weight reduction may be inherently constrained. Conversely, the second approach, a material-level design, integrates multifunctional materials that serve as both load-bearing structural components and power source elements into CSSs. These energy storage units, including all strong structural carbon fiber current collectors and electrodes, and solid-state electrolytes, are developed with enhanced mechanical performance [7, 10]. Despite the relatively enhanced mechanical properties for structural support, these structural materials should be developed without compromising electrochemical performance [8]. Carbon fibers (CFs) can serve as active materials and current collectors due to their high mechanical strength. For example, Asp et al. adopted CF as an active anode for structural batteries with a specific energy of 24 Wh $kg^{-1}$ and high modulus of 25 GPa [11]. Obviously, the material-level design more accurately embodies the essence of structural and multifunctional components, demonstrating superior potential for future development.

Given the inherent trade-offs between mechanical properties and electrochemical performance, one of the main challenges for CSSs lies in balancing the electrochemical performance and mechanical strength.

## 1.2 Research Objectives

Based on the above research background and existing limitations, the goal of this PhD thesis is to develop high-performance CSSs that integrate load-bearing capability and energy storage capacity. In addition, external mechanical load and low temperature are very crucial for their practical applications but have been less studied in previous reports. Driven by above goal, the research objectives of this thesis are:

1) to investigate the electrochemical cycling-induced fatigue (electro-fatigue) failure and mechano-electrochemical coupling performance.

2) to modify the electrode/electrolyte interface by snap-on structure to interlock the interface and to increase the structural stability under load bearing, and to characterize the in situ mechano-electrochemical performance of snap-on structure CSSs.

3) to decrease the influence of the deformation on the electrochemical properties of CSS through adding MXene in the solid electrolyte to uniform the electric field distribution.

4) to study the mechanical strength of CSSs at low temperature, by adding the chaotropic $ClO_4^-$ anions in solid electrolyte to form strong and long hydrogen bonds to increase the stiffness and toughness of CSSs at -20 ℃.

## 1.3 Scope of the Thesis

This thesis focuses on the research of CSSs, which are composed of flexible energy storage devices and carbon fiber reinforced polymer (CFRP). The research includes the preparation of different carbon fiber electrodes, the structural design, and the characterization of the mechanical and electrochemical properties of CSSs. In addition, the effects of external forces (both static and dynamic loads) on the electrochemical properties of CSSs are systematically studied. Through the optimization and modification of carbon fiber electrodes, composite electrolyte, and the electrode/electrolyte interface, CSSs exhibit increasingly superior mechanical strength and electrochemical capacity.

The thesis is organized as follows:

Chapter 1 points out the significance of composite structural energy storage devices (CSESDs) for future engineering applications and presents an overview of their development and existing defects. It further emphasizes that CSS is the main research object in this thesis and outlines the corresponding research objectives.

Chapter 2 mainly focuses on the development of CSESDs including the development of carbon fiber electrodes, structural separator designs and electrolyte, and the coupling effect of mechanical and electrochemical performance. Moreover, characterization approaches, such as in-situ mechano-electrochemical tests, and evaluation methods of multifunctionality are introduced.

Chapter 3 is the experimental methodology of this thesis, including materials, modification methods of carbon fiber electrodes, composite electrolyte, preparation of CSSs, and various characterization methods.

In Chapter 4, a Zn-ion-based hybrid composite structural supercapacitor incorporating a composite energy storage unit is introduced. The electrochemical cycling-induced fatigue (electro-fatigue) failure and mechano-electrochemical coupling performance were investigated. It is revealed that the Zn ion concentration gradient during the charge and discharge process induces alternating stress, which can be equivalent to a mechanical fatigue stress. The electro-fatigue stress gives rise to structural failure and a reduction in electrochemical performance. Moreover, for CSSs, coupling electro-fatigue stress with constant external stress results in increased fatigue stress, significantly accelerating structural failure. These findings elucidate the failure mechanism of CSSs caused by the cycling process, offering valuable insights and strategies to concurrently preserve superior electrochemical and mechanical integrity.

In Chapter 5, the snap-on structure is introduced to interlock the electrode/electrolyte interface, thereby preventing sliding between multiple layers in the energy unit. The improved adhesive bonding stabilizes the electrode layer stack mechanically and significantly contributes to load transfer without sacrificing electrochemical performance. The strong bonding in the electrode/electrolyte interface is crucial for maintaining excellent electrochemical performance under mechanical bending by minimizing shear movement between layers. The snap-on structure exhibits lower stress level in the electrode/electrolyte interface than the sandwich structure, attributed to the interlock interface that facilitates load transfer. Practical applications also indicate that the unique structure enables a new generation of composite structural devices, making them promising for use in electric vehicles, electric aircraft, and other fields.

In Chapter 6, an MXene-based electrolyte for Zn-ion-based hybrid CSS is introduced

to effectively modulate the electric field distribution through a polarized electric field formed by hydrogen bonds between MXene and polymer chains. Integrating MXene into the electrolyte offers a practical approach to regulating electric field distribution, potentially paving the way to design high-performance structural power sources capable of functioning under deformation.

Chapter 7 provides a composite structural hybrid supercapacitor (CSHS) with enhanced mechanical strength and electrochemical performance at low temperatures using a robust, freezing-resistant solid electrolyte. An unconventional Hofmeister effect of chaotropic $ClO_4^-$ anions was observed in anti-freezing ethylene glycol (EG)-polymer, leading to simultaneous enhancements in the stiffness and toughness of the polymer composite. The formation of strong and long hydrogen bonding (SHB) among $ClO_4^-$, EG, and the polymer matrix makes the material stiff and tough. Benefiting from the superior freeze resistance and mechanical strength, the fabricated CSHS demonstrates exceptional electrochemical stability. Furthermore, this investigation enhances the understanding of CSHS operation under both mechanical impact and subzero conditions, establishing design principles for CSHS applications.

Chapter 8 concludes all the research work on CSSs in the thesis. Guidance and prospects for future research directions are also proposed

# Chapter 2 A Review on Composite Structural Energy Storage Devices

The development of lightweight batteries holds significant potential for mobile applications, such as electric vehicles and electric aircraft. Specifically, multifunctional composite structural energy storage devices (CSESDs) are capable of bearing mechanical loads, replacing traditional structural components and contributing to a reduction in overall system weight (Fig. 2.1) [6, 12]. For example, structural batteries can serve as roofs of electric vehicles, reducing the corresponding mass by 20%.[1, 2].

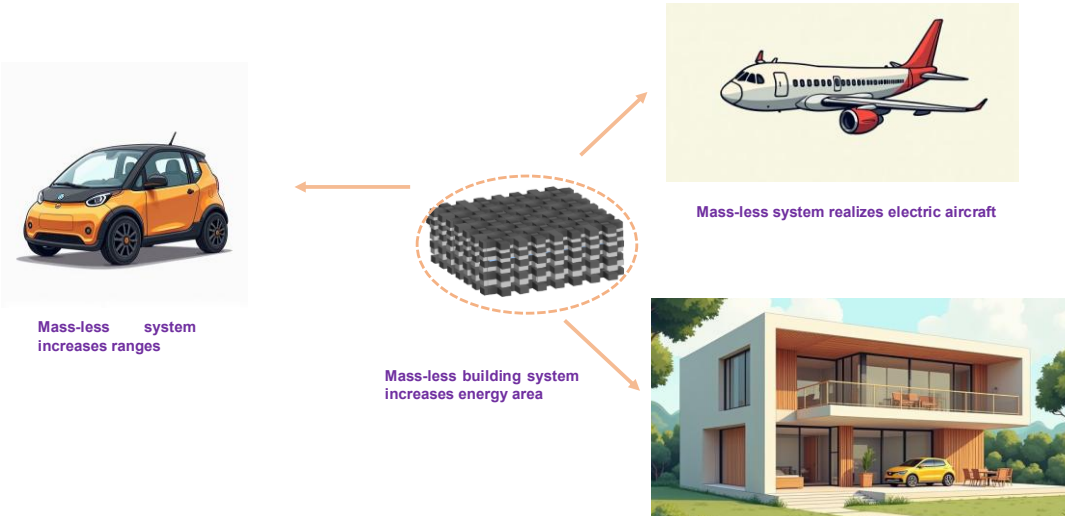


**Figure 2.1** (a) Various applications of CSESDs to save weight or increase energy storage at the system level.

To evaluate the mass or volume saving of CSESDs, the following equation can be used

as a guide:

$$Mass\ Reduction\ Ratio = \frac{m_{CFRP} + m_{ESD} - m_{CSESD}}{m_{CFRP} + m_{ESD}}$$

Where the $m_{CFRP}$ is the mass of a carbon fiber reinforced polymer composite (CFRP) used to provide the required mechanical strength. $m_{ESD}$ and $m_{CSESD}$ are the masses of an energy storage device and a structural composite energy storage device, respectively. The multifunctional efficiency was also generalized to point out that it simultaneously provides multiple mechanical and electrochemical properties, which can be defined as $\eta_{ME} = \eta_M + \eta_E$, where $\eta_{ME}$ is the multifunctional efficiency, $\eta_M$ is the mechanical efficiency, and $\eta_E$ is the electrochemical efficiency [4, 5]. Practically, $\eta_M$ is the ratio of the mechanical value (e.g., flexural modulus or strength) of the CSESDs to that of a CFRP, and $\eta_E$ represents the ratio of the electrochemical capacity of the CSESDs to that of an energy storage unit using liquid electrolyte under zero external load. The multifunctional energy storage devices offer a weight-saving benefit compared to the traditional monofunctional systems when the $\eta_{ME}$ value is greater than 1 [3, 13].

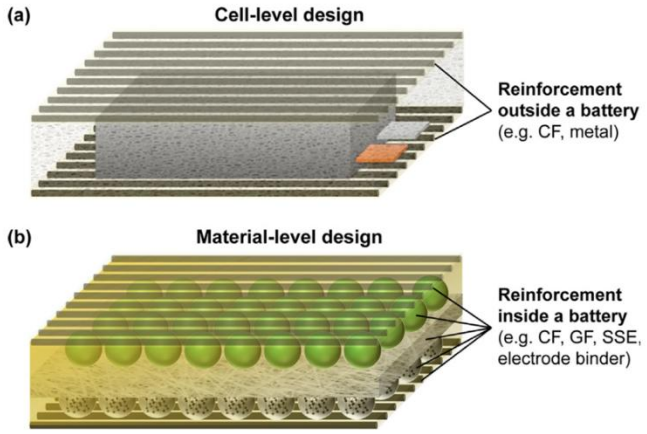


**Figure. 2.2** (a) cell-level designs and (b) material-level design [14].

The challenges for the CSESDs are how to balance excellent electrochemical performance and strong mechanical properties. The architectural structure of CSESDs can be classified into two categories: cell-level and material-level design (Fig. 2.2) [14]. The former refers to a sandwich structure in which supercapacitors are embedded between reinforced carbon fiber (CF) composites [6, 7, 10]. The external non-capacitive reinforced carbon fiber (CF) bears primary mechanical stress, whereas the internal energy storage device is subjected to only a minimal portion of the load. Thus, the multifunctionality of this strategy is limited. Nonetheless, due to its feasible and cost-effective fabrication process, an increasing number of cells are being effectively spatially distributed and directly integrated into the reinforcement, facilitating mass production for applications such as electric vehicles [14]. In contrast, the second approach utilizes multifunctional materials that incorporate structural current collectors, electrodes, and electrolytes, which also serve as load-carrying components and contribute to enhanced mechanical performance [8]. In this design, the challenge lies in avoiding a compromise in electrochemical performance [14]. Several methods can be used to improve the electrochemical performance. For instance, an all-carbon-fiber-based structural lithium-ion battery can achieve a high energy density of 75 Wh $kg^{-1}$ and an elastic modulus of 76 GPa [15]. Therefore, material-level design represents a promising approach to achieving both structural and multifunctional components.

## 2.1 Fabrication methods of structural composite energy storage device

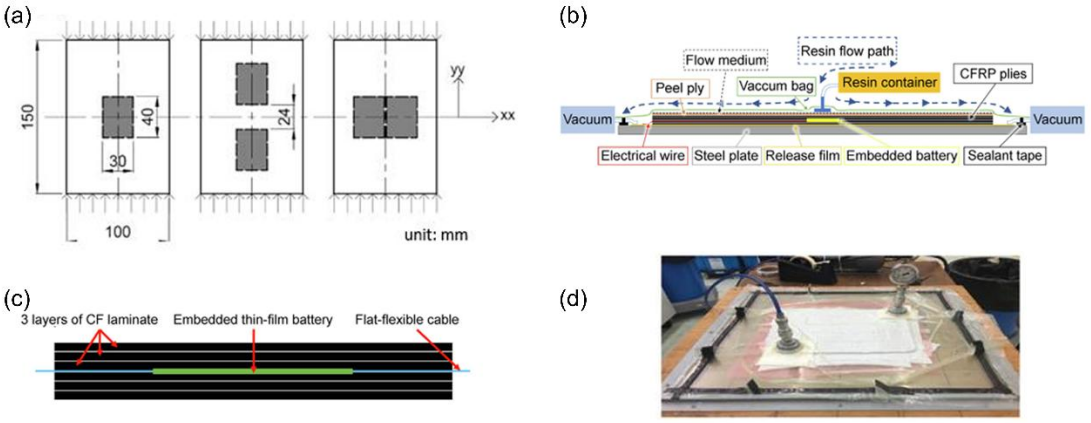


**Figure 2.3** The fabrication process of the CSESDs. (a) The layouts of the laminate system incorporating the lithium cells [16]. (b) A schematic illustration of the manufacturing of a structural lithium-polymer battery by the vacuum bag resin infusion (VBRI) technique [17]. (c) The principle of embedding a thin-film battery in cut-outs of CF laminates [14]. (d) A wet lay-up method under vacuum conditions [18].

CSESDs can be fabricated using traditional wet lay-up composite manufacturing techniques, which are conducted at room temperature under vacuum conditions, thereby safeguarding the temperature-sensitive electrodes and electrolytes [9, 17, 19-23]. The layouts with the laminate system incorporating the lithium cells can be designed with different structures (Fig. 2.1a) [16]. As shown in Fig. 2.3b, the Li-polymer cells containing liquid electrolyte were embedded in the cut-outs of CF laminates using the wet hand lay-up method and subsequently cured using the vacuum bag resin infusion (VBRI) technique at 20 °C for 24 hours [17]. The principle of the VBRI strategy is illustrated in Fig. 2.3c [14]. This strategy can be applied at a practical

scale and avoids damage to the energy storage unit. The CSESDs fabricated by this method simultaneously exhibit high mechanical and electrochemical properties. For example, Thomas et al. embedded lithium-ion batteries in CF laminate sheets, obtaining a rigid structural battery with a specific energy of 45 Wh kg-1 and a flexural strength of 985 N m-2 [19]. Pattarakunnan et al. subsequently incorporated five pouch cells in a sandwich structure with a specific energy of 94 Wh kg-1 [17]. To reduce the overall weight, a structural battery was fabricated using this modified encapsulation strategy, employing CF laminate sheets as both reinforcement and battery packaging. A weight reduction of 5-10 wt.% was achieved due to the elimination of additional packaging weight [9]. A wet lay-up method was employed to fabricate CSESDs under vacuum conditions at ambient temperature (Fig. 2.3d) [18]. Humidity and air bubble disturbances must be avoided during the curing process. This strategy may compromise the mechanical properties of the entire system, as the energy unit may become defects introduced into the system.

## 2.2 Carbon fiber-based materials

Carbon fibers can serve as the active material or the current collector. In the case of the active material, the turbostratic microstructure of the CF anode facilitates the intercalation of Li-ions during both radial and longitudinal expansions [24]. Throughout the lithiation and delithiation processes, the longitudinal elastic modulus of the fiber decreased from 290 GPa to 255 GPa, and subsequently recovered completely. In contrast, the transverse modulus exhibited a reversible increase from 7.6 GPa to 15 GPa [25]. Modern polyacrylonitrile (PAN) demonstrates high mechanical strength, with Young's moduli ranging from 250 to 600 GPa and a tensile strength of 4 to 7 GPa for a single fiber [26].

When evaluating the electrochemical performance of CFs, their specific capacities exhibit significant variation, ranging from 22 to 358 mAh $g^{-1}$. This variation is governed by factors such as fiber structure, surface area, and treatment methods [27]. Simultaneously maintaining both high electrochemical and mechanical properties is crucial for the design of CF-based electrodes. For instance, Asp et al. fabricated a CF anode with a natural surface, which exhibited a specific energy of 24 mAh $g^{-1}$ and a high modulus of 25 GPa [11]. Moyer et al. reported that the energy density of a CF anode with a graphite coating was improved to 35 mAh $g^{-1}$, while the Young's modulus and tensile strength were decreased due to the presence of liquid electrolyte [28].

In addition to serving as an anode, CFs can also function as current collectors in CSESDs due to their high electrical conductivity of $10^2$-$10^3$ S $cm^{-1}$ [29]. Electrophoretic deposition and coextrusion of CFs with an LFP-doped matrix [30] represent the primary strategies for producing the adhesive $LiFePO_4$ (LFP)@CFs [31]. An additional polyacrylonitrile (PAN) layer can be employed to bridge the active material and the polymer matrix, thereby enhancing the interfacial adhesion of LFP particles to the CF surface [32]. Besides, Nickel sulfides [33], polysulfides [34], or $LiMn_{0.97}Al_{0.03}O_2$ [35] deposited on CFs have also been reported to function as structural electrodes. The enhanced adhesion resulting from the electrodeposition of polysulfide onto CFs effectively mitigates the risk of delamination between the active materials and the substrate under mechanical stress [32]. A structural lithium-sulfur (Li-S) battery, incorporating a molten lithium-infused CF anode and a $Li_2S_8$/CF cathode, achieved a specific energy of 43 Wh $kg^{-1}$, calculated based on the total mass of the battery components [36]. Chen et al. designed structural Zn-ion batteries (ZIB)

containing $MnO_2$@CF cathode and Zn@CF anode, demonstrating a specific energy of 182 Wh $kg^{-1}$, calculated based on the mass of active materials [37]. The elastic modulus and capacity were summarized in Table 1.

Various techniques such as vacuum deposition, magnetron sputtering, and electron-beam evaporation were used. As shown in Fig. 2.4a, Jiang et al. designed a composite electrode through arraying $Co_3O_4$-NC nanoflakes on the carbon fiber cloth hosts to avoid Li metal dendrite growth [38]. An individual CF-based structural battery with single carbon fiber, in which the cathode, electrolyte, and anode were sequentially coated, was first introduced (Fig. 2.4b) [39]. Chaudhary et al. developed an all-carbon fiber-based structural battery by employing the carbon fiber's multifunctionality of storing energy and providing strength (Fig. 2.4c) [15]. A pristine carbon fiber negative electrode, a lithium iron phosphate (LFP)-coated carbon fiber positive electrode, and a thin cellulose separator were integrated into a structural battery and cured to demonstrate an energy density of 30 Wh $kg^{-1}$ and an elastic modulus exceeding 76 GPa [15]. In Fig. 2.4d, the individual structural LIB with a single fiber was printed through UV-assisted coextrusion deposition of CFs and doped functional photopolymer resin [40].

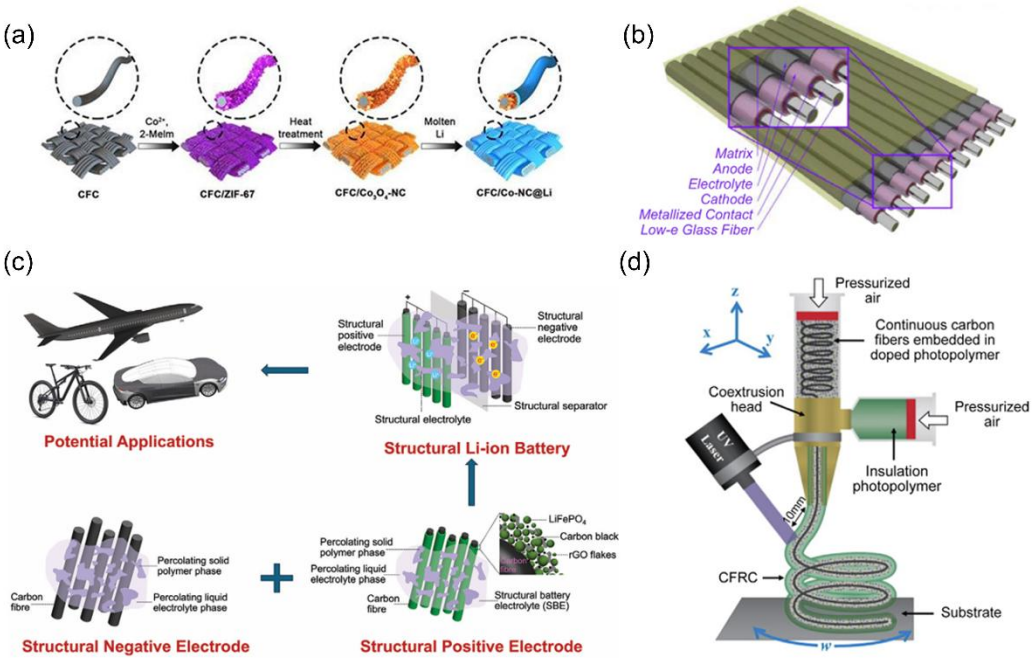


**Figure 2.4** Individual CFs with thin-film battery coating for structural battery design. (a) The manufacturing process of CFC/Co-NC@Li composite electrode [38]. (b) Structural battery with single CFs-based structural electrode and electrolyte [39]. (c) A schematic structure of all-fiber structural batteries utilizing the pristine carbon fiber as negative electrode, lithium iron phosphate (LFP)-coated carbon fiber as positive electrode, and a thin cellulose separator [15]. (d) Individual CF-based micro-battery cell produced by coextrusion deposition [40].

**Table 2.1** Elastic modulus and capacity of structural electrodes.

| Materials | Specific capacity | Elastic modulus | Ref. |
|---|---|---|---|
| $Li_2MnO_4$@CF film | 80.7 mAh $g^{-1}$ | 13.6 GPa | [41] |

| | | | |
|---|---|---|---|
| $LiFePO_4$@CF | 32 mAh $g^{-1}$ | 2.4 GPa | [42] |
| Si-CNT fabric | 500 mF·$g^{-1}$ | 18.7 GPa | [43] |
| 3D-architected carbon | 131 mAh $g^{-1}$ | NA | [44] |

The mechanical properties of separators also need to be significantly enhanced without compromising electrochemical performance to achieve high multifunctional efficiencies. The structural vertically aligned nanofiber separator (VANS), serving as both structural reinforcement components and ionic transport channels in energy device, was developed by electrically insulating aligned alumina nanotubes (Fig. 2.5a-b) [45].

In addition to enhancing individual layer components containing electrodes, separators, and binders, Jin et al. proposed that the interfacial structure plays a crucial role in improving the flexural and shear stiffness of the whole system. They employed coating and hot-pressing methods to design a bio-inspired tree-root-like poly(vinylidene fluoride-co-hexafluoropropylene) (P(VdF-HFP)) binder to tightly adhere the separator and porous electrode (Fig. 2.5c) [33]. As shown in the left inset of Fig. 2.5d, this interfacial structure enhances the flexural modulus of the structural battery compared to that without this adhesion. This structural battery also exhibits high capacity retention of 95% after 500 cycles (Fig. 2.5d). This interfacial PVdF-HFP binder enables the practical application of graphite/NMC532 cells to function as the

electrically powerful wings for a UAV model, because of the high flexural modulus (Fig.2.5d, right inset).

New binders also need to be rationally designed to enhance the mechanical properties of CSESDs. Various binders can strongly adhere electrode particles together and to current collectors, making them the promising candidate components for CSESDs [46]. For example, sodium alginate [47], lithium substituted poly(acrylic acid) (PAA) [48], gelatin and konjac glucomannan [49-54] were proposed as the robust binders. Some binders, such as polyacrylonitrile (PAN) and sodium alginate, have high mechanical strength to maintain electrochemical functionality under external loads [55, 56]. Furthermore, Valentini et al. proposed that ANF could serve not only as a separator material but also as a promising binder for structural electrodes. The reduced graphene oxide (rGO)/ANF composite they designed has a tensile modulus of 13 GPa, which is attributed to their high intrinsic mechanical properties resulting from the extensive hydrogen bonding, which enable the load transfer [56]. Ultra strong ANFs were synthesized through a direct and controllable method [48, 50, 51, 54, 57, 58]. Patel et al. produced ANF-based separators using a straightforward vacuum filtration technique, rather than an intensive synthesis, to prepare ANF separators without modification or additives, as shown in Fig. 2.5e [54]. The ANF-based separator displays a high Young's modulus (8.8 GPa) (Fig. 2.5f), but shows low capacity and cycling stability due to the low ion transportation resulting from the small pore size (Fig. 2.5g). These results suggest that ANF-based separators can be the promising alternatives for the traditional separators in CSESDs. Wang et al. further fabricated the ANF separators to enlarge the pores while maintaining a Young's modulus at 2.8 GPa, which outperforms Celgard 2400 separators in cycling performance of lithium or

sodium ion batteries [59].

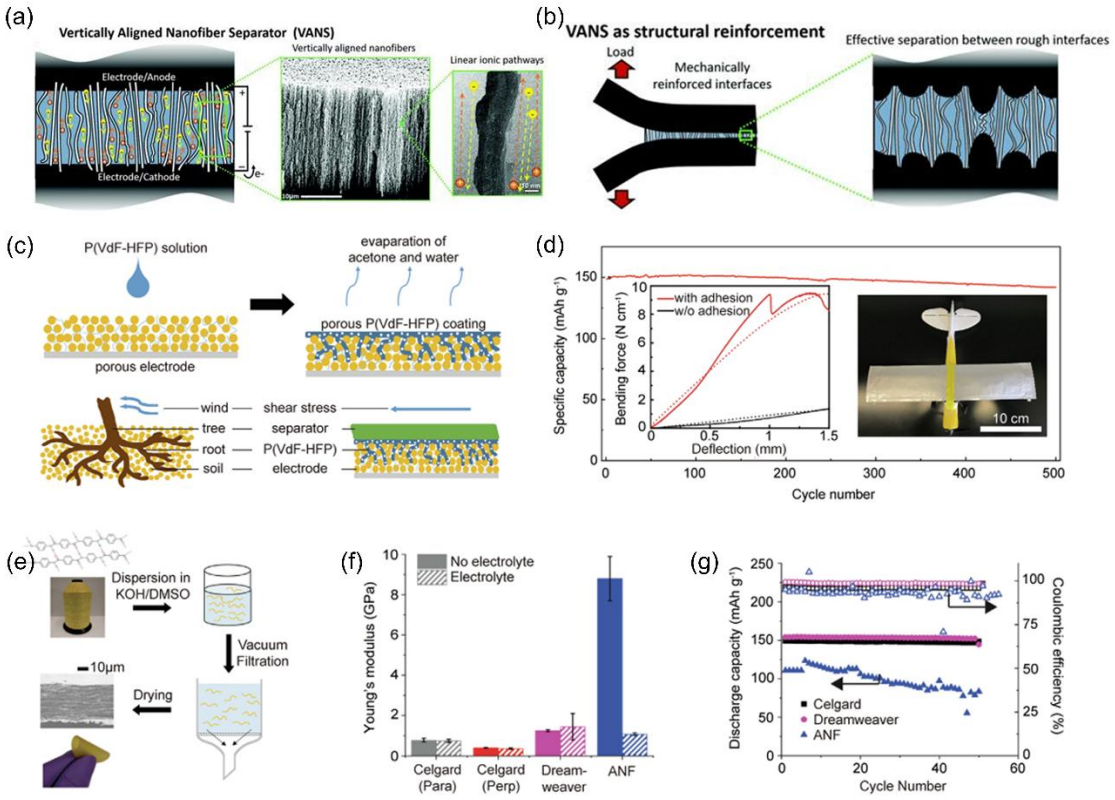


**Figure 2.5** (a) A schematic illustration and SEM figure of the VANS. (b) VANS as both structural reinforcement and ionic transport channels in structural electrodes [45]. (c) A schematic of the fabrication process of a tree-root-like interfacial structure between electrode and separator for structural batteries and the interfacial adhesion against the shear stress introduced by external load, which is compared to a tree against a strong wind. (d) Cycling stability of a structural battery with the tree-root-like adhesion. Left inset: Experimental bending force-deflection curves of the battery with or without electrode/separator adhesion (solid lines) and corresponding FE simulation results (dotted lines). Right inset: Top view of an airplane model with laminated structural battery as "electric wings" [55]. (e) The process of fabricating ANF separators. (f) Young's modulus for Celgard, Dreamweaver, and ANF separators. (g)

Cycle stability of batteries assembled with ANF, Celgard, and Dreamweaver separators [54].

Valuable new material or new concept needs to be proposed for structural separators and binders for CSESDs. The structural separators and binders should remain high mechanical strength even in liquid electrolytes and superior ion transportation. Besides, the interfacial structure can effectively transfer load in layers to enhance the flexural strength of CSESDs.

## 2.3 Design of electrolyte and structural separator

Solid-state electrolytes (SSEs) contain polymers, ceramics, and composites. Load transfer among components under shear or flexural stresses can be further enhanced by the strong solid-state electrolyte, but the ionic conductivity should not be sacrificed significantly. SSE can be employed in CSESDs due to their superior thermal stability and mechanical properties, including tensile and compressive properties, as well as effective load-transfer in interlayers, compared to liquid components [60, 61]. The ionic conductivities are typically $10^{-6}$-$10^{-3}$ S $cm^{-1}$ in solid polymer electrolytes and $10^{-4}$-$10^{-2}$ S $cm^{-1}$ in ceramic electrolytes.

A solid polymer electrolyte (SPE), with polar groups in a polymer to dissociate salts and accelerate ions, can be added with other components, such as ceramic fillers, liquids, or solid plasticizers, to improve ionic conductivity. Poly(ethylene oxide) (PEO), poly(acrylonitrile) (PAN), poly(vinyl alcohol) (PVA), poly(vinylidene fluoride) (PVdF), or polycarbonate (PC) are the common SPEs [62, 63].

The modulus of these polymers is between 290-330 MPa [64] for PEO to 2.6 GPa [65] for PC/PVdF. Adding salts and plasticizers increases the mobility of polymer chains

while weakening the mechanical properties. Snyder et al. studied the correlation between mechanical properties and ion conductivity of structural electrolytes [66, 67]. They also found that co-polymerization is an effective strategy to improve the multifunctionality compared to homopolymers [67]. Although the gel solid electrolytes display high ionic conductivities, their moduli reach approximately several 100 kPa [68-70]. Thereby, the high mechanical properties of the gel electrolyte are crucial for the design of CSESDs. For example, as shown in Fig. 2.5a, Wang et al. proposed a biomimetic aramid nanofibers (ANFs)-based quaternary ammonium functionalized polyvinyl alcohol (QUPA) composite electrolyte membranes to obtain the combination of suitable mechanical and ion transport properties with the ability to withstand large bending and other deformations (Fig. 2.6a). The mechanical properties, such as tensile strength and Young's modulus, increase gradually, along with the increase in ANF concentrations (Fig. 2.6b). The ionic conductivity (61.3 mS $cm^{-1}$) of QUPA/ANF-2.0 membrane is much higher than that of polyvinyl alcohol (PVA) (13.6 mS $cm^{-1}$) and QUPA (46.8 mS $cm^{-1}$) (Fig. 2.6c) [71]. Besides, the composite electrolyte with a gradient composition of PEO and epoxy was designed to improve ion exchange at the interface of electrolyte and electrode (Fig. 2.6de) [72]. In the graded structure, the electrolyte with a high salt ratio (blue open circle) near the electrodes provides paths for ion transport but compromise the mechanical properties. In contrast, the low salt ratio electrolyte in the middle region decreases ion transportation while enhancing mechanical strength (Fig. 2.6d) [72].

Many investigations have been proposed to enhance the mechanical performance of electrolyte. CFs can act as the structurally strong substrates on which the polymer electrolyte is deposited [73]. Besides, epoxy-based electrolytes were used in structural

batteries due to their unique characteristics of adhesiveness [74]. The bi-continuous multifunctional electrolytes, which contain a porous epoxy matrix to support the structure and are penetrated by liquid electrolytes to maintain high ionic conductivity, could be another promising structural electrolyte with high tensile modulus (25-50 GPa) and electrochemical stability [75, 76].

The ceramic electrolytes exhibit higher ionic conductivity and modulus than the polymer electrolyte [77, 78]. The coherent interfaces between ceramic electrolytes and electrodes/current collectors are very difficult to realize. Besides, oxide ceramics are fragile and lack ductility, leading to high interfacial electrode/electrolyte resistance due to the relatively weak bonding strength and cracks under internal stresses [79]. In contrast, sulfide electrolytes are more suitable for being applied in CSESDs as they possess higher toughness. Ceramic electrolytes have been integrated into structural batteries [80]. However, the brittle oxide ceramic electrolytes cannot withstand repeated high bending stress.

Composite electrolytes possess high ion conductivity and modulus comparable to ceramics, as well as the toughness and flexibility comparable to polymers. For example, the nanocomposite polymer electrolyte demonstrates enhanced ionic conductivity ($10^{-4}$-$10^{-3}$ S $cm^{-1}$), which is promoted by the incorporation of ceramic nanoparticles within the polymer matrix [81, 82]. The ionic conductivity and mechanical strength are closely correlated with the geometry and topology of both the ceramic and polymer materials. An increased number of interconnected pathways, formed by nanowires, will enhance ionic conductivity. In general, the mechanical properties of nanocomposites are gradually improved in the following order: nanoparticle, nanowire, nanosheet, and 3D framework [83]. Besides, interfacial

adhesion is crucial to transfer load and enhance mechanical properties. As shown in Fig. 2.6 f-g, Li et al. designed a nacre-like "brick-and-mortar" microstructure for ceramic and polymer composite electrolyte, which realizes a high elastic modulus of 7.8 GPa [84]. Zekoll et al. also developed a poly(propylene carbonate) (PPC)/LLZTO composite electrolyte simultaneously displaying a stable cycling performance and a tensile strength of 6.8 MPa [85]. A high modulus of 6.9 GPa can be achieved by employing bacterial cellulose-supported poly(methyl vinyl ether-alt-maleic anhydride), P(MVE-MA) structural network to a polymer, and then the high ionic conductivity of up to $1.3\times10^{-3}$ S $cm^{-1}$ after soaking in a liquid electrolyte [86]. The electrochemical and mechanical properties of the electrolyte were collected in Table 2.2.

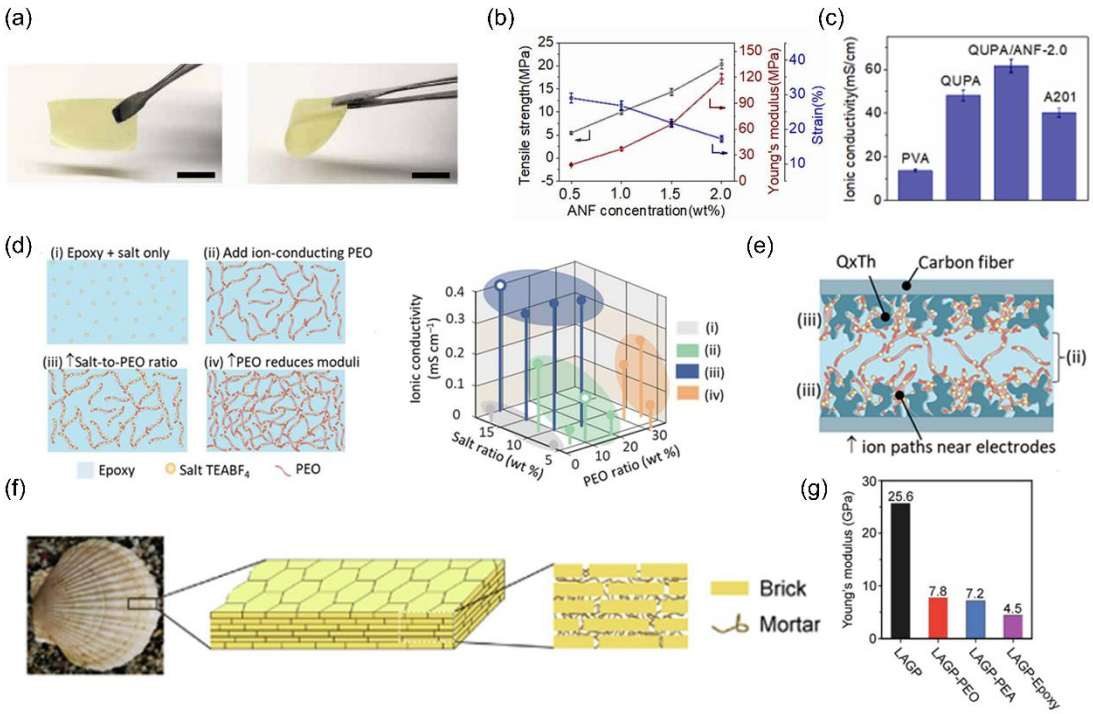


**Figure 2.6** (a) photographs of quaternary ammonium functionalized polyvinyl alcohol (QUPA)/aramid nanofibers (ANFs) composite electrolyte membrane in different states. (b) Tensile strength values, Young's modulus, and elongation at break of QUPA/ANF

with various ANF concentrations. (c) Comparison of ionic conductivity of the PVA, QUPA, and QUPA/ANF-2.0 membranes [71]. (d) Schematic illustration and measurements of ionic conductivity of composite electrolyte with various PEO/epoxy ratios. (e) A cross-sectional schematic of the electrolyte with gradient composition: the edge part electrode region had a higher concentration of salt and PEO than the middle part to enhance the device kinetics. (f) A nacre-like "brick-and-mortar" microstructure composite electrolyte with (g) enhanced Young's moduli [74].

**Table 2.2** Mechanical and electrochemical properties of structural electrolyte.

| Materials | Ion conductivity | Elastic modulus | Ref. |
|---|---|---|---|
| Polymer/CNF electrolytes | 0.32 mS $cm^{-1}$ | 805 MPa | [87] |
| Polymer cellulose electrolytes | 1.3 mS $cm^{-1}$ | 6900 MPa | [86] |
| LATP-GF/PEO-LiTFSI electrolyte | 6.3× $10^{-2}$ mS $cm^{-1}$ | 1.62 GPa | [88] |
| PEEK fiber in PEO/LiTFSI | 61mS $cm^{-1}$ | 0.9 GPa | [89] |
| PEO/$Zn(CF_3SO_3)_2$/BANFs (PZB) | 2.5 ×$10^{-2}$ mS $cm^{-1}$ | 0.21 GPa | [90] |

## 2.4 Mechanical and electrochemical performance of structural energy devices

The design and performance of the composite structure and components which include the electrode, separator, electrolyte, current collector, and assembly materials, are essential for developing advanced CSESDs.

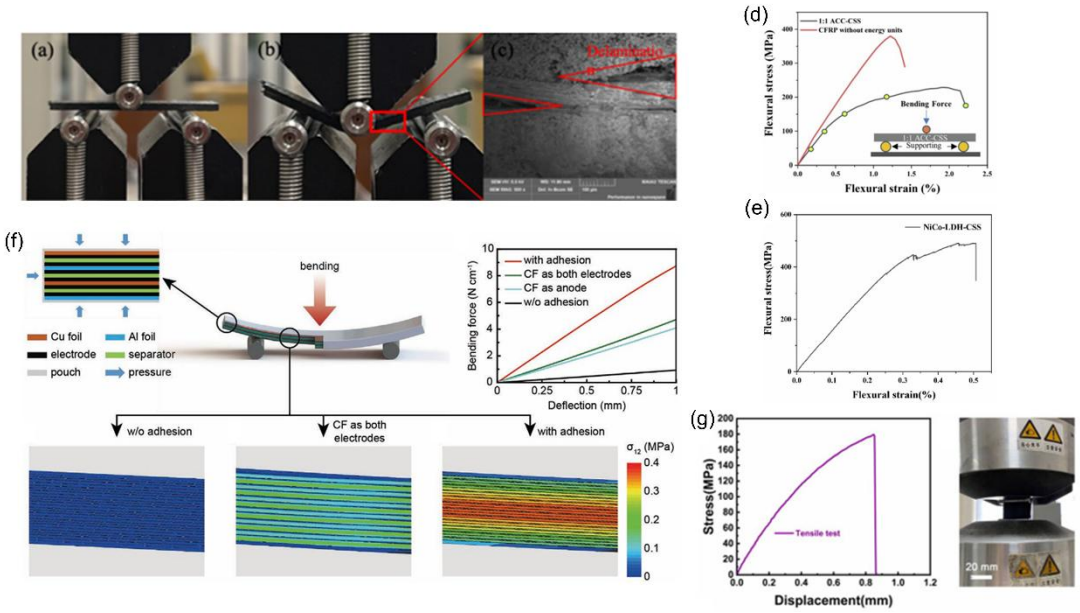


**Figure 2.7** Photos of the composite structural supercapacitor sample (a) before and (b) during the three-point bending test. (c) The SEM image of the structural supercapacitor after the three-point bending test. (d) Flexural stress-strain curves for ACC-CSS and CFRP. [91]. (e) Tensile stress-strain curve for battery composites [92]. (f) The finite element simulation of the three-point bending test for the structural batteries [55].

The mechanical properties, electrochemical performance, and the coupling effect of them need to be carefully investigated. Various characterization techniques can be utilized to explore the structural evolution, failure mechanism, and the degradation of electrochemical performance under applied loads. In general, the mechanical

properties (modulus, strength, stress, fracture strength, and toughness) of the composite structure or the components can be obtained via tensile tests, compression tests, and three-point bending tests. Zhou et al. fabricated the structural supercapacitor (1:1 ACC-CSS) and conducted the three-point bending tests. Fig. 2.7a-b showed the sample before and during the test. The stress-strain curve (Fig. 2.7d) displays that the flexural modulus of the device is lower than the composite without the energy storage unit. As shown in Fig. 2.7c-e, structural delamination failure mainly occurs at the interface between energy units and the carbon fiber reinforcement [91]. The tensile stress-strain curves of the composite battery can be obtained from the tensile measurement [92]. The simulation methods are effective strategies to map the stress, strain, and failure distributions to investigate the mechanical properties of different configurations of CSESDs [55, 93, 94]. As shown in Fig. 2.7f, the finite element simulation results provide the distribution of the shear stress in the composite battery with the tree-root-like electrode/separator interface. [55, 93, 94]. Combining these techniques provides insights into the thorough characterization of composite structure and component performance in CSESDs.

## 2.5 Coupling effect of mechanical and electrochemical performance

In order to assess the electrochemical performance of CSESDs under mechanical stress, in situ mechano-electrochemical tests are conducted to measure the coupling effect between these properties [23]. For example, the multifunctional capabilities of a structural battery cell can be evaluated by strain-dependent cycling retention achieved through conducting reversible charge-discharge tests under tensile loads (Fig. 2.8a) [95]. Besides, as depicted in Fig. 2.8b, the electrochemical performance of CSESDs

under a three-point bending test can be used to evaluate the impact of flexural stress on cycling retention [23].

The in situ mechano-electrochemical coupling performance in CSESDs is crucial to demonstrate their multifunctionality and advance the design and application of CSESDs. As shown in Fig. 2.8c, the influence of deformation on the areal specific capacitance of the LEID-3 was investigated through measuring the electrochemical performance under a three-point bending test. No significant change was observed in the specific capacitance of LEID-3 under this deflection [96]. Zhou et al. further evaluated the in situ mechano-electrochemical performance, and the cyclic voltammetry (CV) curves were stable under five different three-point bending loads (Fig. 2.8d) [91]. In order to verify the stability and reliability of 5:5 NiCo-LDH-CSS under dynamic loads, the in situ tensile fatigue and electrochemical measurements were conducted (Fig. 2.8f). As displayed in Fig. 2.8e, the galvanostatic charge-discharge (GCD) curves and corresponding cyclic tensile load profiles demonstrate that the device offers high capacity retention and intact composite structure under tensile fatigue tests. The little ripples observed in the charge-discharge curve indicate that the applied loads affect the charge-discharge process, revealing the coupling effect between electrochemical performance and mechanical stress (Fig. 2.8g) [97].

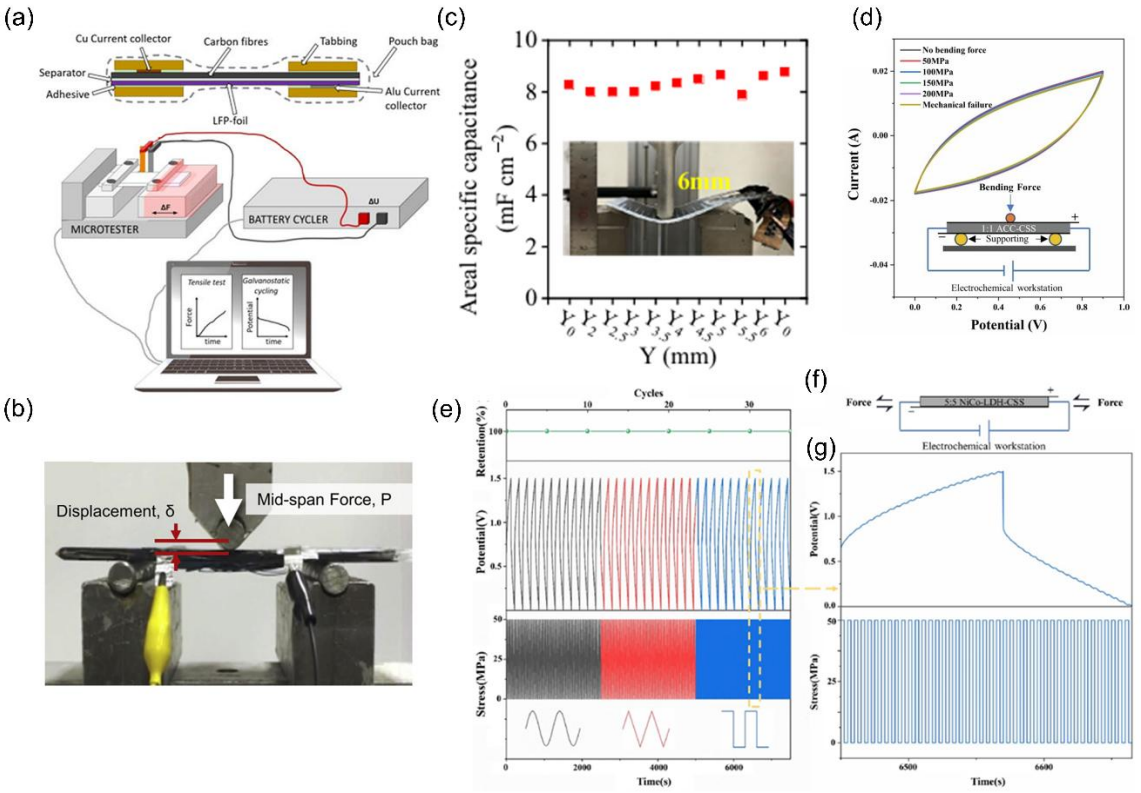


**Figure 2.8** In situ mechano-electrochemical tests for the CSESDs. (a) In situ tensile and electrochemical tests for the CSESDs [95]. (b) In situ three-point bending and electrochemical tests for the CSESDs [23]. (c) Specific capacitance of load-bearing/energy storage integrated devices (LEID-3) at different bending deflections. Inset: photograph of three-point bending test [96]. (d) CV curves of structural supercapacitor (ACC-CSS) under three-point bending test [91]. (e) In situ tensile fatigue and electrochemical measurements of 5:5 NiCo-LDH-CSS at different dynamic stresses [97]. (f) Schematic of test setup [97]. (g) GCD curve and corresponding cyclic load profile from the yellow region of (e) [97].

**Table 2.3** Elastic moduli and ion conductivities of some reported electrolytes. Young's modulus (E), ultimate tensile strength (UTS), and flexural strength (σ)

| CSESD | Energy density ($Wh \cdot kg^{-1}$) | Mechanical properties | Ref. |
|---|---|---|---|
| CNT fiber/polymer electrolytes interleaves | $37.5 \times 10^{-3}$ (cell) | σ= 153 MPa, $E_f$ = 60 GPa | [98] |
| $LiCoO_2$-CNF/PVDF-PEGDMA-gel | 35 (cell) | E=3.1 GPa | [99] |
| PAN@LFP/PAN@Gr | 35 (cell) | E=1.8 GPa | [28] |
| Graphite@CF/structural electrolyte | 23.6 (cell) | E=25 GPa<br>UTS=300 MPa | [11] |
| PS@CF/Li@CF | 43 (cell) | E=1.2 GPa | [36] |
| $MnO_2$@CF/Zn@CF | 182 (active) | E=12.5 GPa,<br>UTS=293 MPa | [37] |
| ZnO-CF/GF/SPE | 0.1562 (cell) | E=21GPa | [100] |
| CuO-CF/GF/SPE | 0.10604 (cell) | E=19.6 GPa | [12] |

## 2.6 Summary

Multifunctional CSESDs enhance the energy density for systems such as electric vehicles and aircraft through reducing the total mass. This concept can be realized by embedding energy units into external reinforcements, employing structural electrodes, electrolytes, and separators, or adopting a special structure to effectively transfer load between inner layers. Considering the coupling effect between mechanical and electrochemical performance, various assessment methods were reported to balance these two properties. Therefore, it is important to evaluate the multifunctional efficiency of CSESDs, and the corresponding evaluation criteria were proposed. Hence, more research and progress at the material and device levels need to be made under the complex conditions during the operation process.

# Chapter 3 Experimental Methodology

## 3.1 Materials

CFs (3K carbon fibers, FAW 200 gsm, Taiwan TEI Composite Co., Ltd.), active carbon (AC) (YEC-8A), and Zn foil (50 μm) sodium sulfate ($Na_2SO_4$, ACS, ≥99%, Aladdin), boric acid ($H_3BO_3$, ACS, ≥99%, Aladdin) were used for electrode preparation. zinc sulfate heptahydrate ($ZnSO_4{\cdot}7H_2O$, AR 99.5%, Aladdin), zinc perchlorate hexahydrate ($Zn(ClO_4)_2{\cdot}6H_2O$) (99.995%, Aladdin), ethylene glycol (EG) (>99%, Aladdin), potassium hydroxide (KOH, ACS reagent, ≥85%, pellets, Sigma), and poly(vinyl alcohol) (PVA, Mw 85,000~124,000, 99+% hydrolyzed, Sigma) were used for electrolyte preparation. zinc trifluoromethanesulfonate (Zn $(OTF)_2$) (98%, Aladdin), bis(trifluoromethane)sulfonimide lithium salt (LiTFSI) (98%, Aladdin), and MXene ($Ti_3C_2T_X$, Foshan xinxi technology Co., Ltd.), acrylamide (AM) (AR reagent, 99.0%, Aladdin), ammonium persulfate (APS) (99.99% metals basis, Aladdin) and N, N′-Methylenebis (acrylamide) (MBA) (97%, Aladdin) were utilized for electrolyte preparation. Westsystem 105 epoxy and 209 hardeners (Hong Kong High Gain Industrial, Co., Ltd.) were used for structural composite supercapacitors fabrication.

### 3.1.1 Preparation of electrodes, polymer electrolyte, and energy storage unit

Zinc electrodes were fabricated via an electrodeposition process on the carbon fiber (CF) substrates. Before electrodeposition, the CFs were activated (ACF) by immersion in a potassium hydroxide (KOH) solution, followed by drying and heating at 800 °C for 2 hours. ACF was immersed in a solution containing 0.1 M $ZnSO_4{\cdot}7H_2O$, 0.2 M

$Na_2SO_4$, and 0.1 M $H_3BO_3$, which was later electrodeposited under various constant current densities (1, 2, 3, 4, 5, 10, and 20 mA $cm^{-2}$) for 2h at room temperature, yielding ZACF1, ZACF2, ZACF3, ZACF4, ZACF5, ZACF10, and ZACF20 anodes, respectively. The slurries of AC, SuperP, and polyvinylidene fluoride (PVDF) at a ratio of 8:1:1 in N-Methyl-2-pyrrolidone (NMP) were stirred at room temperature for 12 hours. Then the slurries were coated on the CF surface and dried at 110 ℃ for 10 hours to obtain the AC-CF cathode material.

A polymer electrolyte was prepared by dissolving 5 g polyvinyl alcohol (PVA) and 28.756 g of $ZnSO_4 \cdot 7H_2O$ in 50 mL of deionized water (DIW) under stirring at 95 ℃ for 5 hours. After cooling the PVA solution to room temperature, the ZACF anode and AC-CF cathode were fully immersed in the PVA-$ZnSO_4$ electrolyte and placed in an oven at 60 ℃ for 10 minutes. The precursor electrolyte-coated carbon fiber electrodes were then pressed together in a sandwich structure and dried in an oven at 60 ℃ for 15 minutes to obtain the energy storage unit.

### 3.1.2 Preparation of electrolyte and supercapacitors with different structures

First, 2M KOH solution was stirred for 30 minutes. Then, 2 g AM as a monomer, 24 mg APS as an initiator, and 1 mg MBA as a cross-linker were blended into 10 mL KOH solution and stirred until the mixture became transparent to get the gel electrolyte precursor for subsequent utilization.

Two CFs-AC electrodes and the gel electrolyte precursor were placed into the designed mold to undergo in-situ polymerization on the CFs-AC electrodes at 60 ℃ for 1.5 hours. By adjusting the amount of the transparent electrolyte solution, a bulged snap-

on buckle structure was polymerized onto the pore structure of the carbon cloth. The thickness of hydrogel was controlled to be less than 1 mm. The sandwich structure was fabricated by the conventional method, where the transparent electrolyte solution was first dropped into the mold to polymerize at 60 ℃ for 1.5 hours, forming the gel electrolyte. Then the CFs-AC electrodes and gel electrolyte were stacked into a sandwich structure.

### 3.1.3 Preparation of electrolytes with and without MXene

First, water in salt (WIS) electrolyte was prepared by stirring 1 M Zn $(OTF)_2$ and 21 M LiTFSI. After the solution became clear, 2 g AM, 24 mg APS, and 1 mg MBA, acting as monomer, initiator, and cross-linker, respectively, were mixed into 10 mL of the as-prepared WIS solution. Then, the electrolyte precursor was obtained, and the electrolyte without MXene (WIS-P electrolyte) was formed through a polymerization process at 65 ℃ for 2 h. The same procedure was used to prepare the MXene-based electrolyte (WIS-P-M electrolyte), except for the introduction of different contents of $Ti_3C_2T_X$/deionized water (DIW) (10 mg $ml^{-1}$) into the 10 ml WIS electrolytes.

### 3.1.4 Preparation of SH-PAM, SE-PAM, and CE-PAM electrolytes

First, a precursor solution was prepared by dispersing 2 g AM as the monomer, 24 mg APS as the initiator, and 1 mg MBA as the cross-linker in 10 mL of 2M $ZnSO_4$ solution. The resulting precursor was polymerized at 60 ℃ for 2 h to obtain the SH-PAM electrolyte. Following a similar procedure, SE-PAM was synthesized by replacing the solvent with a 1:2 (v/v) mixture of ethylene glycol (EG) and water. For CE-PAM, $Zn(ClO_4)_2$ was used instead of $ZnSO_4$ in the EG/water (1:2 v/v) solvent.

## 3.2 Fabrication of CSSs

A wet lay-up composite manufacturing method was adopted to fabricate CSS devices. The CFs and glass fabric impregnated with epoxy resin, and energy storage units including electrodes and electrolyte, were laid layer by layer according to the pre-designed position and placed on an aluminum plate. Then, a vacuum bag was covered on the plate and the CSS was obtained after vacuum curing for 24 hours at room temperature.

## 3.3 Characterizations

### 3.3.1 Material Characterizations

The sample morphologies were characterized using field-emission scanning electron microscopy (FESEM, MAIA3) and transmission electron microscopy (TEM, Jeol, JEM-2100F) at 200 kV accelerating voltage. The specific surface area of the material was determined by Brunauer-Emmett-Teller (BET) test machine (Micromeritics ASAP2020). X-ray diffraction (XRD, Rigaku SmartLab 9kW - Advance) was used for crystal structure analysis. Raman spectrum was collected by WITEC confocal Raman system. X-ray photoelectron spectroscopy (XPS, Thermo Scientific K-Alpha) was used to analyze the valence states of elements. X-ray computed tomography (X-ray CT, Bruker Skyscan 1172) was used to characterize the internal structure damage of ACNT-CSS after drop-weight impact. Differential scanning calorimetry (DSC, NETZSCH, DSC214) was conducted within a temperature range of -105 ℃ to 20 ℃ at a scan rate of 5 ℃ $min^{-1}$ to characterize the solid-liquid transition temperature of the electrolyte. The Fourier-transform infrared spectrometer (FTIR) (Frontier, PerkinEImer, America) was utilized for performing the FTIR analysis.

### 3.3.2 Electrochemical and Mechanical Characterizations

Cyclic voltammetry (CV), and galvanostatic charge-discharge (GCD) were operated by the electrochemical workstation (CHI660e, Chenhua, China) at room temperature. Galvanostatic cycling tests were conducted using a two-electrode configuration. The cells were assembled in a 2032-type coin cell format, employing Zn foil or ZACF as the anodes, AC-CF as the cathode, a glass fiber as the separator, and 180 μL 2 M $ZnSO_4$ as the electrolyte. The electrochemical performance of CSSs was also evaluated using a two-electrode system. The specific capacitance of the electrode materials was calculated from the GCD curves according to the following equation [101],

$$C = I \cdot \Delta t / m \cdot \Delta V \tag{3.1}$$

where $I$ is the current (mA), $m$ is the mass (g), Δt is the discharge time (s) and $\Delta V$ is the potential window (V).

The energy density of the device ($E$, $mWh \cdot kg^{-1}$) can be obtained from the following equations [102],

$$E = \frac{1}{M} \int_0^t A V_{(t)} \, dt \tag{3.2}$$

where $A$ is the discharge current, $V(t)$ is the discharge voltage at time $t$, and $M$ is the mass of total CSS or active materials.

The electrochemical performance measurements, including voltage profiles and cyclic performance of CSSs, were recorded by using a battery test system (LAND CT2001A) on a two-electrode system. The ionic conductivity of the hydrogel solid electrolyte was calculated from Equation 3.3 [103],

$$\delta = L/RS \tag{3.3}$$

where $L$ is the thickness of the solid electrolyte, and $R$ is the bulk resistance obtained from the intercept of the impedance curve on the x-axis. $S$ represents the test area of the polymer electrolyte

A three-point bending and short beam shear tests were conducted by a universal testing machine (Static testing system 5 kN zwicki). For the three-point bending test, samples (10 cm × 2 cm × 2 mm) were tested with a support span of 5 cm at the bending speed of 2 mm·min$^{-1}$. For the short beam shear test, samples (2 cm × 1 cm × 2 mm) were tested with a support span of 1 cm at the bending speed of 1 mm·min$^{-1}$. The flexural strength and flexural modulus of the device were calculated using the following equations [97],

$$\sigma_f = \frac{3PL}{2bd^2} \tag{3.4}$$

$$E_f = \frac{L^3 m}{4bd^3} \tag{3.5}$$

where $\sigma_f$ is flexural stress (MPa), $P$ is maximum applied load (N), $L$ is the support span (mm), $b$ is the width of the CSS sample (mm), $d$ is the thickness of the sample (mm), $E_f$ is flexural modulus (MPa), and $m$ is the slope of the initial straight line of the load-deflection curve (N·mm$^{-1}$).

In situ mechano-electrochemical tests of CSS can be used to study the correlation between flexural stress and electrochemical performance. The in-situ electrochemical properties were studied under different constant flexural stresses of 30, 50, and 70 MPa. The test was conducted by three-point bending (Static testing system 5 kN

zwicki) and electrochemical workstation (CHI660e, Chenhua, China) to measure mechanical performance and electrochemical properties simultaneously.

### 3.3.3 In-Situ Mechano-Electrochemical Characterization

In-situ mechano-electrochemical characterization is a double-field coupling test, and it was used to test the electrochemical performance of CSSs with the application of external loads to study the impact of external load on the electrochemical performance. Four electrochemical mechanical measurements were carried out in this thesis, including electrochemical three-point bending test, electrochemical tensile test, and electrochemical three-point bending fatigue test and electrochemical tensile fatigue test. The external force was constant in the first two tests and dynamic in the last two tests. Universal testing machines were used in the electrochemical three3-point bending (Static testing system 5 kN zwicki), electrochemical three-point bending fatigue (Static testing system 5 kN zwicki) and electrochemical tensile tests (Static testing system 20 kN zwicki), while a fatigue machine was used to perform the electrochemical tensile fatigue test (Linear testing system 10 kN zwicki). In the process of applying external force, an electrochemical workstation (CHI660e, Chenhua, China) was applied to test electrochemical properties.

### 3.3.4 Simulation

**Specified geometry and boundary conditions in the 2D electrochemical model.**

The energy unit of CSS was built as a 2D electrochemical model for simulation. As shown in Fig.3.1a, the model was constructed with a three-layer configuration consisting of anode, electrolyte, and cathode, with same thicknesses of 0.2 mm, maintaining consistency with experimentally fabricated samples. A 1-mm-length representative volume element (RVE) approach was implemented with periodic

boundary conditions at both left and right sides to reduce computational cost while maintaining accuracy.

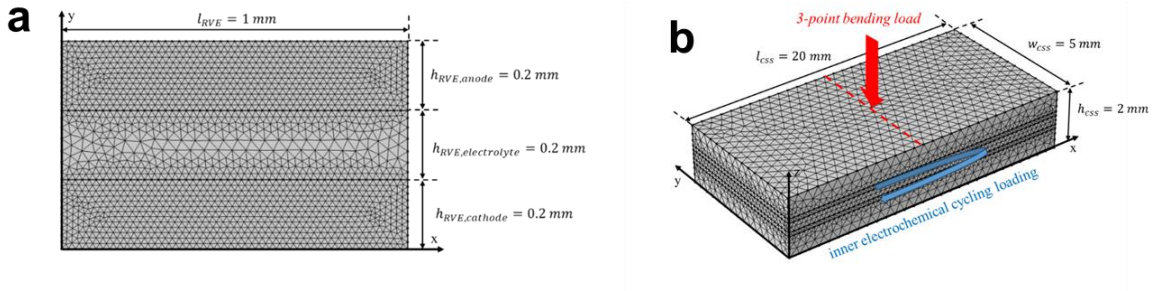


**Figure 3.1** (a) 2D RVE electrochemical model. (b) 3D mechanical model.

**Geometry and boundary conditions in the 3D mechanical model**

The three-dimensional mechanical model was established to simulate the CSS under three-point bending conditions. As shown in Fig. 3.1b, two protective composite layers (0.7 mm each) were symmetrically arranged on either side of the 0.6-mm-thick energy unit. In this model, the width was maintained identical to the experimental samples as 5 mm, while a reduced span length of 10 mm was adopted for simulation. This modeling strategy was implemented because the three-point bending load was applied on the model sample through bending stress rather than force. This approach ensured equivalent internal bending stress magnitudes while significantly improving computational efficiency. Three-point bending stresses of 0 MPa, 30 MPa, 50 MPa, and 70 MPa were independently applied along the central axis of the top surface to investigate the mechanical response under varying load conditions, while fixed constraints were imposed at the bottom left and right boundaries to accurately replicate

**Coupling strategy between electrochemical model and mechanical model**

The coupling strategy between electrochemical model and mechanical model is illustrated in Fig. 3.2. A 2D RVE electrochemical model of the CSS (Fig. 3.1a) was

built to obtain electrochemical parameters, including the potential distribution and Zn ion concentration distribution. During charge/discharge cycles, the Zn ion concentration in energy unit of CSS exhibits cyclic variations governed by an electrochemical model, which induce corresponding volume deformations. To achieve this coupling step, the Zn ion concentration distribution obtained from the two-dimensional electrochemical model was converted to strain distribution through expansion coefficients ( $\beta$ ). These electrochemically induced strains generated corresponding stress fields, which were subsequently mapped along the y-axis direction and incorporated into the 3D mechanical model as cyclic electrochemical loading inputs.

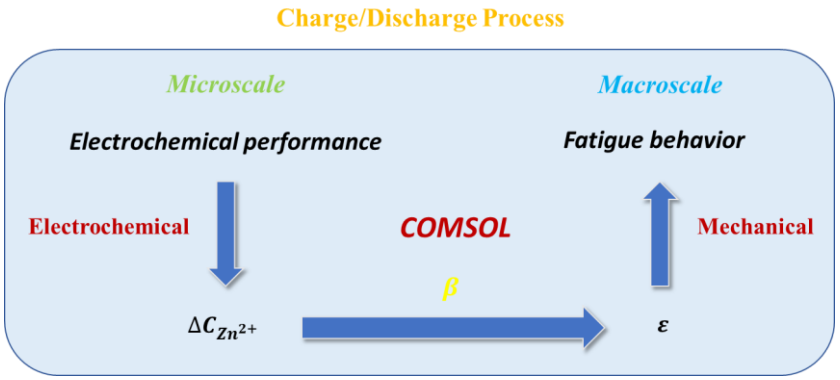


**Figure 3.2** Multi-physics coupling strategy.

The coupled simulation framework ultimately enabled comprehensive fatigue analysis under combined mechanical bending and electrochemical cycling loads, providing critical insights into the multi-physics failure mechanisms.

### Governing equations and parameters in the Multiphysics model

#### Electrochemical model

In electrochemical model, the governing equations of CSS (including modified CF of

anode and cathode and polymer electrolyte) are shown as follows:

Mass transfer and conservation

In CF, Zn ion flux is given by:

$$N_{cf} = -D_{cf}\nabla c_{cf} \tag{3.6}$$

In MCF, the conservation of mass requires:

$$\frac{\partial c_{cf}}{\partial t} + \nabla N_{cf} = 0 \tag{3.7}$$

where $N_{cf}$, $D_{cf}$ and $c_{cf}$are Zn ion flux, diffusivity, and concentration of modified CF electrodes respectively. Besides, $t$ is time and $\nabla$ is gradient operator in the two-dimensional model.

**Ohm's law and conservation of charge**

In polymer electrolyte, the current density is described using ohm's law:

$$i_{pe} = -\sigma_{pe}\nabla\phi_{pe} \tag{3.8}$$

Where $i_{pe}$ is current density and $\sigma_{pe}$ is Zn ion conductivity of polymer electrolyte. $\phi_{pe}$ is the potential of polymer electrolyte.

In polymer electrolyte, the conservation of charge requires:

$$\nabla \cdot i_{pe} = 0 \tag{3.9}$$

In modified carbon fiber electrodes, the current density is given by Ohm's law:

$$i_{cf} = -\sigma_{cf}\nabla\phi_{cf} \tag{3.10}$$

where $i_{cf}$, $\sigma_{cf}$ and $\phi_{cf}$ are current density, Zn ion conductivity and potential of modified carbon fiber electrodes, respectively.

In modified carbon fiber electrodes, the conservation of charge requires:

$$\nabla \cdot i_{cf} = 0 \tag{3.11}$$

where $i_{cf}$, $\sigma_{cf}$ and $\phi_{cf}$ are current density, Zn ion conductivity and potential of modified carbon fiber electrodes, respectively.

**Mechanical model**

The 3D mechanical model was developed to simultaneously account for both three-point bending loads and internal electro-fatigue loading within the energy unit. The macroscopic stress in the modified CF electrode scale, $\sigma_{ij}$, is given by [104, 105]:

$$\sigma_{ij} = C_{ijkl}(\varepsilon_{kl} - \varepsilon\delta_{kl}) \tag{3.12}$$

where $C_{ijkl}$ is a fourth-order elastic tensor, $\varepsilon_{kl}$ is the strain tensor in modified CFs anode, $\varepsilon$ is the strain tensor, $\delta_{kl}$ is Kronecker delta.

The equilibrium of stress is given by:

$$\nabla \cdot \sigma = 0 \tag{3.13}$$

**Coupling of mechanical and electrochemical models**

The electrochemical and mechanical models mentioned above are coupled through the Zn ion concentration, $c$, and the Eigen strain, $\varepsilon$. The Zn ion intercalation swelling based on the hygroscopic swelling equation is used to describe this expansion and contraction during the process of Zn ion transferring in the electrolyte which causes

concentration gradient:

$$\varepsilon = \beta M\left(c - c_{ref}\right) \tag{3.14}$$

where $\varepsilon$ is the Eigen strain caused by Zn ion intercalation and deintercalation, $\beta$ is the expansion coefficient of Zn ion intercalation, $M$ is the molar mass of Zn ion, $c$ is the Zn ion concentration, which is calculated by the 2D electrochemical model, and $c_{ref}$ is the strain-free reference concentration.

**Fatigue model**

In this work, Dirlik model is used and paired with the Basquin fatigue criterion to compute the fatigue life of the energy unit of CSS. The Basquin fatigue criterion is given by:

$$\sigma_a = \sigma_f'\left(2N_f\right)^b \tag{3.15}$$

where, the amplitude stress $\sigma_a$ is related to the number of cycles $N_f$ through the parameters $\sigma_f'$ = 2.2 GPa and $b$ = –0.25. The fatigue failure number $N_f$ of each component in energy unit can be obtained from S-N curve based on existing literature [106, 107].

The multi-field coupling characterization here is to add an additional temperature field on the basis of original electrochemical mechanical tests, which is used to study the effect of temperature change on the electrochemical performance of CSS under a constant load. Temperature and bending force were applied through a universal testing machine with a temperature box (ZwickRoell 250 kN Allround floor) and the electrochemical test was accomplished by Chenhua CHI660e.

The values of electrochemical and mechanical variables in the models are summarized in Table 4.2.

**Density functional theory (DFT) calculations**

The binding energies were calculated by DFT in the ORCA package [108]. For geometry optimization and single-point energy calculations, they were performed under the B3LYP-D3BJ/6-311G* [109] and B2PLYP-D3BJ/def2-TZVP levels[110], respectively.

# Chapter 4 Electrochemical Cycling Decay Induced by electro-fatigue of CSSs

In order to investigate the coupling effect of electrochemical and mechanical performance, in Chapter 4, a Zn-ion-based hybrid CSSs incorporating a composite energy storage unit were developed. The electrochemical cycling-induced fatigue (electro-fatigue) failure and mechano-electrochemical coupling performance were investigated. In situ mechano-electrochemical tests reveal that the fabricated CSS maintains 101.6% of its initial capacity (49.3 mAh $g^{-1}$) after 1000 cycles under an applied flexural stress of 30 MPa. Upon increasing the stress to 70 MPa, capacity retention decreases to 81.8% after 3000 cycles. Furthermore, SEM analysis shows a progressive structural degradation correlated with elevated stress levels. Simulation results reveal that the Zn ion concentration gradient during charge and discharge processes induces alternating stress, which can be equivalent to a mechanical fatigue stress. The electro-fatigue stress gives rise to structural failure and a reduction in electrochemical performance. Moreover, for CSSs, coupling electro-fatigue stress with constant external stress results in increased fatigue stress, significantly accelerating structural failure. These findings elucidate the failure mechanism of CSSs caused by the cycling process, offering valuable insights and strategies to concurrently preserve superior electrochemical and mechanical integrity.

## 4.1 Introduction

The demand for high energy density electric cars and aircraft has driven the development of multifunctional devices that synergistically integrate electrical energy

storage and load-bearing capabilities [111, 112]. Replacing conventional structural components with these multifunctional devices can significantly reduce the overall system weight [1, 11, 113]. The multifunctional CSSs have been extensively applied in weight- and volume-constrained domains such as electric vehicles and aircraft [12, 114-117].

There are two structural designs for CSSs: decoupled and coupled [14, 16, 17, 118]. In the decoupled approach, supercapacitors are embedded into the CF reinforcement, in which the energy storage units and reinforcement components remain independent. Consequently, this configuration has a limitation in weight reduction and potentially introduces structural defects into the system [6, 10]. Conversely, the coupled approach integrating multifunctional energy storage units, including composite structural carbon fiber electrodes, current collectors, and electrolytes, into CSSs efficiently decreases the total mass and structural defects. For instance, high-strength structural carbon fiber electrodes and electrolytes with an epoxy resin matrix have been successfully combined into all-solid-state CSS [119]. Besides, the high interfacial adhesion is also crucial to effectively transfer load and prevent relative sliding under mechanical loading, thereby stabilizing the structure and maintaining electrochemical performance [23, 55]. However, for this method, it needs to be carefully designed to ensure that the electrochemical properties of the composite materials are not compromised [14]. Recently, Zhang *et al.* fabricated a structural supercapacitor with a multilayer structure, which achieves a high flexural strength of 160.0 MPa and simultaneously exhibits a high energy storage capability of 32.4 mF $cm^{-2}$ [96].

Despite these advancements, research on the effect of electrochemical cycling on structural failure, particularly under applied loads, remains limited for CSSs. Finite

element simulations may offer an economically efficient and technically meaningful approach to investigate the structural failure of CSSs caused by the electrochemical process and the coupled electrochemical-mechanical behavior during operation. While some foundational simulation work related to other research has been conducted on analogous systems, such as structural battery and all-solid-state battery [120-122], dedicated simulations for CSSs remain rare.

The electrochemical cycling-induced fatigue (electro-fatigue) failure of an all-solid-state Zn-ion CSS integrating the composite electrodes and electrolyte was investigated. In situ mechano-electrochemical characterizations reveal that the designed CSS exhibits a high capacity retention of 101.6% after 1000 electrochemical cycles under constant external flexural stress of 30 MPa, with the retention decreasing to 81.8% as the stress increases to 70 MPa. SEM images show that cracks within the energy storage unit propagate as the stress increases from 30 to 70 MPa after 3000 cycles. The simulation results demonstrate that the electrochemical cycling process induces mechanical fatigue stress as a result of volume changes caused by the ion concentration gradient. Furthermore, the combination of charge-discharge fatigue stress and applied loads leads to a greater cumulative fatigue stress, which ultimately promotes structural degradation and electrochemical deterioration. This study provides comprehensive insights into the capacity decay mechanism under moderate mechanical load, which will guide the rational design of CSSs with balanced electrochemical and mechanical properties for practical applications.

## 4.2 Morphology and electrochemical performance of zinc electrode materials

The fabrication process of the zinc activated and deposited structural carbon fiber negative electrodes are illustrated in Fig. 4.1a. The CF substrate was first activated by potassium hydroxide (KOH) at 800°C for 2 hours. Zinc was then electrodeposited onto the activated CF under various current densities (1, 3, 4, 5, 10, and 20 mA $cm^{-2}$). SEM images (Fig. 4.1b-d and Fig. 4.2a-c) show that the CF network serves as a three-dimensional (3D) substrate for zinc electrodeposition. Zinc nanosheet arrays were successfully grown on the CF substrate at lower current densities (1, 3, 4, and 5 mA $cm^{-2}$). In particular, at 1 and 3 mA $cm^{-2}$, the zinc nanosheets were uniformly distributed on the CF surface. However, at higher current densities (4 and 5 mA $cm^{-2}$), aggregation of zinc nanosheets was observed. When the current density was further increased to 10 and 20 mA $cm^{-2}$, flat zinc particles were formed instead of nanosheets.

XRD spectroscopy was employed to investigate the phase evolution of the ZACF samples (Fig. 4.1e). The XRD patterns of ZACF prepared at lower current densities (1 to 4 mA $cm^{-2}$) displayed two diffraction peaks at $2\theta$ values of 25° and 43° [123], which correspond to the CF substrate. Notably, all ZACF samples displayed sharp characteristic peaks corresponding to metallic hexagonal zinc, confirming the successful deposition of pure zinc metal without any discernible impurities [124].

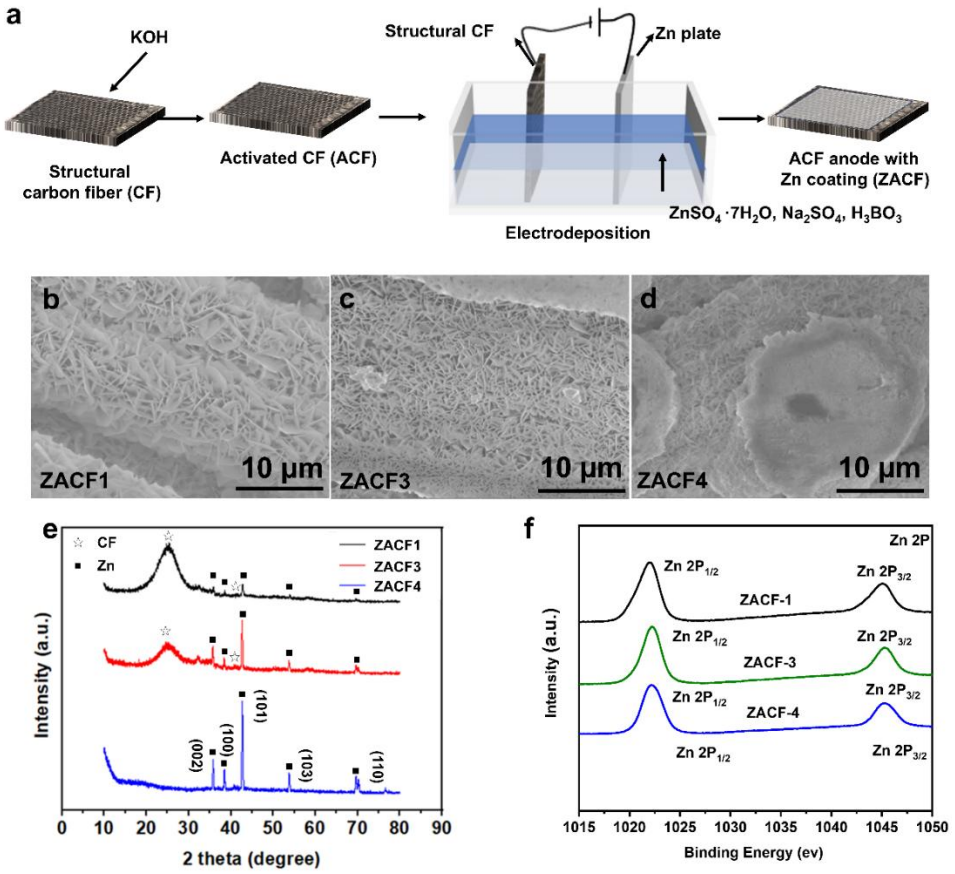


**Figure 4.1** (a) Schematic illustration of the zinc electrodeposition process. (b-d) SEM images of ZACFs prepared under various current densities. (e) XRD patterns and (f) XPS spectra of ZACF anodes prepared under electrodeposition current densities of 1, 3, and 4 mA $cm^{-2}$.

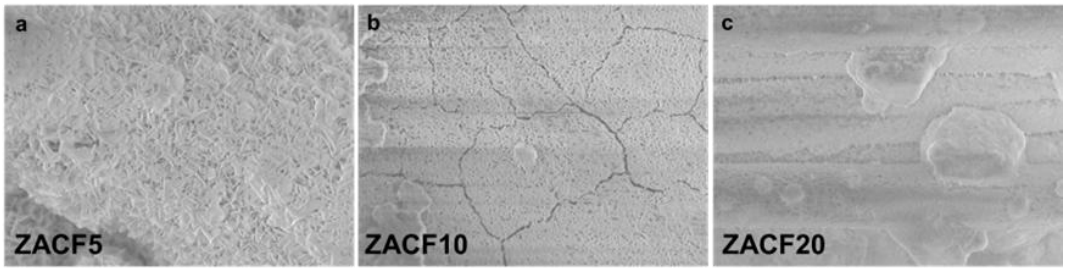


**Figure 4.2** SEM images of Zn electrodeposition on ACF at various current densities: (a) 5 mA $cm^{-2}$ (ZACF5), (b) 10 mA $cm^{-2}$ (ZACF10), and (c) 20 mA $cm^{-2}$ (ZACF20)

XPS results provided valuable insights into the chemical states and composition of the zinc species present in the ZACF samples. The high-resolution Zn 2p spectrum (Fig. 4.1f) revealed two distinct peaks at binding energies of 1021.9 and 1045 eV, which can be assigned to Zn $2p_{3/2}$ and Zn $2p_{1/2}$, respectively [126, 127]. The result confirms that the zinc deposited on the CF substrate exists in its metallic state and is successfully electrodeposited on the CF surface. The XPS, SEM, and XRD analyses have verified the formation of uniform blade-like zinc nanosheets on the CF substrate under electrodeposition current densities ranging from 1 to 3 mA $cm^{-2}$.

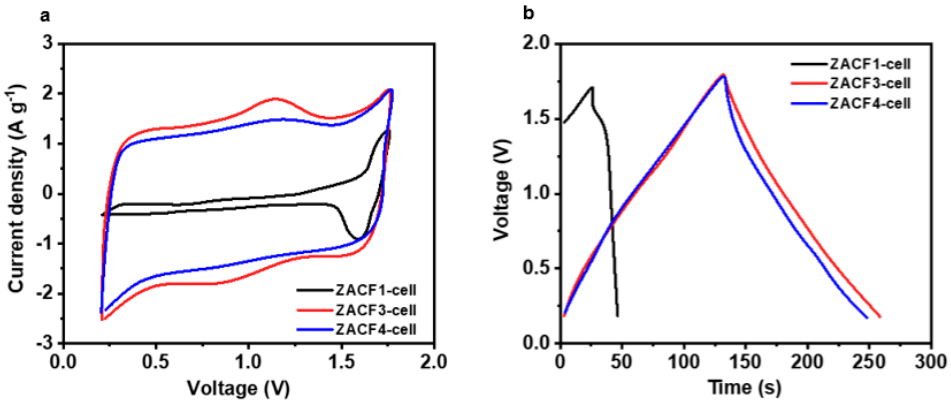


**Figure 4.3** (a) The CV curve and (b) GCD profiles of ACF-cell, ZACF3-cell and Zn-cell.

To evaluate the electrochemical performance of the ZACF samples, CV and GCD tests were conducted using coin cells comprising different ZACF anodes and AC-CF cathodes. As depicted in Fig. 4.3a, the coin cells exhibited a stable working voltage window of 0.2-1.8 V at a scan rate of 20 mV $s^{-1}$. Notably, when the electrodeposition current density was below 3 mA $cm^{-2}$, the low zinc content was insufficient to trigger the desired capacitive properties. However, as the current density was increased to 3

mA $cm^{-2}$, the CV curves showed a quasi-rectangular shape, and the specific current density reached its maximum value, indicating an enhanced capacitive behavior. These findings were further corroborated by the GCD curves (Fig. 4.3b). Based on a comprehensive analysis of the morphological, structural, and electrochemical characterization results, it can be concluded that 3 mA $cm^{-2}$ represents the optimal current density for Zn electrodeposition.

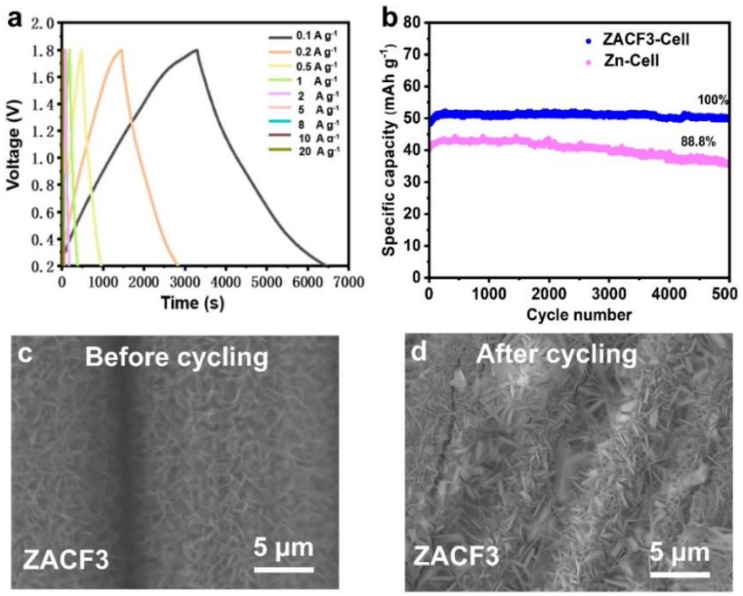


**Figure 4.4** (a) GCD curves of ZACF3-cell at various current densities. (b) Long-term cycling stability comparison between ZACF3-cell and Zn-cell. (c-d) SEM images of ZACF3 anode before and after 5000th cycling.

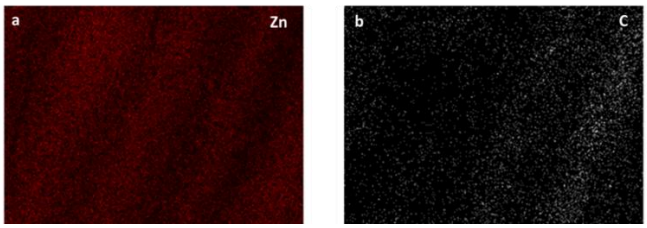


**Figure 4.5** EDS mapping images of ZACF3 anode after 5000th cycles.

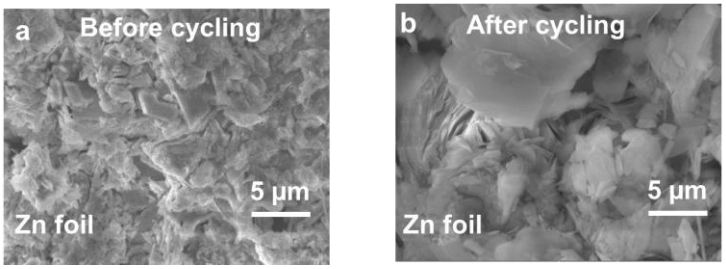


**Figure 4.6** (a-b) SEM images of Zn foil anode before and after 5000th cycling.

GCD results in Fig. 4.4a revealed the specific capacity values of the ZACF3-cell at different current densities. The cell achieved a high specific capacity of 87.5 mAh $g^{-1}$ at a current density of 0.1 A $g^{-1}$. In Fig. 4.4b, the ZACF3-cell exhibited higher capacity retention (100% after 5000 cycles at a current density of 1 A $g^{-1}$) than the Zn-cell (Zn foil as anode and AC-CF as cathode) (88.8%). In Fig. 4.4c-d, the SEM images showed that the ZACF3 anode maintained a smooth and dendrite-free surface, similar to its pristine structure even after prolonged cycling. Energy dispersive spectroscopy (EDS) mapping images of ZACF3 anode after the 5000th cycle showed that Zn was uniformly distributed on the carbon fiber substrate (Fig. 4.5). This observation suggested that the ZACF3 anode effectively suppresses the formation of zinc dendrites, ensuring stable electrochemical performance. In contrast, the SEM image of the Zn foil anode after 5000 cycles (Fig. 4.6a-b) showed significant aggregation and dendrite formation on its surface. The formation and growth of these dendrites can lead to short-circuiting and rapid capacity decay. The superior electrochemical performance and morphological stability of the ZACF3 anode can be attributed to its nanosheet structure, which increases overall active sites on the surface area for efficient charge storage and transfer and thus enhances the kinetics of ion diffusion. Furthermore, the CF matrix offered a robust and conductive network for electron transport. In summary, the high specific capacity, excellent rate capability, and exceptional cycling stability of the

ZACF3 anode and its ability to suppress dendrite formation make it a promising candidate electrode for Zn-ion based CSS.

## 4.3 Electrochemical and mechanical performance of the ZACF3-CSS

To evaluate the potential for practical applications, CSSs were systematically fabricated by encapsulating the energy storage unit (comprising a ZACF3 anode, a polymer electrolyte, and an AC-CF cathode) between two CF layers in a sandwich configuration, followed by epoxy resin infusion (Fig. 4.7a). Based on the total mass of the CSS, GCD measurements were conducted (Fig. 4.7b). The device delivered a specific capacity of 0.189 mAh $g^{-1}$ at 0.5 mA $g^{-1}$, and retained 0.0335 mAh $g^{-1}$ at 2 mA $g^{-1}$, demonstrating high rate performance. The device achieved a specific capacity of 0.142 mAh $g^{-1}$, an energy density of 228 mWh $kg^{-1}$ at a power density of 1600 mW $kg^{-1}$ at 1 mA $g^{-1}$. Based on the active material mass, the energy density was 39.2 Wh $kg^{-1}$ at a power density of 80.8 W $kg^{-1}$ at 0.2 A $g^{-1}$ and had a high rate performance at different current densities (Fig. 4.8). The comparison of ZACF3-CSS with recent research data is shown in Fig. 4.7c. These results demonstrate that ZACF3-CSS exhibits excellent electrochemical performance.

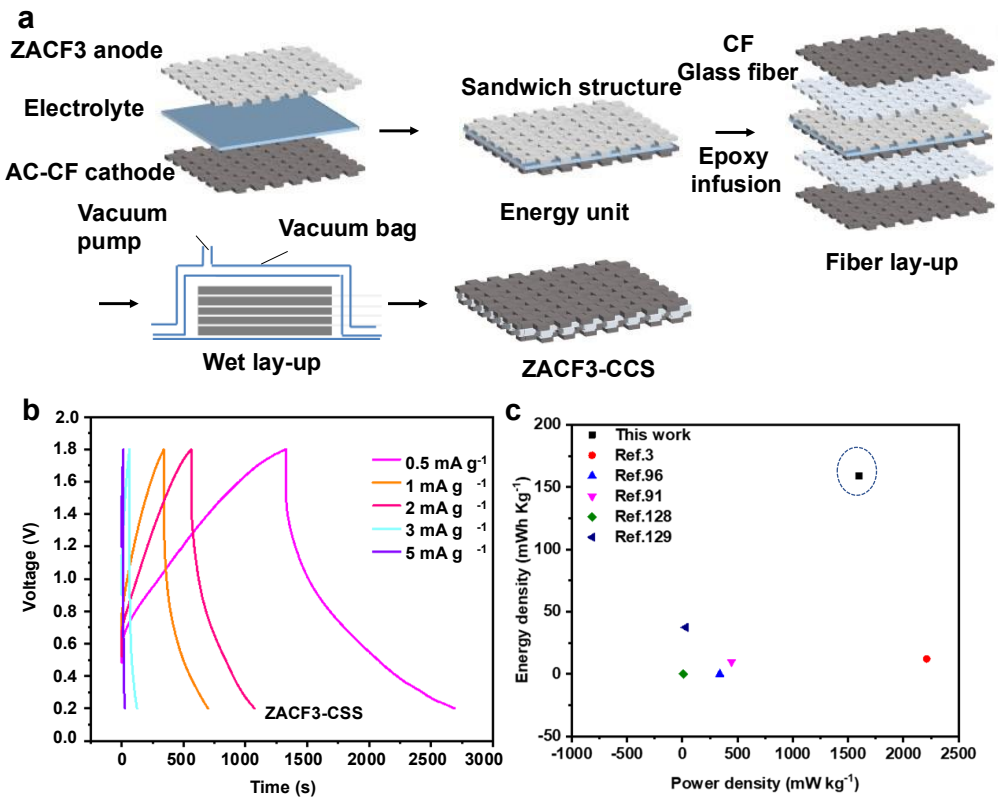


**Figure 4.7** (a) Schematic illustration of the fabrication process for ZACF3-CSS. (b) GCD curves of ZACF3-CSS were measured at various current densities. (c) Comparison of the electrochemical properties of ZACF3-CSS with previously reported structural energy storage devices.

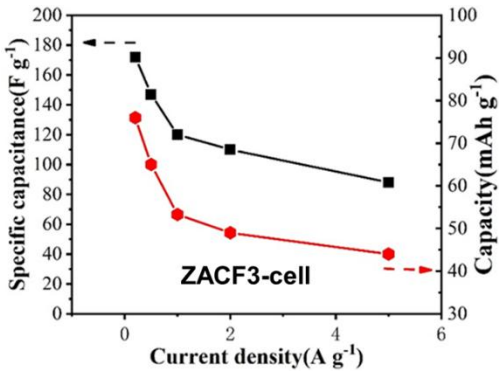


**Figure 4.8** Rate performance of ZACF3-cell.

**Table 4.1** Comparison of energy density and power density parameters of the Zn-ion based CSS with other CSSs in literature.

| CSSs | Energy density ($Wh \cdot kg^{-1}$) | Power density ($W \cdot kg^{-1}$) | Ref. |
|---|---|---|---|
| CF/VG/$MnO_2$ | 0.0122 [b] | 2.2103 [b] | [3] |
| LEID-3 | 0.034[b] | 0.34 [b] | [96] |
| ACC-CSS | 0.0099[b] | 0.4455[b] | [91] |
| Kevlar/epoxy | 0.169[c] | 20[c] | [128] |
| | 0.00008[b] | 0.0092[b] | [128] |
| CF/EDLC/CF | 0.0375[b] | 30[b] | [129] |
| ZACF3-CSS | 39.2[a] | 80.8[a] | This work |
| | 0.2277[b] | 1.5998[b] | This work |

[a] Normalized based on active materials.

[b] Normalized based on composite device.

[c] Normalized based on electrode mass.

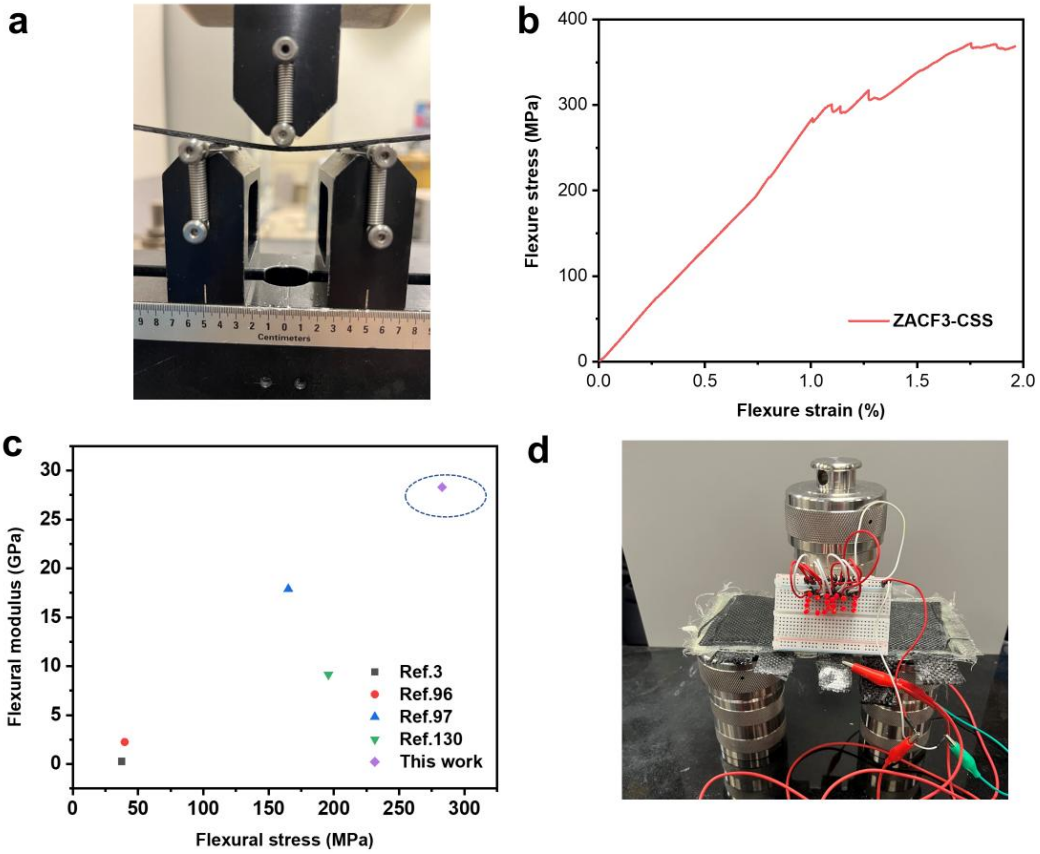


**Figure 4.9** (a) Photo images of the experimental setup for three-point flexural testing. (b) The three-point test curves of ZACF3-CSS. (c) Comparison of mechanical performance between ZACF3-CSS with previously reported structural energy storage devices. (d) In situ demonstration of ZACF3-CSS practical application of powering LED under mechanical loading.

Under a three-point bending test, the ZACF3-CSS exhibited a flexural strength and flexural modulus of 282.9 MPa and 28.3 GPa, respectively (Fig. 4.9a-b). The ZACF3-CSS demonstrated significantly greater rigidity compared to previously reported structural supercapacitors (Fig. 4.9c) [3, 96, 97, 130]. This enhancement in mechanical performance can be ascribed to the structural integrity of the ZACF3-CSS, which effectively integrates the carbon fiber electrodes and polymer electrolyte with reinforced carbon fibers. To further demonstrate the practical application of the

ZACF3-CSS, a 10 kg weight was placed on the suspended device (Fig. 4.9d). Remarkably, the device exhibited no obvious bending or deformation under this substantial load when powering an LED.

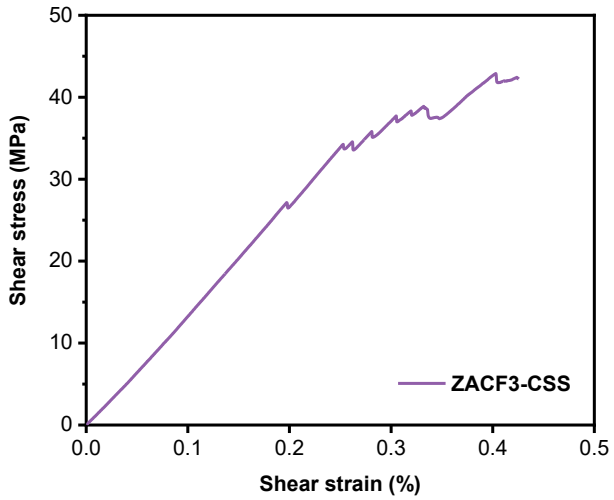


**Figure 4.10** Short beam shear tests of ZACF3-CSS.

The interfacial bonding between the multiple layers of ZACF3-CSS plays a crucial role in determining load transfer efficiency and mechanical performance. To assess the interfacial force, short beam shear tests were conducted to measure the shear stress. Shear stress represents the frictional resistance that inhibits the relative sliding between layers along a shared neutral axis [55]. Higher shear stress indicates increased frictional resistance, facilitating more efficient force transfer between the layers. The ZACF3-CSS exhibited a shear stress of 27.0 MPa (Fig. 4.10). Efficient force transfer between the layers is essential for maintaining structural integrity and distributing loads evenly throughout the device. When subjected to mechanical stresses, the strong interfacial bonding in the ZACF3-CSS prevents delamination, thereby improving the overall mechanical strength.

## 4.4 Coupling relationship between electrochemical and mechanical properties

To investigate the mechano-electrochemical coupling behavior of the ZACF3-CSS, an in situ study was conducted to evaluate the cycling performance under various constant external loads. The cycling stabilities of the ZACF3-CSS under different flexural stresses are shown in Fig. 4.11a-b. The ZACF3-CSS demonstrated stable cycling performance for the initial 1000 cycles under a flexural stress of 30 MPa. The SEM image of the device after the 1000 cycles (Fig. 4.11d) showed no discernible cracks or structural damage, closely resembling the pristine sample before the test (Fig. 4.11c). This observation indicates that the ZACF3-CSS can maintain its structural integrity and electrochemical performance under moderate flexural stress. With increasing flexural stress to 50 MPa, the cycling performance of the ZACF3-CSS experienced a minor decline but still maintained good capacity retention and the SEM analysis (Fig. 4.11e) revealed the development of some minimal cracks in the energy storage unit. Despite the presence of these minor defects, the ZACF3-CSS continued to operate effectively, demonstrating its robustness under increased mechanical stress. When the flexural stress was further increased to 70 MPa, the ZACF3-CSS exhibited a significant reduction in capacity, retaining only 81.8% of its initial value. The SEM images (Fig. 4.11f) revealed the presence of serious cracks in the energy storage unit, which could be attributed to the sudden capacity drop. In contrast, the capacity retention of the device without load remained 100% after 3000 cycles, suggesting that high flexural stress can induce structural damage to degrade cycling performance.

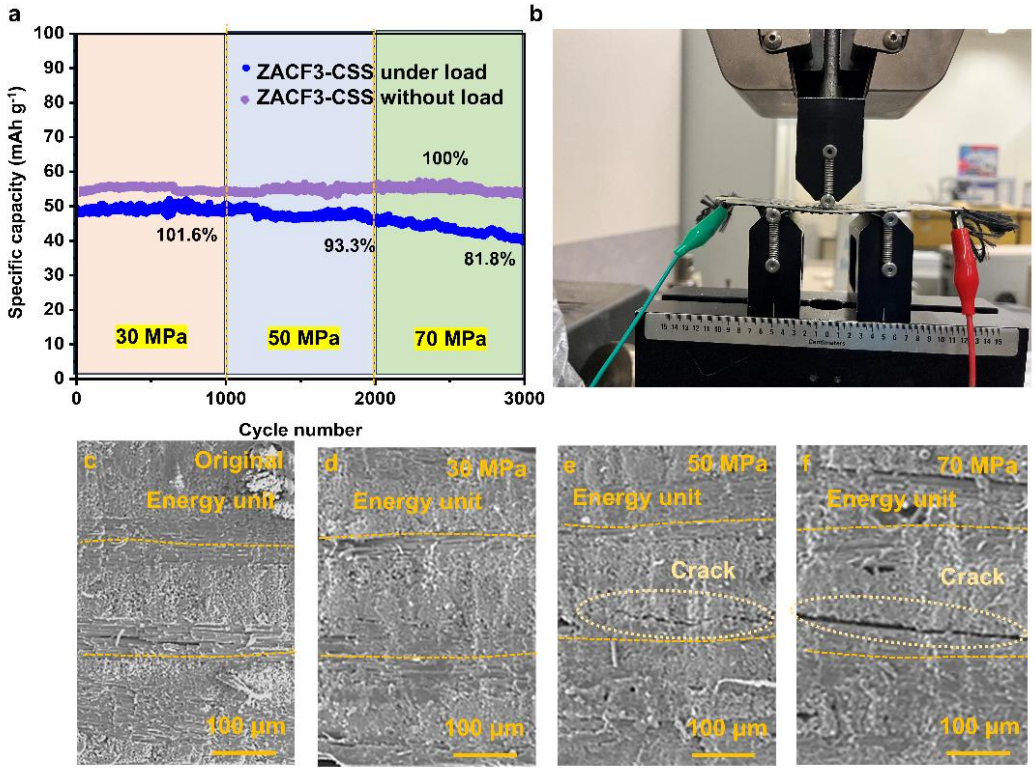


**Figure 4.11** (a) In situ mechano-electrochemical characterization of ZACF3-CSS under various flexural stresses. (b) Experimental configuration of the in situ mechano-electrochemical testing system. (c-f) Cross-sectional SEM images of ZACF3-CSS before and after cycling under different stresses.

As the flexural stress was further increased from 30 to 50 and 70 MPa, the integrity of the inner regions was destroyed. The development of structural defects within the energy storage unit led to the gradual decline of cycling performance without a sudden break. The crack propagation under applied stress demonstrates the coupling between electrochemical and mechanical behavior.

## 4.5 Simulation results for electro-fatigue failure

The numerical simulation was implemented using COMSOL Multiphysics 5.5 to investigate the effect of the charge-discharge process on the fatigue failure and

mechano-electrochemical coupling behavior of CSS. The energy storage unit in CSS undergoes changes in internal ion concentration distribution as zinc ions shuttle between anode and cathode during the charge-discharge process (Fig. 4.12). Simultaneously, for both electrode and electrolyte materials, the intercalation/deintercalation of zinc ions induces volume changes. The corresponding strain fields were derived from the calculated concentration distribution using the material-specific volumetric expansion coefficients ($\beta$). As shown in Fig. 4.12, these strain variations generate stress fields within the energy unit of CSS. For example, in the inset images of Fig. 4.12, the different Zn ion concentration distributions at different charge times induce different stresses. The peak internal stress during charging was found to be around 60 MPa, and this stress was observed to correspondingly increase and decrease following the charge-discharge process of CSS. Through these charge-discharge cycles, such alternating internal stress variations can result in mechanical fatigue. Given its electrochemical origin, this phenomenon is termed electrochemical cycling-induced fatigue or simply electro-fatigue.

It was experimentally observed that the capacity decreased and an inner crack occurred, propagating as the applied loads increased. To validate the relationship between this failure and electro-fatigue, the 3D mechanical model of CSS was built to investigate the fatigue performance under various three-point bending load conditions. The stress fields of the 2D electrochemical model were propagated to the 3D model along the width direction of the CSS.

**Table 4.2** Electrochemical mechanical variables and values in the Multiphysics model

| Parameter | Symbol | Value |
|---|---|---|
| Maximum Zn ion concentration of anode/cathode | $c_{max,a}$ /$c_{max,c}$ | 18000 mol/m$^3$ |
| Initial Zn ion concentration of anode/cathode | $c_{0,a}/c_{0,c}$ | 10/9497 mol/m$^3$ |
| Conductivity[131] of CF | $\sigma_{cf}$ | 58800 S/m |
| Conductivity of polymer electrolyte[132] | $\sigma_{SE}$ | 3 S/m |
| Current density | $i$ | 1 C |
| Equilibrium potential of energy unit when SOC=0/SOC=1 | $E_{eq,0}$ / $E_{eq,1}$ | 0.2/1.8 V |
| The molar mass of lithium | $M$ | 65.38 g/mol |
| Modulus of CFs of anode/cathode | $E_{cf,a}/E_{cf,c}$ | 230 GPa |
| Modulus of polymer electrolyte | $E_{pe}$ | 10 MPa |
| Swelling coefficient of CFs of anode/cathode [133] | $\beta_{cf,a}/\beta_{cf,c}$ | $1.846\times10^{-3}$ m$^3$/kg |

| | | |
|---|---|---|
| Swelling coefficient of polymer electrolyte [134] | $\beta_{pe}$ | $5.31\times10^{-3}$ $m^3/kg$ |

Note: the additional subscript *a* stands for anode, and *c* stands for cathode

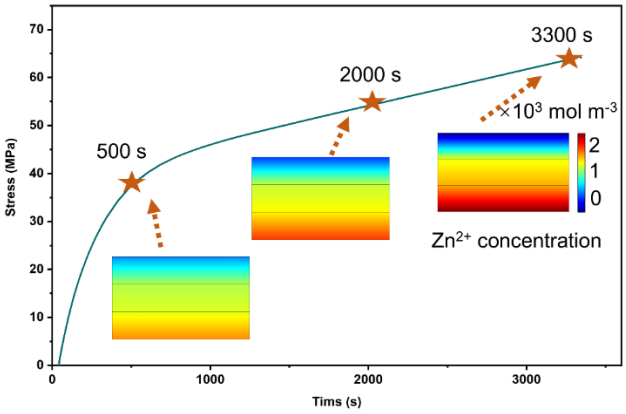


**Figure 4.12** Different stresses induced by the Zn ion concentration distribution gradient. The inserted pictures representing the Zn ion concentration distribution at charge times of 500 s, 2000 s, and 3300 s, respectively, generating different stresses.

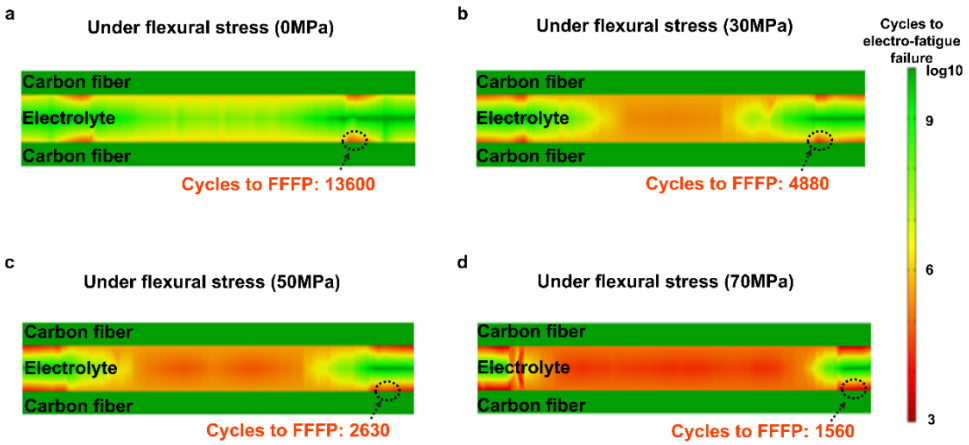


**Figure 4.13** Simulation results of cycles to fatigue failure distributed in an energy storage unit under different flexural stress: (a) 0 MPa, first fatigue failure point (FFFP) occurred at 13600 cycles; (b) 30 MPa, FFFP occurred at 4880 cycles; (c) 50 MPa, FFFP occurred at 2630 cycles; (d) 70 MPa, FFFP occurred at 1560 cycles.

To achieve a reliable simulation of the fatigue failure process of the energy unit in CSS, material-specific S-N curves were assigned for both the carbon fiber and electrolyte components, with parameters derived from validated data in existing literature [106, 135]. Through fatigue simulation based on S-N curves, the fatigue life of the energy unit in CSS was successfully simulated and predicted under combined electrochemical cycling loading and mechanical loading. Detailed parameter settings are provided in the Table 4.1.

As illustrated in Fig. 4.13a, the first fatigue failure point was observed after 13,600 cycles without mechanical load, which was solely attributed to electro-fatigue during the charge-discharge process. When constant stresses of 30, 50, and 70 MPa were applied, the cycles to the first fatigue failure point were significantly reduced to 4,880, 2,630, and 1,560 cycles, respectively (Fig. 4.13b-d). Additionally, the area corresponding to the lower cycle range was found to increase, indicating the coupling effect between external force and electro-fatigue stress, which accelerated the failure process. The results demonstrated that the fatigue stress induced by electrochemical cycling was coupled with external mechanical stress, increasing aggregated fatigue stress and promoting structural failure.

## 4.6 Summary

The electrochemical cycling induced-fatigue failure and the mechano-electrochemical coupling effect were investigated. The fabricated ZACF3-CSS exhibited an energy density of 39.2 Wh $kg^{-1}$ at a power density of 80.8 W $kg^{-1}$ at 0.2 A $g^{-1}$ and a flexural strength of 282.9 MPa. It showed a cycling stability with a capacity retention of 100% after 3000 cycles without mechanical load. The in situ mechano-electrochemical analysis revealed that, under varying applied loads from 30 to 70 MPa, the ZACF3-

CSS maintains a capacity retention of 81.8% after 3000 cycles. The SEM images showed progressive cracks developed as the flexural stress increased. The simulation results elucidated the electrochemical declination caused by the electro-fatigue stress, which originates from the Zn ion concentration gradient. It is also demonstrated that the flexural stress accelerates the electro-fatigue failure, causing a reduction in electrochemical stability. The electro-fatigue failure and coupling relationship between mechanical and electrochemical properties highlight the design and application conditions for these devices to achieve optimal electrochemical and mechanical performance in real-world applications.

# Chapter 5 Electrode/Electrolyte Interface Structure Design for CSSs

In chapter 5, the energy unit with the snap-on buckle structure of electrode and hydrogel electrolyte interface is integrated into a complex matrix to enhance the interlocked effect. The improved adhesive bonding contributes to load transfer without sacrificing of electrochemical performance. The specific capacitance of PAM-I-CSS is high at 98.2 F $g^{-1}$ at 0.5 A $g^{-1}$ and it retains stable capacitance after 8500 cycles even under a three-point bending test. This demonstrates that strong bonding at the electrode/electrolyte interface is crucial for maintaining excellent electrochemical performance under mechanical bending by minimizing shear movement between layers. Simulation results show that the snap-on structure exhibits lower stress distribution than the sandwich structure at the electrode/electrolyte interface due to the interlocked interface facilitating load transfer. Practical applications also indicate that the unique structure enables a new design of composite structural devices, making them promising for use in electric vehicles, electric aircraft, and other fields.

## 5.1 Introduction

Over the past decades, energy storage devices have been applied in various fields, such as portable electronics and electric vehicle storage [136, 137]. Energy devices with high energy and power densities have become crucial for the progression of energy storage technologies. On top of that, realizing weight or volume reductions and additional functionalities in energy storage devices is beneficial for the fabrication of novel energy storage materials, such as composite structural energy storage

components, which can simultaneously provide energy and bear loads [112, 138]. To date, typical structural devices encompass composite structural batteries and supercapacitors, which have been employed in a wide range of applications, including volume- and weight-restricted electric vehicles and aviation [1, 2, 11, 13, 139].

Compared to composite structural batteries, CSSs exhibit significant potential applications due to their higher power density [140, 141]. CSSs can be constructed using structural supercapacitors (SSs), especially the layered structure of SSs, which contains reinforced units that are suitable for load-bearing. The multi-functionality of the structural composite can be achieved not only by the structure design that addresses weight-loading and maintains the electrochemical performance of the electrode but also by improving the electrochemical performance and mechanical properties of both the electrode and electrolyte [142-144].

The conventional CSSs are composed of three parts: carbon fiber-based electrodes, polymer electrolytes, and structural units [98]. The structure units typically consist of carbon fiber reinforcement materials that provide mechanical strength, ensuring the device can bear loads. For the energy unit structure, the sandwich structure is commonly employed in which the carbon fiber electrode and quasi-solid-state electrolyte are bonded layer by layer. This structure makes it challenging to achieve dense contact between the carbon fiber electrode and hydrogel electrolyte, leading to weakened adhesion and low mechanical strength due to interlayer sliding [9, 145, 146].The high shear stress of the CSS device indicates that these layers, likely sharing a common neutral axis, effectively transfer loads throughout the system, resulting in significant rigidity and excellent flexural strength [11, 55]. In order to enhance the adhesion, various unique structures have been proposed in other research [147, 148],

such as polymer rivets to mechanically stabilize the electrode layer stack [23], or tree-root-like lamination at the electrode/separator interface [55]. However, these structures either significantly reduce the energy density of the whole device or fail to provide sufficient mechanical strength. Besides, other special structures have been proposed to strengthen adhesive bonding by immersing nanowires in epoxy, forming an interlocking effect at the bonding interface in composite structure [149, 150].

Here, the snap-on structure was fabricated to interlock the electrode/electrolyte interface, thereby preventing sliding between multiple layers in energy unit. Then the unique energy structure fabricated by the in-situ polymerization process is integrated into high strength CFRP composites to form PAM-I-CSS. The structure of sandwich energy unit without the snap-on structure is integrated into the reinforced composite using the same methodology, resulting in the formation of the CSS (PAM-S-CSS). Then the two structures of electrode and electrolyte interface in CSS devices are investigated and compared. The snap-on structure CSS can enhance adhesive bonding, resulting in improved shear strength. The dense shear interaction enables the multiple layers to share a nearly common neutral axis, thereby allowing effective load transfers in the battery laminate during a three-point bending test, ultimately enhancing the overall mechanical properties [149, 151].

To better understand the impact of the electrode/electrolyte interface strength on mechanical properties, finite element analysis (FEA) simulation of the stress state model of the energy unit under bending was conducted. The comprehensive simulation analysis of the stress distribution at the electrode/electrolyte interface provides valuable insights into the mechanical behavior under bending loads. By comparing these two structures, it can be demonstrated that the interlock interface more

effectively transfers load than the sandwich structure. Furthermore, the influence of load transfer efficiency at the electrode/electrolyte interface on Young's modulus and shear modulus was explored.

Electrochemical characterizations reveal that the snap-on structure possesses high flexural strength and delivers energy density comparable to other structural batteries. To deeply understand the interaction between mechanical performance and electrochemical properties, in-situ mechano-electrochemical tests were employed. These tests demonstrate that the strong adhesive bonding of PAM-I-CSS provides high specific capacitance and stable cycling performance, even under external bending. Finally, the practical application of the structural energy device is demonstrated by using the PAM-I-CSS device to drive a fan while bearing heavy loads. This highlights the high electrochemical performance and load-bearing capability of the device. Therefore, the composite device including snap-on structure interface in energy units can be widely applied in practical fields due to its improved flexural strength with minimal compromise to electrochemical performance.

## 5.2 Fabrication and performance of snap-on structure CSS

As illustrated in Fig. 5.1a, the snap-on structure is fabricated through the in-situ polymerization of hydrogel electrolyte on the carbon fiber electrode. The electrode and electrolyte are layered to form the sandwich structure. The snap-on buckle contains a convex button and a concave button corresponding to the carbon fiber and hydrogel electrolyte, respectively, as clearly seen in the cross-section views (Fig. 5.1b and 5.1c). The snap-on structure provides a robust interface between the carbon fiber and hydrogel electrolyte, ensuring strong adhesion and mechanical stability. The optical image further elucidates the structural details (Fig. 5.1d-f). The pores in the carbon

cloth are devoid of hydrogel in the sandwich structure, while the pores are filled with an appropriate amount of gel to form a protruding bump-like locking structure on the other side of the carbon cloth, significantly increasing the adhesive strength between electrode and electrolyte. The filling of the pores in the carbon cloth with hydrogel electrolyte not only increases the adhesive strength but also enhances the overall mechanical properties of the composite, making it more resilient to mechanical deformation and stress. The bonding interface, as shown in Fig. 5.1g-h, demonstrates robust lamination between the electrolyte and the electrode, thereby improving the mechanical rigidity of the entire system. The robust lamination between the electrolyte and electrode ensures that the composite can withstand mechanical forces without delamination or degradation. This strong interfacial bonding is achieved through the in-situ polymerization process, which promotes the formation of a snap-on buckle structure between the hydrogel electrolyte and the carbon fibers. This results in a composite material with superior mechanical rigidity and durability.

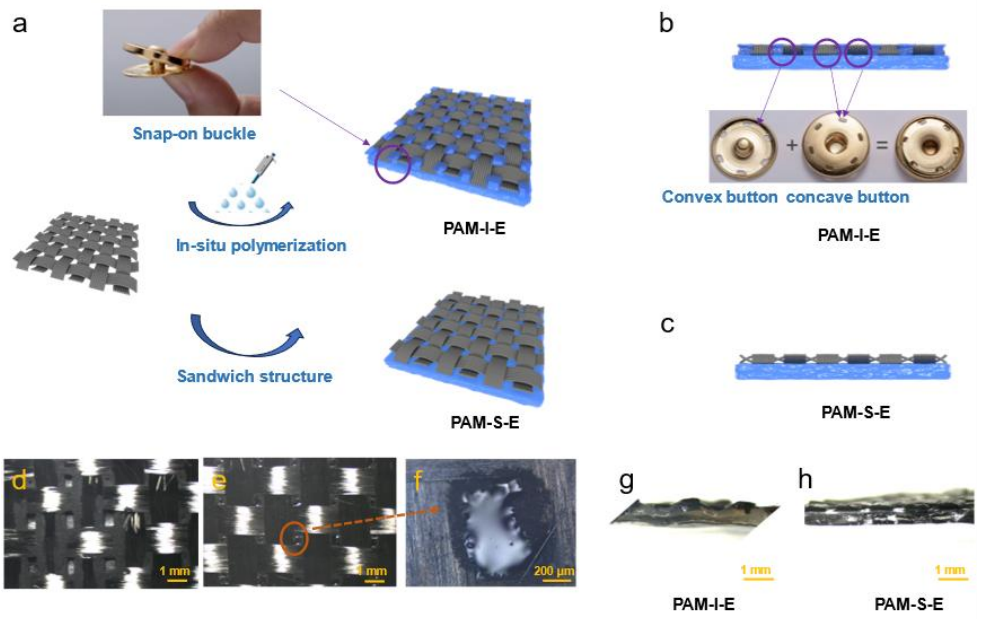

**Figure 5.1** Schematic diagram of the formation of snap-on buckle and sandwich structures at the electrolyte and electrode. (a) Schematic illustration of the formation process. (b) Detailed schematic of snap-on buckle structure. (c) Detailed schematic of sandwich structure. (d) Optical image of sandwich structure. (e) Optical image of snap-on buckle structure. (f) Magnified optical image of snap-on buckle structure. (g) Cross-sectional view of snap-on buckle and sandwich structures.

As shown in Fig. 5.2a, the composite structural supercapacitor devices were fabricated using the wet lay-up composite manufacturing technique. The energy unit was integrated into the center of CFs and glass fabric, providing mechanical strength while maintaining electrochemical performance. The device with the snap-on structure containing the electrolyte fabricated by the in-situ polymerization is denoted as the PAM-I-CSS and the device with sandwich structure is denoted as PAM-S-CSS. The CV curves of PAM-I-CSS were measured at different scan rates ranging from 5 mV $S^{-1}$ to 40 mV $S^{-1}$, maintaining almost identical shapes, which indicates a rapid charge transfer rate and quick kinetics (Fig. 5.2b). The nearly identical shapes of the CV curves imply rapid charge transfer in the device. The GCD curves at different current densities, as exhibited in Fig. 5.2c, reveal a specific capacitance of 98.2 F $g^{-1}$ at 0.5 A $g^{-1}$. The linearity and symmetry of the GCD curves further confirm the excellent electrochemical stability and efficiency (87.1%) of the structure. The high-rate performance of PAM-I-CSS is presented in Fig. 5.2d, showing a very high specific capacitance of 71.3 F $g^{-1}$ at 5 A $g^{-1}$. This high-rate capability is essential for applications that require rapid energy delivery, such as in power tools and auxiliary energy source for electric vehicle batteries.

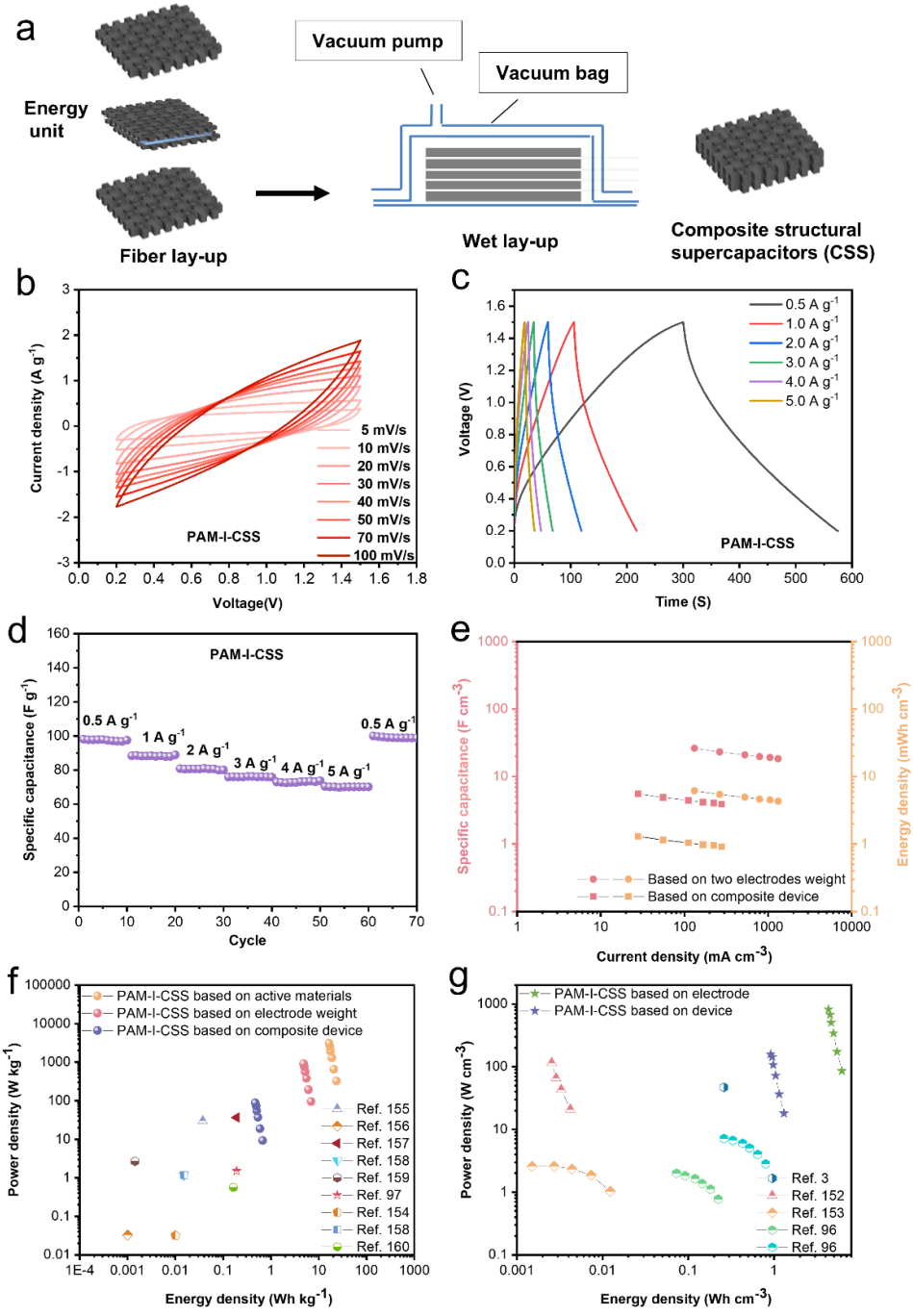


**Figure 5.2** (a) Schematic illustration of CSS device fabrication. (b) The CV curves of the PAM-I-CSS at different scan rates. (c) The GCD curves of the PAM-I-CSS at different current densities. (d) Rate performance of PAM-I-CSS. (e) Volumetric specific capacitance and energy density for PAM-I-CSS. The Ragone plots of PAM-

I-CSS compared with other data based on (f) weight and (g) volume.

The volumetric, gravimetric, and areal specific capacitance and energy density are further shown in Fig. 5.2e and Fig. 5.3a-b. The volumetric, gravimetric, and areal specific capacities (5.56 F $cm^{-3}$, 2.857 F $g^{-1}$, and 860 mF $cm^{-2}$), energy densities (1.305 mWh $cm^{-3}$, 0.671 Wh $kg^{-1}$, and 0.202 mWh $cm^{-2}$) and power densities (18.07 mW $cm^{-3}$, 9.284 W $kg^{-1}$, and 2.80 mW $cm^{-2}$) are calculated based on the whole device of PAM-I-CSS, including energy unit and carbon fiber epoxy composite. As shown in Fig. 5.2f-g and Fig. 5.3c, the Ragone profiles based on weight, volume [3, 96, 152, 153], and area indicate that the PAM-I-CSS exhibits superior energy density to other recently reported ones (Table 5.1), calculated with active materials, electrodes, or composite device. These results provide a comprehensive understanding of the device's performance, considering different scales and dimensions. The high specific capacities and energy densities make it a promising candidate for various energy storage applications.

To further quantify the multifunctionality of CSSs, the multifunctional efficiency is proposed in Eq. (5.1) to assess its potential application [5]. The multifunctional efficiency is calculated as shown in Eq. (5.1)

$$\eta_{ME} = \eta_M + \eta_E \tag{5.1}$$

where $\eta_{ME}$ represents the multifunctional efficiency. $\eta_M$ is the mechanical efficiency, defined as the ratio of the structural devices' mechanical performance (such as flexural modulus and strength) to that of pure carbon fiber reinforced polymer (CFRP) without energy unit. $\eta_E$ is the value of the specific capacitance of CSS without deformation to the capacitance of cell-level supercapacitor with liquid electrolyte.

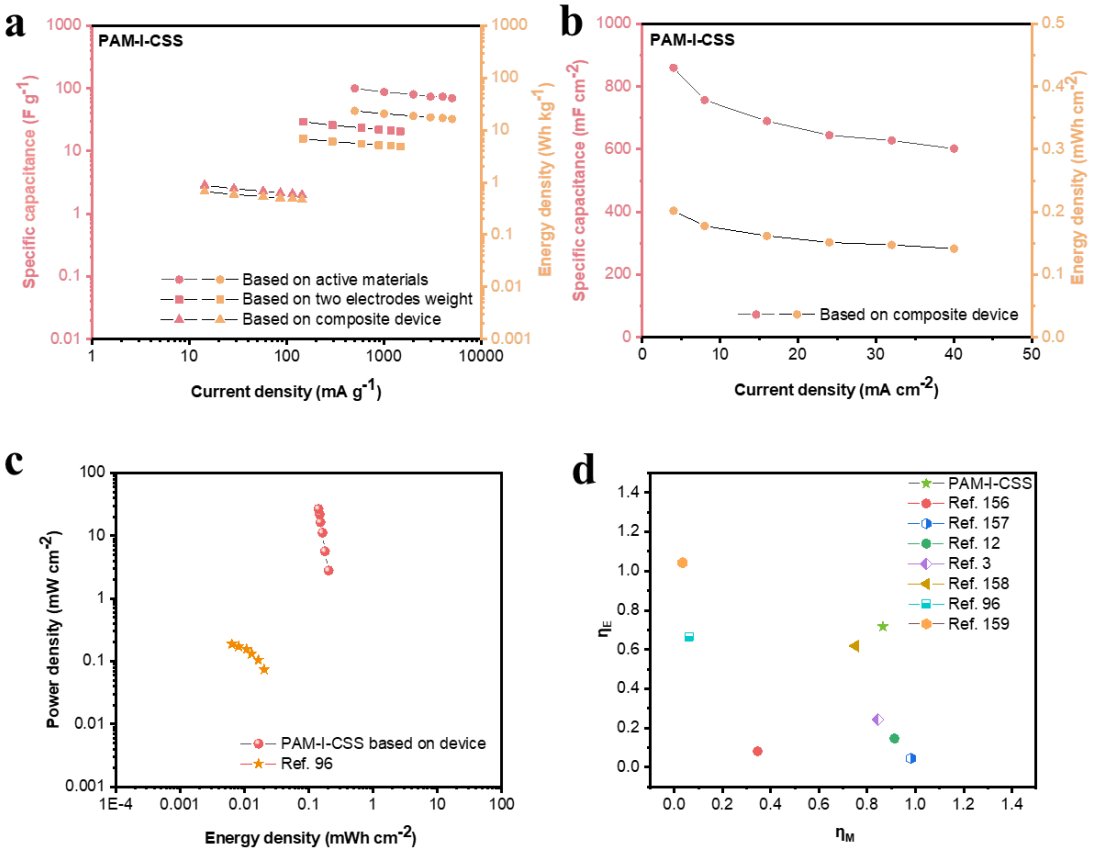


**Figure 5.3** (a) The gravimetric specific capacitance and energy density for PAM-I-CSS. (b) The areal specific capacitance and energy density for PAM-I-CSS. (c) The Ragone plots of PAM-I-CSS compared with other data based on area. (d) The Ragone profile for the multifunctional efficiencies of PAM-I-CSS and other research results.

The PAM-S-CSS device in this study achieves 86.5% of the flexural strength of the baseline sample, along with 71.7% of the areal capacitance of the supercapacitor in liquid electrolyte. where $\eta_{ME}$ represents the multifunctional efficiency. $\eta_M$ is the mechanical efficiency, defined as the ratio of the structural devices' mechanical performance (such as flexural modulus and strength) to that of pure carbon fiber reinforced polymer (CFRP) without energy unit. $\eta_E$ is the value of the specific

capacitance of CSS without deformation to the capacitance of cell-level supercapacitor with liquid electrolyte. As a result, the defined multifunctional efficiency $\eta_{ME}$ is approximately 1.58 (>1), indicating that our multifunctional devices could reduce the overall weight compared to conventional integrated systems that include separate mechanical and electrochemical components [3, 156]. The Ragone plots comparing the multifunctional efficiency of PAM-I-CSS with other literature data are shown in Fig. 5.3d [3, 12, 96, 156-159], indicating that our device exhibits the highest multifunctional efficiency. Therefore, it is evident that the PAM-I-CSS we fabricated is a promising candidate for practical applications in multifunctional structural energy storage.

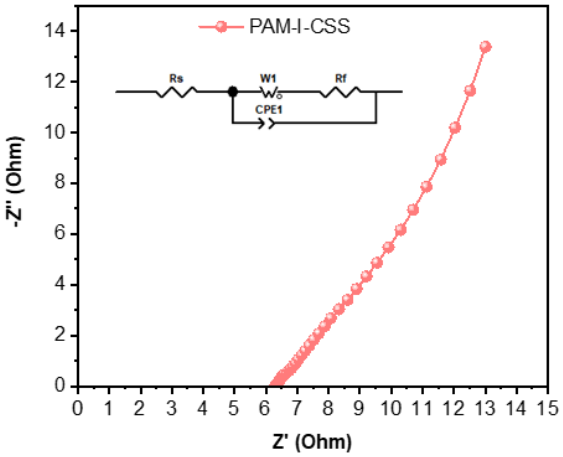


**Figure 5.4** The EIS test for the PAM-I-CSS device.

The EIS result is shown in Fig. 5.4 and the inset is the equivalent circuit diagram. The Rs of the PAM-I-CSS is only about 6.29 Ω, which is much smaller than that reported in other literature [97], indicating a high ion transport rate, in line with the excellent electrochemical performance.

**Table 5.1** Comparison of energy density and power density in this work with other CSSs previously reported in the literature.

| CSSs | Energy density ($Wh \cdot kg^{-1}$) | Power density ($W \cdot kg^{-1}$) | Ref. |
|---|---|---|---|
| CNT fiber/Polymer electrolyte interleaves | 0.375[b] | 30[b] | [160] |
| CAG-CF | 0.001[b] | 0.0328 [b] | [157] |
| Cu–Co selenide nanowire CF/GF/SPE | 0.1916[a] | 36.65[a] | [161] |
| $SnO_2$-CSS | 0.01506[d] | 1.16[d] | [162] |
| ACF/PEGDGE/LiTFSI/IL/GF | 0.00143[c] | 2.68[c] | [163] |
| 5:5 NiCo-LDH-CSS | 0.191[d] | 1.508[d] | [97] |
| CF/CNT/MTM57+EMIMTFSI | 0.01[d] | 0.032[d] | [156] |
| SnO2-NR/WCF | 0.01506[d] | 1.160[d] | [162] |
| Optimized SZSC | 0.1646[d] | 0.5633[d] | [164] |
| PAM-I-CSS | 23.47[a] | 324.97[a] | This work |
| PAM-I-CSS | 6.903[b] | 95.58[b] | This work |
| PAM-I-CSS | 0.671[d] | 9.284[d] | This work |

[a] Normalized based on active materials.

[b] Normalized based on electrode weight.

[c] Normalized based on total cell weight of electrodes, electrolyte, and separator.

[d] Normalized based on composite device.

## 5.3 Simulation results of PAM-S-CSS and PAM-I-CSS

The interfacial adhesion between the electrode and electrolyte is crucial due to fractures caused by the external loading, which leads to the degradation of the electrochemical performance. Fig. 5.5a displays a digital image of the in-situ mechano-electrochemical tests, which measure electrochemical performance under a three-point bending test. The interfacial force between the electrode and hydrogel electrolyte within the energy unit is essential for both electrochemical performance and mechanical properties. As shown in Fig. 5.5b, the interfacial adhesion in the sandwich structure is derived from the simple contact between the carbon fiber electrode and hydrogel electrolyte. In contrast, the carbon fiber and hydrogel electrolyte are interlocked in the snap-on structure. The peeling test is further conducted to evaluate the interfacial adhesion between the electrode and electrolyte in the energy unit (Fig. 5.5c) [154, 155]. The peeling force of the energy unit with sandwich structure is approximately 7 N, exhibiting a relatively smooth curve. In contrast, sharp peaks are observed in the curve, and the peeling force of the energy unit with snap-on structure, approximately 30 N, is about four times higher than that of the sandwich structure energy unit, demonstrating a stronger interfacial force. The stronger adhesion allows the entire energy unit to have higher mechanical strength and more effective force transfer.

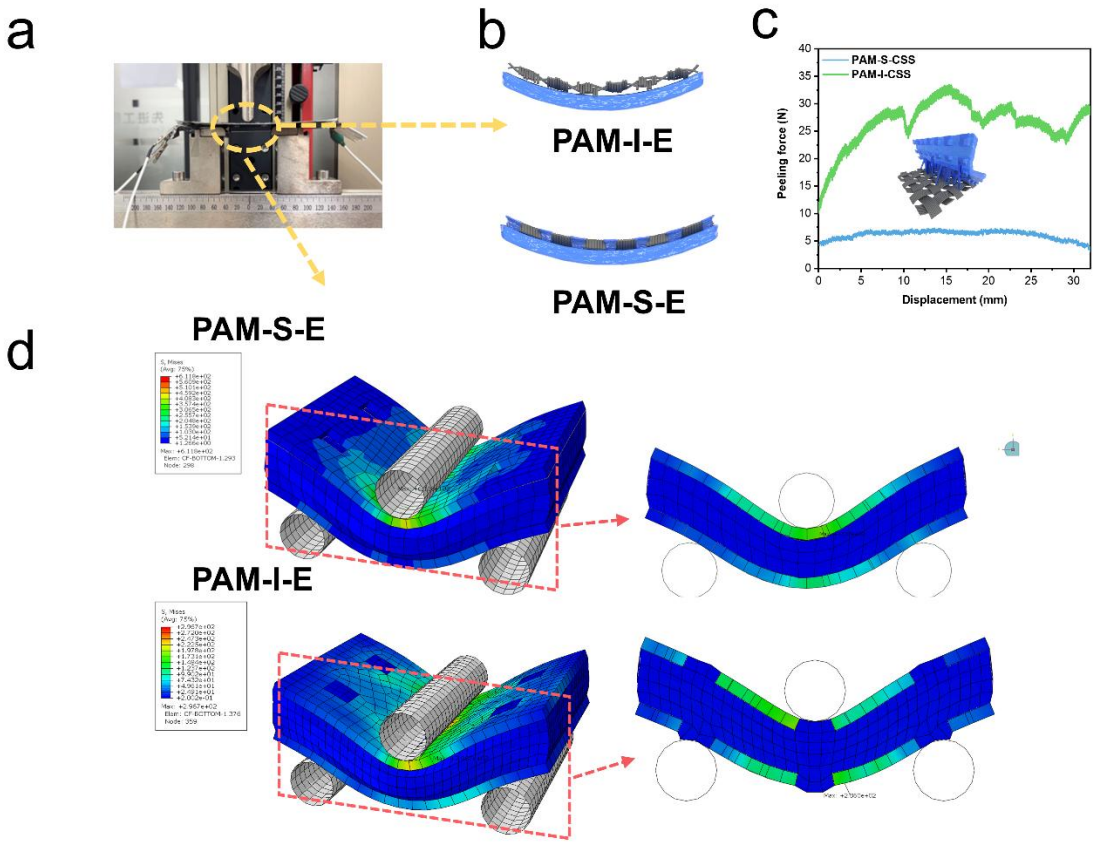


**Figure 5.5** (a) Digital image of three-point bending test. (b) Schematic illustration of a cross-sectional view of the hydrogel electrolyte in configurations PAM-S-CSS and PAM-I-CSS under deformation. (c) Results of the 180° peeling-off test at the electrode-electrolyte interfaces, including an inset image depicting the peeling process of a robust interface attributed to the snap-on buckle structure. (d) Simulation results illustrating force transfer across the electrode-electrolyte interface during the three-point bending test with the corresponding cross-sectional region of the device depicted in the left figure.

The simulation relating to force transfer in the snap-on structure and sandwich structure was thoroughly investigated to demonstrate how adhesion force strengthens the mechanical performance of the structural device. To deeply understand the impact of the electrode/electrolyte interface structure on the mechanical strength of the whole

system, the ABAQUS finite element (FE) software was employed to simulate the three-point bending test of the energy unit within the reinforcement complex. During the application of external force to the entire system, the energy unit bears a relatively small proportion of load, leading to degradation of the electrode/electrolyte boundary or electrolyte. Meanwhile, the reinforcement complex bears the majority of the load. To represent the loading condition of the electrode/electrolyte boundary, the FE analysis focuses on the energy unit rather than the entire device, as the reinforcement parts of the two structures are identical. The simulation models are depicted in Fig. 5.6.

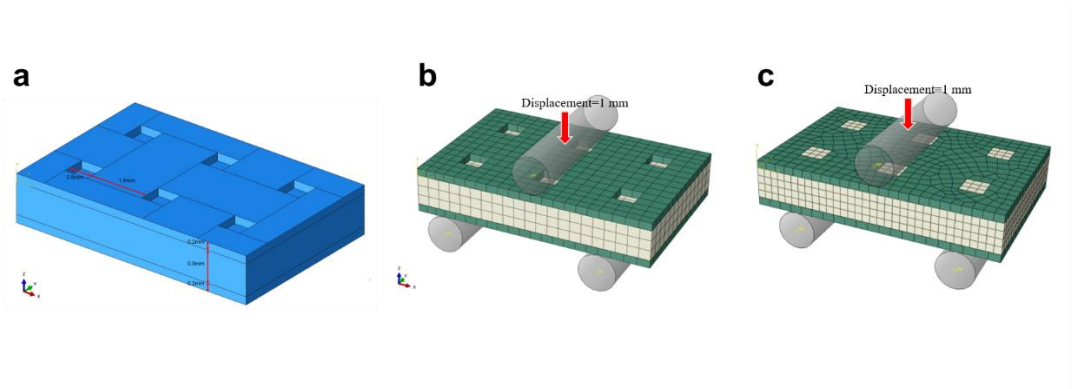


**Figure 5.6** The simulation model of (a) the energy unit, (b) PAM-S-E, and (c) PAM-I-E.

To replicate real test conditions, the thickness of both the electrode and electrolyte is set to 0.2 mm and 0.8 mm, respectively. The side length of the square hole on the carbon cloth is 0.6 mm, with active materials coated on one side. During the simulation, the boundary conditions of the model are consistent with those of the three-point bending experiment. To prevent displacement of the sample, the supports at the bottom are completely fixed, and the compressors at the top are located on the symmetry surface of the sample, restricting all degrees of freedom except for the translational motion in the Z-direction. Additionally, the model is loaded by applying Z-direction

displacement to its reference point. Furthermore, the cohesive zone model (CZM) is applied to simulate the interface failure [165]. The cohesive force contact model permits a certain degree of relative sliding and separation at the contact interface. This simulation method more accurately reflects the stress distribution and physical response within the structural capacitor, simulating the complex state of the interface under external mechanical loading.

The simulation results are presented in Fig. 5.5d. For the same deflection of 1 mm, the force at the electrode/electrolyte interface of PAM-S-E is concentrated at the center, exhibiting the highest flexural strength of 611.8 MPa. In contrast, the force at the electrode/electrolyte interface of PAM-I-E is evenly distributed around the center with the highest flexural strength of 296.7 MPa. This phenomenon is more clearly observed in the cross-section view of the simulation results. The snap-on structure of the electrode/electrolyte interface allows the effective load transfer between multiple layers by evenly distributing the force over a larger area compared to the sandwich structure, thereby providing stable electrode/electrolyte interface for electrochemical performance under loading.

## 5.4 In-situ mechano-electrochemical tests of PAM-S-CSS and PAM-I-CSS

To further elaborate, the in-situ mechano-electrochemical tests provide critical insights into the durability and reliability of the energy storage devices under mechanical stress. The in-situ mechano-electrochemical tests were conducted to measure the cycling performance of PAM-S-CSS and PAM-I-CSS with the three-point bending test (Fig. 5.7a). The specific capacitance of PAM-S-CSS decreased from 85.5 F $g^{-1}$ to 64.62 F

$g^{-1}$, with a capacitance retention of approximately 75.58% after 8500 cycles. In contrast, the PAM-I-CSS delivered a stable cycling performance, with a slight decrease in specific capacitance from 97.37 F $g^{-1}$ to 91.7 F $g^{-1}$, maintaining a capacitance retention of 94.18% after 8500 cycles. To gain a deeper understanding of the structural integrity under the external force, SEM images were taken to show the transverse cross-sections of PAM-S-CSS and PAM-I-CSS before and after cycling. As shown in the insets of Fig 5.7a, the snap-on structure in PAM-I-CSS has a cross-locked interface, while the sandwich structure in PAM-S-CSS shows a parallel interface of carbon fiber and electrolyte. After 8500 cycles, the interface of PAM-I-CSS maintained the same structure as the initial state under constant three-point bending. Conversely, small cracks appeared in the interface of PAM-S-CSS, indicating that the sandwich structure is more susceptible to external constant load than the snap-on buckle structure with the locked interface. The observed degradation in the specific capacitance of the sandwich structure highlights the limitations of the parallel interface design, which is prone to crack formation and subsequent specific capacitance loss under mechanical loading. On the other hand, the cross-locked interface in snap-on structure demonstrates superior mechanical stability, as evidenced by the minimal structural changes observed in the SEM images after 8500 cycles. This robust interface design not only prevents crack formation but also ensures consistent load distribution, thereby maintaining the electrochemical performance of the device. The practical application of the PAM-I-CSS is demonstrated in Fig. 5.7b. The suspended device is strong enough to support a heavy substance. Furthermore, the suspended PAM-I-CSS could power a small fan under the loading of the heavy objects. By adopting a cross-locked interface, it is possible to achieve a balance between mechanical strength and electrochemical performance, making these devices suitable for demanding

applications such as drones, vehicles, and aerospace technologies.

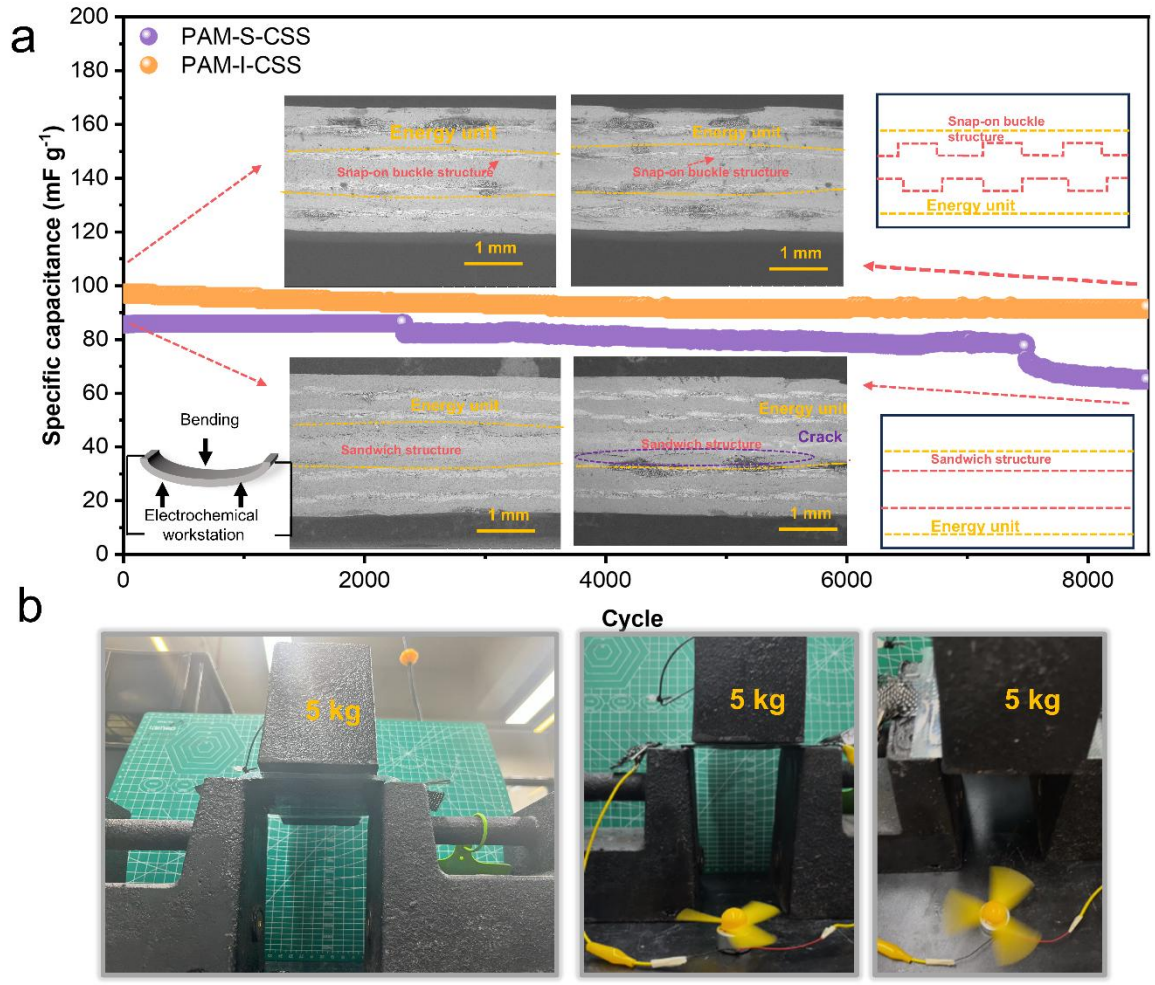


**Figure 5.7** (a) In-situ mechano-electrochemical measurement of the PAM-I-CSS and PAM-S-CSS. Insets present the SEM images of PAM-I-CSS and PAM-S-CSS before and after cycling (side view). (b) Demonstration of the practical application of PAM-I-CSS under external load, illustrating its capability to power a small fan.

To thoroughly investigate the impact of the snap-on buckle structure on the mechanical strength of the structural device, three-point bending and short beam tests were evaluated to explore the primary failure mechanism under external force. The interfacial adhesion of multiple layers stacked in a CSS is a crucial factor in

determining the rigidity of the structural device. This is because higher interfacial adhesion force can inhibit the interlayer sliding. In this way, these layers, sharing a common neutral axis, effectively transfer loads between different layers. When the interfacial adhesion is strong, the shear stress can be effectively transferred from one layer to another, thereby enhancing the overall shear strength of the composite. Conversely, weak interfacial adhesion results in poor stress transfer, leading to delamination and reduced shear strength [55]. Short beam shear test was set up to measure the shear strength of the device. From the SEM images of the central area (Fig. 5.8a) or the side area (Fig. 5.8b) of the fractured PAM-S-CSS sample, significant delamination is observed between the carbon fiber and hydrogel electrolyte interface, indicating that the main failure mechanism under the shear stress is weak interfacial adhesion. On the other hand, failure predominantly formed around the edge area in the reinforcement unit, without delamination in the central area (Fig. 5.8c) and the side area (Fig. 5.8d) of the PAM-I-CSS energy unit layers. This indicates more effective load transfer arising from the rigid adhesive force between the electrode and electrolyte interface. As a result, the shear stress of PAM-I-CSS is 55.61 MPa, which is higher than that of PAM-S-CSS (36.23 MPa), as seen in Fig. 5.8i. The higher shear stress observed in the PAM-I-CSS sample than that in the PAM-S-CSS sample indicates that the interfacial adhesion plays a pivotal role in enhancing shear strength. The stronger interfacial adhesion solidly bonds different components, effectively facilitating load transfer and demonstrating greater flexural strength [11].

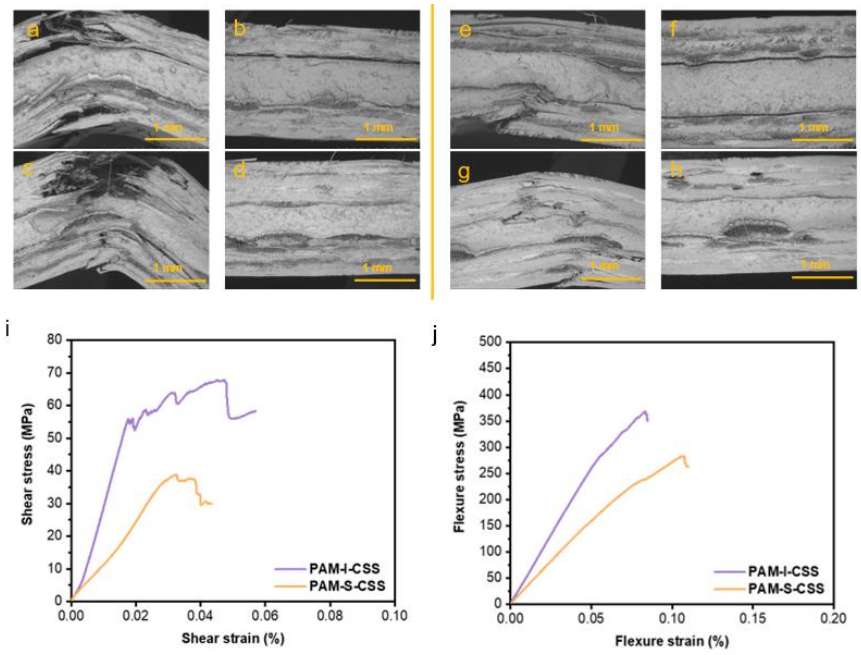


**Figure 5.8** The SEM images of the middle part (a, c) and edge part (b, d) of fractured three-point bending PAM-I-CSS and PAM-S-CSS devices. The SEM images of the middle area (e, g) and side area (f, h) of fractured PAM-I-CSS and PAM-S-CSS devices after a short beam test. (i) Shear stress profiles of the PAM-I-CSS and PAM-S-CSS devices. (j) The three-point bending test curves of the PAM-I-CSS and PAM-S-CSS devices. Moreover, the three-point bending test results highlight the importance of interfacial adhesion in determining the flexural strength of composite structures. The observed delamination, especially in the intralayer between the carbon fiber electrode and the hydrogel electrolyte, appears to be the governing failure mechanism after the three-point bending test in PAM-S-CSS, as exhibited in the middle area (Fig. 5.8e) and side area (Fig. 5.8f). High flexural strength is corroborated by the layers of the reinforcement unit (the matrix-fiber) in the middle part (Fig. 5.8g), along with the lack of obvious delamination between the electrode and electrolyte (Fig. 5.8h). This indicates that the locked structure between the carbon fiber electrode and the hydrogel electrolyte can affect load transfer in multiple layers, which fairly conforms to the

simulation results, leading to higher mechanical strength of PAM-I-CSS. Moreover, the locked interface was too strong to be delaminated, which altered the main failure mechanism for the PAM-I-CSS. This enhanced the flexural stress and flexural modulus, which increased considerably from 282.21 MPa and 26.34 GPa, respectively, for the PAM-S-CSS to 367.92 MPa and 44.34 GPa, respectively, for the PAM-I-CSS, as seen in Fig. 5.8j. Consequently, the snap-on buckle structure in PAM-I-CSS with strong interfacial adhesion significantly enhances the shear strength and load transfer efficiency of composite structures. Optimizing interfacial properties through interlock bonding design can further improve mechanical performance.

## 5.5 Summary

Although balancing electrochemical properties and mechanical strength is challenging, our designed snap-on structure device obtains excellent performance with a specific capacitance of 98.2 F $g^{-1}$, energy density of 23.47 Wh $kg^{-1}$, and power density of 324.97 W $kg^{-1}$ at 0.5 A $g^{-1}$, without significantly sacrificing flexural modulus and flexural strength. The high electrochemical performance can be attributed to the energy unit and the strengthened adhesive bonding, which successfully transfers loads across multiple layers of the electrode stack. An in-situ study of electro-chemo-mechanical coupling was conducted to understand the impact of external force on capacitance retention, measuring electrochemical performance of the devices under 3-pont bending test. The capacitance remains at 94.18% after 8500 cycles under constant load, manifesting that the device possesses excellent electrochemical performance under high mechanical loads. The method of fabricating multilayered devices is simple and economical, making it suitable for industrial production.

# Chapter 6 Stabilizing the Spatial Distribution of Electric Field

In Chapter 6, an MXene-based electrolyte for Zn-ion-based hybrid CSS to effectively modulate the electric field distribution through a polarized electric field formed by hydrogen bonds between MXene and polymer chains. In situ mechano-electrochemical performance and simulation results indicate that the MXene-based CSS maintains a more uniform electric field under bending conditions (at a strain of 0.5%) compared to devices without MXene. The designed CSS delivers a specific capacity of 101 mAh $g^{-1}$ at a current density of 0.2 A $g^{-1}$. The energy density of the device reaches 80 Wh $kg^{-1}$ at the power density of 163.3 W $kg^{-1}$, which is about nine times higher than the best result previously achieved (9.3 Wh $kg^{-1}$). Integrating MXene into the electrolyte offers a practical approach to regulating electric field distribution, potentially paving the way to design high-performance structural power sources capable of functioning under deformation.

## 6.1 Introduction

The increasing energy density requirements for batteries remain a critical challenge in the advancement of electric transportation. This challenge can be overcome through lightweight design, which increases the mileage of electric vehicles and promotes the industrialization of electric aircraft [166]. Multifunctional CSSs, which store electrochemical energy, can simultaneously substitute structural components by carrying the mechanical load, minimizing the overall system mass [138, 167].Compared with composite structural batteries [14], CSSs offer superior power

density and a longer lifespan, making them more suitable for integrated structural systems without the need for frequent and undesirable replacements.

The architectural strategies of CSSs can be broadly classified into two categories: cell-level and material-level designs [14]. The former involves supercapacitors sandwiched between reinforced CF composites [6]. In this design, the external non-capacity reinforcement withstands the primary mechanical stress, while the internal supercapacitor bears only a minimal part of the load. For instance, Moyer *et al.* used a traditional composite layup process to sandwich lithium-ion batteries between epoxy-impregnated CFs. They achieved an energy density of 36 Wh $kg^{-1}$ and a Young's modulus of 1.8 GPa [28]. In contrast, the material-level design approach integrates multifunctional materials, including all mechanically robust structural carbon fiber current collectors, electrodes, and electrolytes, into CSSs to achieve enhanced mechanical performance [8]. Despite the improved mechanical properties of these structural materials, they must be carefully developed to avoid compromising electrochemical performance [14]. These structural devices have achieved acceptable results by balancing both electrochemical and mechanical performance. For example, an all-carbon-fiber-based structural lithium-ion battery in full-cell configuration achieved a high energy density of 75 Wh $kg^{-1}$ and an elastic modulus of 76 GPa [168]. Thus, material-level design can more accurately capture the essence of structural and multifunctional components.

Recently, deformation during working conditions has been shown to severely affect the stability of the electric field intensity, exacerbating dendrite issues in flexible Zn-ion batteries [169]. For example, Li *et al.* demonstrated that deformation caused by different operational modes can induce perturbations in the electric field within Zn-

ion flexible batteries [169]. They found that the Zn anode exhibited a non-uniform electric field in curved regions compared with the planar configuration. Any uneven local electric field intensity may trigger dendrite growth, leading to low Coulombic efficiency (CE) and reduced cell lifespan [169, 170]. Analogously, deformation in CSSs under external loading induces heterogeneous electric field distributions. Therefore, maintaining a uniform electric field is essential for improving the electrochemical performance of CSSs. MXene has been extensively used in solid electrolytes to inhibit the Zn dendrite growth due to its enhanced dielectric constant, which accelerates zinc salt dissociation and ion transport through a locally polarized electric field effect [171]. Moreover, incorporating dielectric MXene is expected to facilitate the dissociation of alkali metal salts [171, 172]. For instance, Zhang *et al.* proposed a built-in electric field strategy by adding MXene to solid electrolyte in lithium-metal batteries, achieving stable operation for 6000 hours at 0.1 mA $cm^{-2}$ and remarkable cycling stability, even at 4.6V [172]. The MXene-bonded transport network offers significant potential opportunity for developing electrolytes in CSSs, which has yet to be fully explored.

Considering the application of multifunctional materials under bending conditions, a Zn-ion material-level hybrid CSS system with MXene-based electrolyte was fabricated to mitigate the perturbations in electric field. In situ mechano-electrochemical measurements and simulations show that the polarized electric field, generated through hydrogen bonds between MXene and polymer chains, effectively modulates the electric field distribution within CSS under mechanical stress. Furthermore, MXene significantly enhances the ionic conductivity of electrolytes and improves mechanical properties. The MXene-based CSS exhibits a specific energy of

80 Wh $kg^{-1}$ and a flexural modulus of 33.8 GPa. Even under a three-point bending test (at a strain of 0.5%), the device achieved a capacity retention of 90.4% after 10,000 mechanical load cycles. Overall, we present a feasible strategy to decrease the impact of mechanical disturbances on electric field intensity in our CSS systems, thereby ensuring stable and exceptional electrochemical performance.

## 6.2 Electrochemical performance and multifunctionality of CSSs

Schematic illustration of the preparation process for the MXene-bonded electrolyte is exhibited in Fig. 6.1a and the images of WIS-P and WIS-P-M are shown in Fig. 6.1b-d. The results of morphology (Fig. 6.2a-c) and crystal structure (Fig. 6.2d) show the MXene nanosheet with high crystallization. The SEM was applied to analyze the morphology of the polymer electrolytes. Compared with the MXene-free electrolyte, the electrolyte incorporating MXene has smaller pores (Fig. 6.3), which is attributed to the hydrogen bonds between MXene and the polymer to promote the crosslinking of the polymer chains. Furthermore, the elemental mapping images indicate that MXene nanosheets are well dispersed within the polymer membrane.

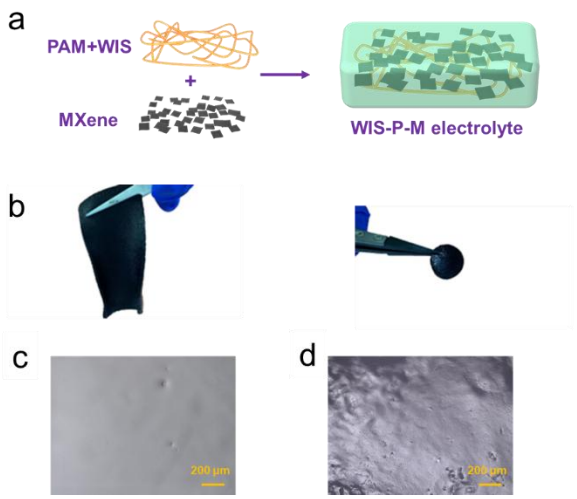


**Figure 6.1** (a) Schematic illustration of the preparation process for the MXene-bonded electrolyte. (b) Images of WIS-P-M electrolyte. Optical images of (c) WIS-P and (d) WIS-P-M electrolyte.

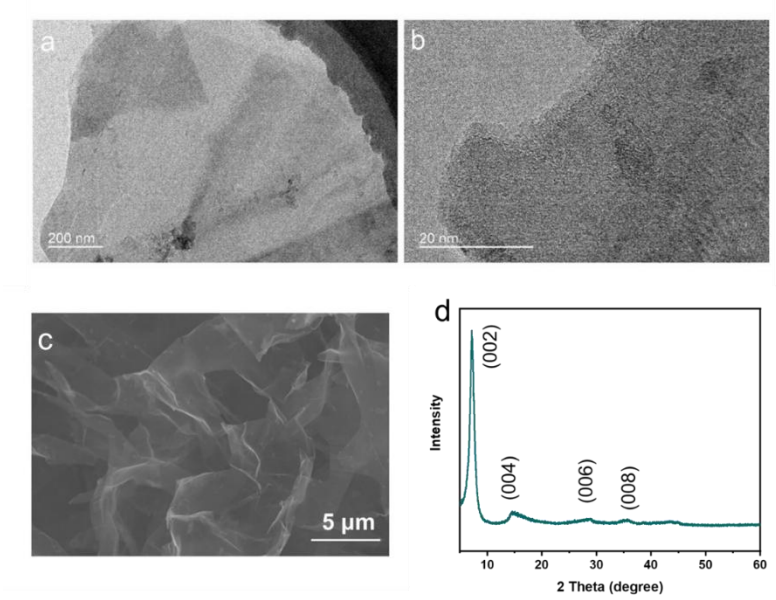


**Figure 6.2.** (a-b) TEM images, (c) SEM image, and (d) XRD pattern of the $Ti_3C_2T_x$ MXene nanosheets.

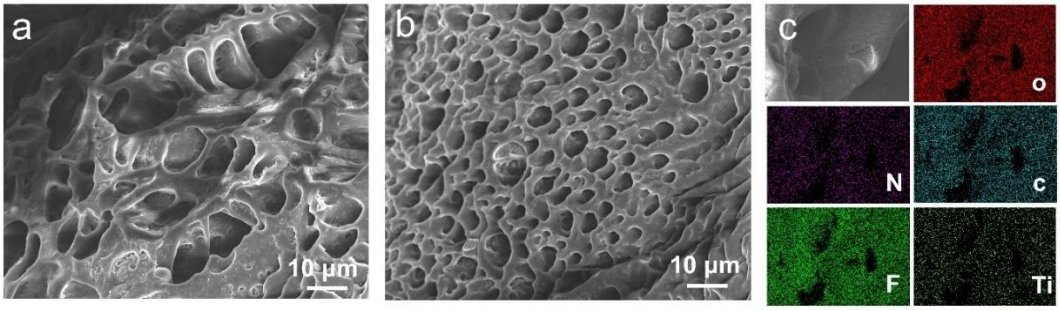


**Figure 6.3** SEM images of the (a) MXene-free and (b) MXene-based polymer electrolytes and (c) corresponding mapping images.

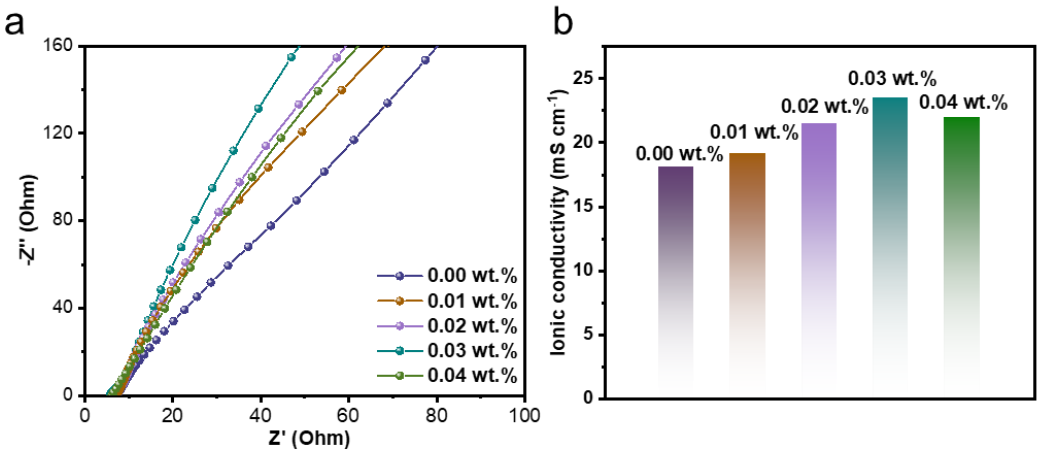


**Figure 6.4** (a) EIS and (b) Ionic conductivity of electrolytes with different MXene contents.

The effect of the additive amount of MXene on the ionic conductivity of electrolytes was systematically investigated by preparing 0.00 wt.%, 0.01 wt.%, 0.02 wt.%, 0.03 wt.%, and 0.04 wt.% MXene-containing electrolytes. As illustrated in Fig. 6.4a, the electrolyte resistances tend to increase at first and then decrease with the increased content of MXene. When the addition of the MXene is 0.03 wt.%, the optimum ionic conductivity of the electrolyte is 23.5 mS $cm^{-1}$, attributed to the enhanced ion transport facilitated by MXene additives (Fig. 6.4b). The surface-terminating groups of MXene

(-F, -O) facilitate $Zn^{2+}$ adsorption through electrostatic interactions, substantially reducing ionic diffusion barriers and promotes charge carrier mobility, and enhancing the electrochemical plating/stripping kinetics. Therefore, by establishing shortened $Zn^{2+}$ pathways and facilitating strong $Zn^{2+}$ adsorption, the incorporation of MXene in electrolyte significantly enhances $Zn^{2+}$ conductivity. While the excess addition of MXene limits the improvement of conductivity due to the agglomeration of MXene.

The electrochemical performance and multifunctionality of CSSs, both with and without MXene, were evaluated. The CSSs were fabricated using a wet lay-up method, which incorporated CFs-AC, Zn foil, structural polymer electrolytes with and without MXene, and reinforced carbon fibers, then cured at ambient temperature under vacuum conditions (Fig. 6.5a). Fig. 6.5b depicts the GCD curves of the MXene-based CSS (WIS-P-M CSS) at current densities of 0.2-1.5 A $g^{-1}$, exhibiting symmetrical triangular shapes. As the current density increased, a noticeable decline in capacity was observed. Furthermore, Fig. 6.5c shows the cycling performance of WIS-P-M CSS and CSS without MXene (WIS-P CSS) at a current density of 0.4 A $g^{-1}$. Notably, the WIS-P-M CSS retained approximately 98.0% of its initial specific capacity (85.0 mAh $g^{-1}$) and the WIS-P CSS achieved a 97.0% capacity retention of its initial value (75.81 mAh $g^{-1}$) after 5000 cycles, indicating that both the WIS-P-M CSS and WIS-P CSS delivered excellent capacity retention without external mechanical load. As illustrated in Fig. 6.5d, the specific capacity and energy density of WIS-P-M CSS were calculated based on mass, of the active material, electrode, and composite device. Based on the active material, the specific capacity of WIS-P-M CSS reached 101 mAh $g^{-1}$ at the current density of 0.2 A $g^{-1}$, and the energy density was 80 Wh $kg^{-1}$ at the power density of 163.3 W $kg^{-1}$. The specific capacity remained at 61.1 mAh $g^{-1}$ even

at 1.5 A $g^{-1}$, indicating excellent rate performance. Based on the entire device (including both the energy storage unit and composite part), the specific capacity of WIS-P-M CSS reaches 2.9 mAh $g^{-1}$ (or 5.6 mAh $cm^{-3}$, 1.9 F $cm^{-2}$) at a current density of 6 mA $g^{-1}$. The energy density was 2.3 Wh $kg^{-1}$ (4.5 Wh $cm^{-3}$, 0.7 Wh $cm^{-2}$) at a power density of 4.7 W $kg^{-1}$ (9.1 W $cm^{-3}$, 1.4 W $cm^{-2}$). Ragone plots (Fig. 6.5e) reveal that WIS-P-M CSS exhibits superior gravimetric energy and power densities compared to previously reported studies utilizing electroactive commercial CF electrodes. These improvements can be attributed to the unique structural design and the incorporation of MXene, which synergistically enhances the electrochemical performance of the device.

**Table 6.1** Comparison of energy density and power density parameters of the WIS-P-M CSS with other CSSs in literature.

| | Energy density ($Wh \cdot kg^{-1}$) | Power density ($W \cdot kg^{-1}$) | Ref. |
|---|---|---|---|
| CF/solid electrolyte interleaves | 0.169[b] | 20[b] | [128] |
| CuO-CF/GF/SPE | 0.10604[a] | 12.57[a] | [12] |
| GNP/CAG-CSS | 0.786[a] | 108[a] | [173] |
| CNT-infiltrated CF | 0.0016[d] | 0.193[d] | [174] |
| 5:5 NiCo-LDH-CSS | 0.191[d] | 1.508[d] | [97] |
| | 0.920[c] | 7.264[c] | [97] |

| | | | |
|---|---|---|---|
| | 9.269[a] | 73.18[a] | [97] |
| MnOOH-NWs@WCF | 0.00812[d] | 4.7368[d] | [175] |
| CF/CuO/PES+IL+LiS | 0.0166[d] | 269.2[d] | [161] |
| WIS-P-M | 80[a] | 163.27[a] | This work |
| | 23.528[b] | 48.016[b] | This work |
| | 2.286 [d] | 4.66[d] | This work |

[a] Normalized based on active materials.

[b] Normalized based on electrode mass.

[c] Normalized based on total cell mass of electrodes, electrolyte, and separator.

[d] Normalized based on composite device.

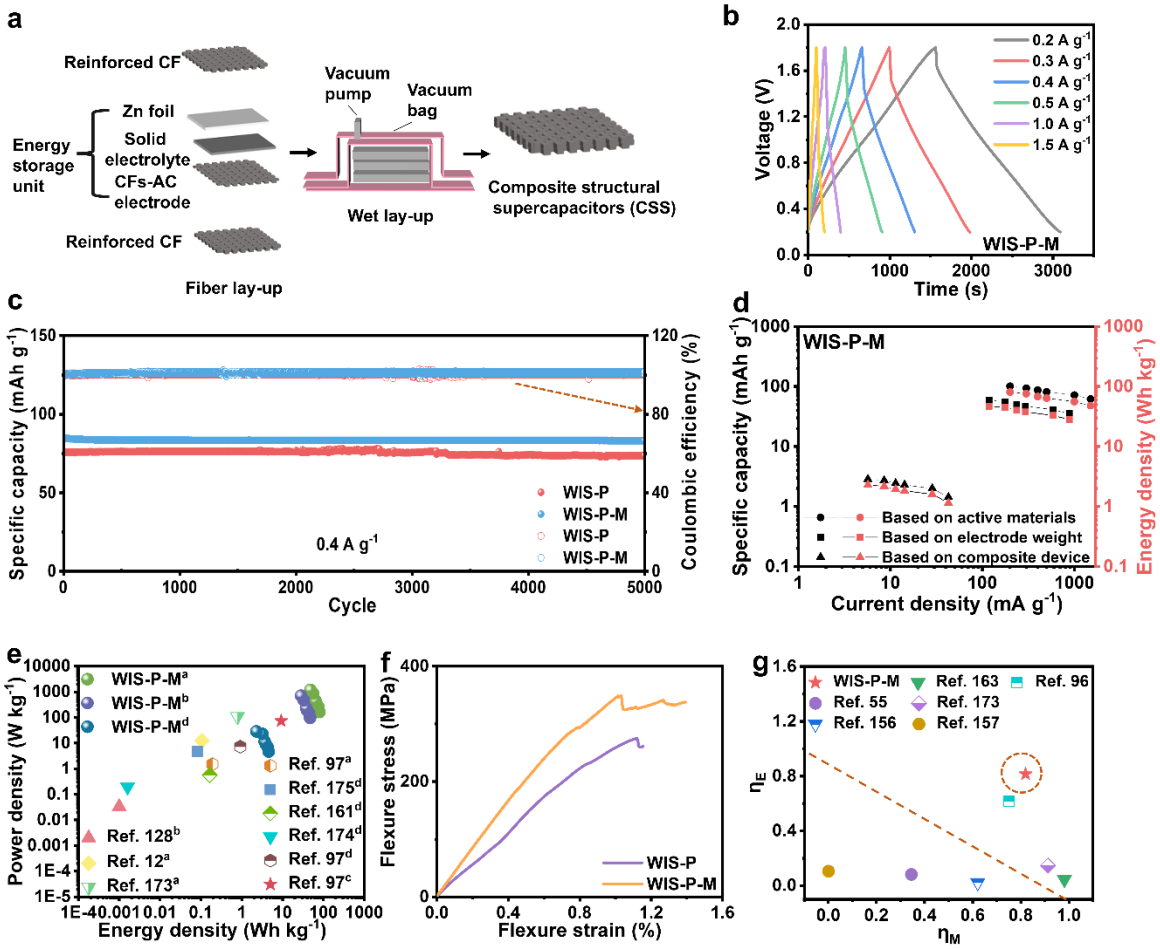


**Figure 6.5** Assembly, electrochemical performance, and multifunctionality of CSSs. (a) Schematic illustration of fabricated CSSs device. (b) GCD plots of WIS-P-M CSS. (c) Cycling performance of WIS-P-M and WIS-P CSSs. (d) Specific capacity and energy density of WIS-P-M CSS at different current densities. (e) Ragone plots of WIS-P-M CSS compared with other reported values (based on [a] active materials; [b] electrode mass; [c] total cell mass of electrodes, electrolyte, and separator; [d] composite device) (f) Three-point bending measurement of the CSSs. (g) Ragone plots of the multifunctional efficiency ($\eta_{ME}$) of WIS-P-M CSS compared with other studies.

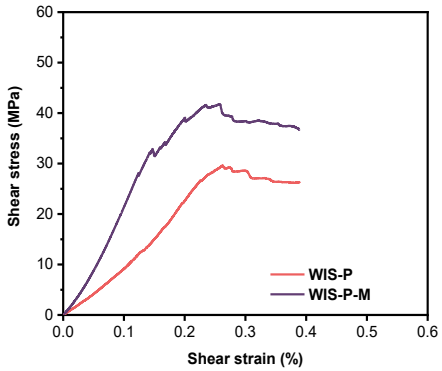


**Figure 6.6** Sheer stress curves of WIS-P-M and WIS-P CSSs.

The mechanical properties of the entire CSSs were systematically investigated, followed by a thorough assessment of their multifunctionality. The three-point bending tests revealed that the WIS-P-M CSS sample possesses a flexural strength of 350.1 MPa and a flexural modulus of 33.8 GPa, significantly exceeded the values of 274.8 MPa and 24.5 GPa observed for the WIS-P CSS, respectively (Fig. 6.5f). This represents increases of 27.4% in flexural strength and 37.9% in flexural modulus. This improvement is attributed to the formation of hydrogen bonds by the MXene additives. A short beam test was performed to assess the interfacial force between multiple layers and measure the shear stress. Higher shear stress values indicate increased frictional resistance to the sliding of components along a common neutral axis, thereby facilitating more efficient force transfer between layers. The WIS-P-M CSS demonstrated a superior shear stress of 32.9 MPa, 23.8% higher than the 26.6 MPa observed for WIS-P CSS (Fig. 6.6). These results suggest that incorporating MXene enhances the interfacial bonding and promotes more efficient force transfer between layers. To quantify the synergistic effects of mechanical and electrochemical properties, the concept of multifunctional efficiency ($\eta_{ME}$) was employed. According to previous studies [97], a $\eta_{ME}$ value exceeding 1 indicates that multifunctional

structural energy storage composites offer a weight-saving advantage compared to conventional monofunctional systems. The WIS-P-M CSS sample achieved a $\eta_{ME}$ of approximately 1.64, surpassing previously reported values (Fig. 6.5g). This result indicates that WIS-P-M CSS shows great potential as a promising candidate for practical multifunctional structural energy storage applications.

## 6.3 Mechanism of regulating electric field distribution

The dielectric measurements and simulation study shed light on the mechanism by which MXene nanofillers modulate the electric field in WIS-P-M CSS, as depicted in Fig. 6.7a. Previous research suggests that deformation leads to an uneven electric field distribution, characterized by higher field intensity in the central stressed areas compared to the less-stressed sides of the device [169]. The Fourier transform infrared spectrum (FTIR) spectra of WIS-P and WIS-P-M electrolytes were employed to confirm the interplay and bonding between MXene nanofiller and polymer chains (Fig. 6.8). The characteristic peaks at 3474 and 3376 $cm^{-1}$ are assigned to the stretching vibration of N-H in the WIS-P electrolyte. However, for the WIS-P-M, the peaks shift the lower wavenumber region to 3466 and 3376 $cm^{-1}$, which should be attributed to the formation of hydrogen bonds [176]. The hydrogen bond further forms dipolar under an external electric field [171]. The accumulation of these dipoles enhances the dielectric permittivity, thereby promoting mental salt dissociation and ion transport through localized electric field polarization. To test this hypothesis, the dielectric constants of electrolytes for both WIS-P-M and WIS-P CSSs were experimentally measured. The results revealed that the dielectric constant of WIS-P-M CSS at 40 Hz was 5724, significantly higher than the value of 1741 for WIS-P CSS (Fig. 6.7b). This substantial increase is attributed to the formation of hydrogen bonds between MXene

and polymer chains.

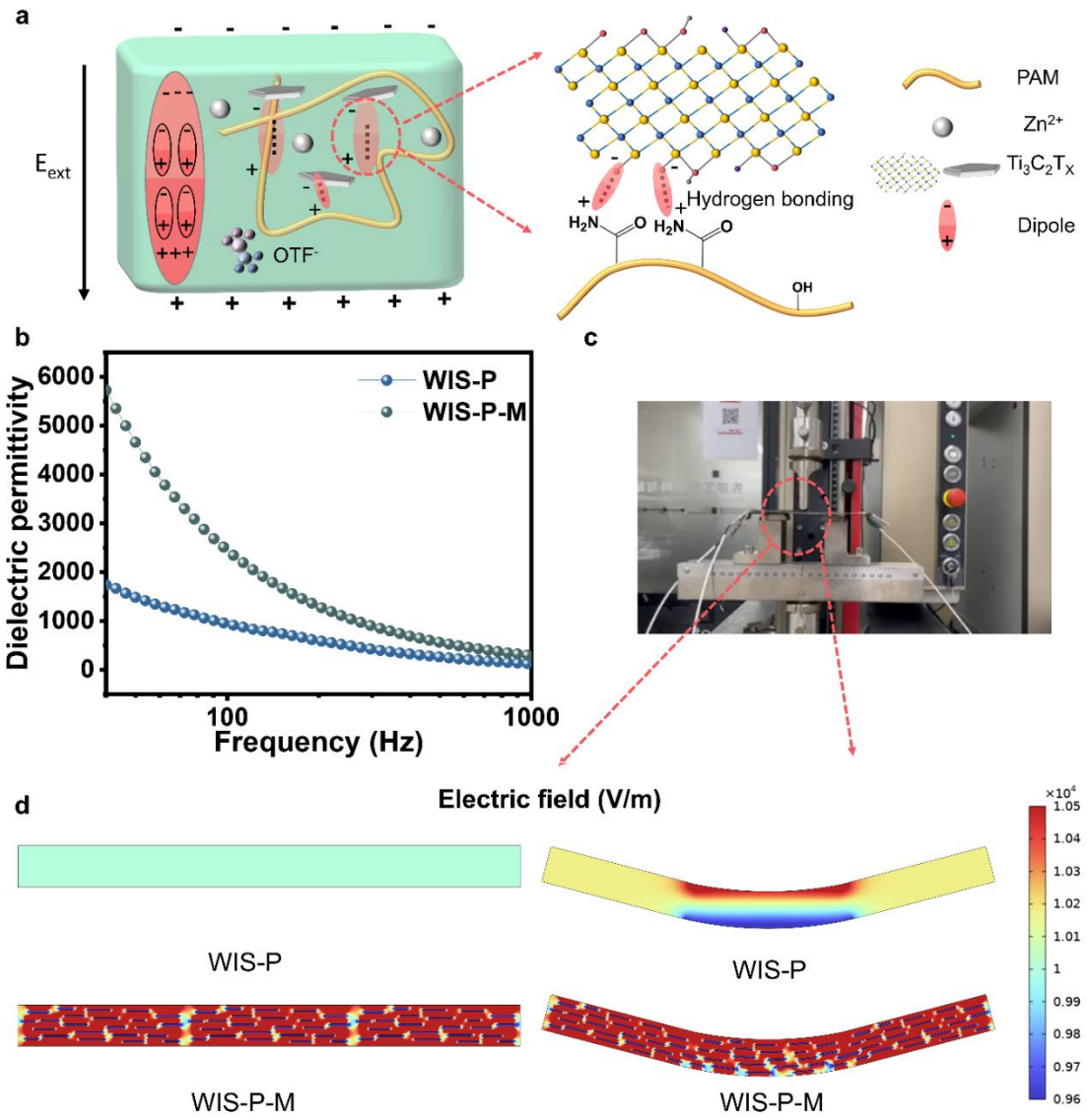


**Figure 6.7** Mechanism of regulating the electric field distribution in the MXene-based CSS. (a) Schematic illustration of the dipoles excited by the hydrogen bonds between MXene and polymer chain under an external electric field. (b) Dielectric constant of electrolyte for WIS-P and WIS-P-M CSSs. (c) Digital images of electrochemical testing of CSSs under three-point bending. (d) Simulation of the electric field distribution of CSSs under deformation.

COMSOL simulations were conducted to demonstrate the role of MXene in regulating the electric field distribution (Fig. 6.7d). The electric field intensity was calculated using spatial derivation ($\vec{E} = -\nabla_i V$) and conduction models $\overrightarrow{J_c} = \nabla \cdot \vec{E}$, assuming a bending curvature of 0.01. 3D simulation models and boundary conditions, and mesh independence verification were established (Fig. 6.9). Calculations were performed using COMSOL Multiphysics, employing the variation equation, with grid division achieved via the Galerkin method. The computational results show that, without external forces, both WIS-P-M and WIS-P CSSs exhibit relatively uniform electric fields. However, under deformation (bending), WIS-P CSS exhibits concentrated field intensity in the central most-stressed region. Moreover, both the coarse and fine grids exhibit the same simulation results, which confirm that MXene-induced dipoles effectively re-distribute the electric field, thereby reducing the impact of external mechanical load on electrochemical performance.

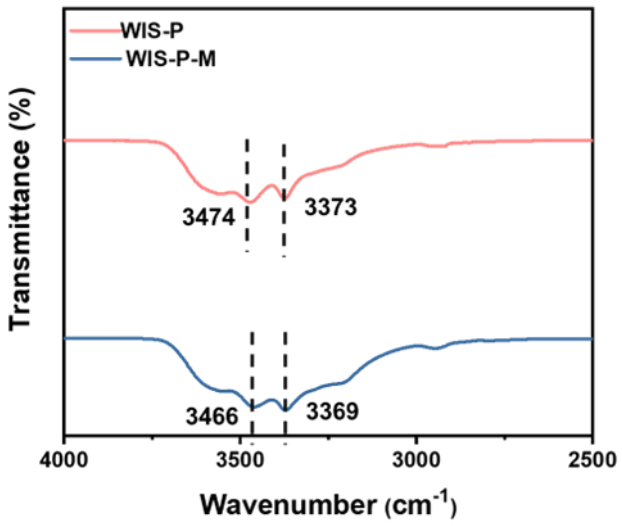


**Figure 6.8** FTIR spectra of WIS-P and WIS-P-M electrolytes.

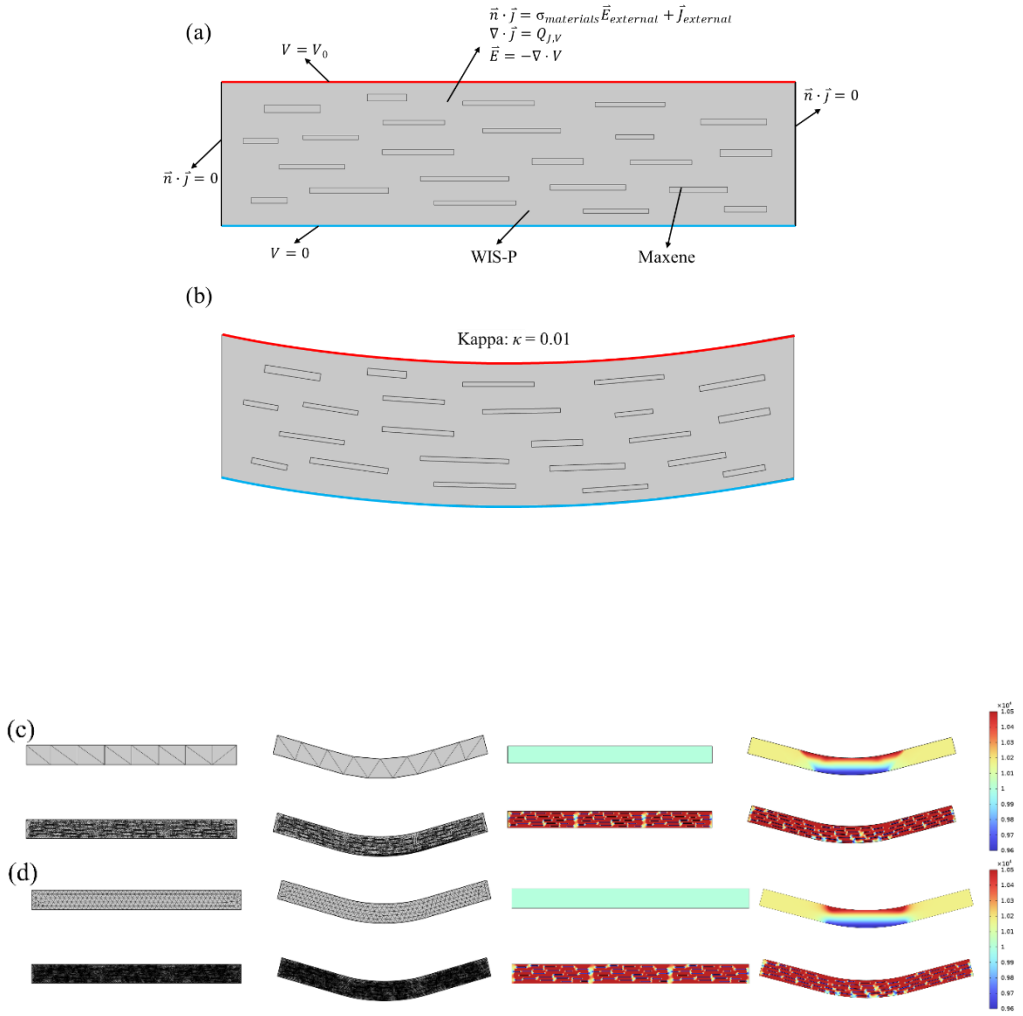


**Figure 6.9** Schematic diagram of (a) WIS-P and (b) WIS-P-M devices with boundary conditions for the COMSOL simulation; (c) Coarse and (d) fine mesh independence verification.

## 6.4 Effect of external deformation on electrochemical performance

The uniform electric field is crucial for mitigating Zn dendrite formation, which hinders the practical application of Zn batteries [171]. The growth of Zn dendrite is related to the electric field distribution. Uniform electric field accelerates even Zn deposition, suppressing Zn dendrite growth. This uneven electric field caused by the

Zn ion diffusion, side reaction and uneven Zn deposition. Fig. 6.11a depicts the impact of electric field distribution on Zn deposition. To validate the computational results, a Zn|Zn symmetric device was constructed to examine the Zn plating/stripping process under external mechanical load (at a strain of 0.5%), with an applied current density of 0.3 mA $cm^{-2}$ and a capacity of 0.1 mA h $cm^{-2}$ (Fig. 6.11b). The incorporation of MXene significantly improves the reversibility of Zn plating/stripping, as demonstrated by sustained operation exceeding 700 hours under continuous three-point bending without degradation. SEM images show the morphological evolution of cycled Zn foil regions within WIS-P-M and WIS-P symmetric devices (Fig. 6.11c-f). SEM analysis revealed that peripheral regions display smaller Zn flakes (Fig. 6.11d, 3f) compared to central areas (Fig. 6.11c, Fig. 6.11e), with the latter experiencing higher stress (strain). Furthermore, the WIS-P-M symmetric device demonstrates superior uniformity and smoothness in Zn deposition compared to the WIS-P device, which is attributed to the improved electric field uniformity, increased ionic conductivity, and enhanced ion transport properties of the WIS-P-M device.

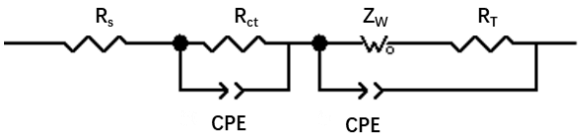


**Figure 6.10** The equivalent circuit used for EIS spectra fitting.

**Table 6.2** The fitting parameters of WIS-P and WIS-P-M CSS at various strains corresponding to the equivalent circuit.

| | $R_s$ | $R_{ct}$ | $Z_w$ |
|---|---|---|---|
| WIS-P-M-0% | 3.7 | 12.3 | 5.3 |

| | | | |
|---|---|---|---|
| WIS-P-M-0.5% | 3.8 | 16.9 | 16.6 |
| WIS-P-0% | 7.4 | 13.0 | 5.8 |
| WIS-P-0.5% | 7.4 | 33.1 | 59.8 |

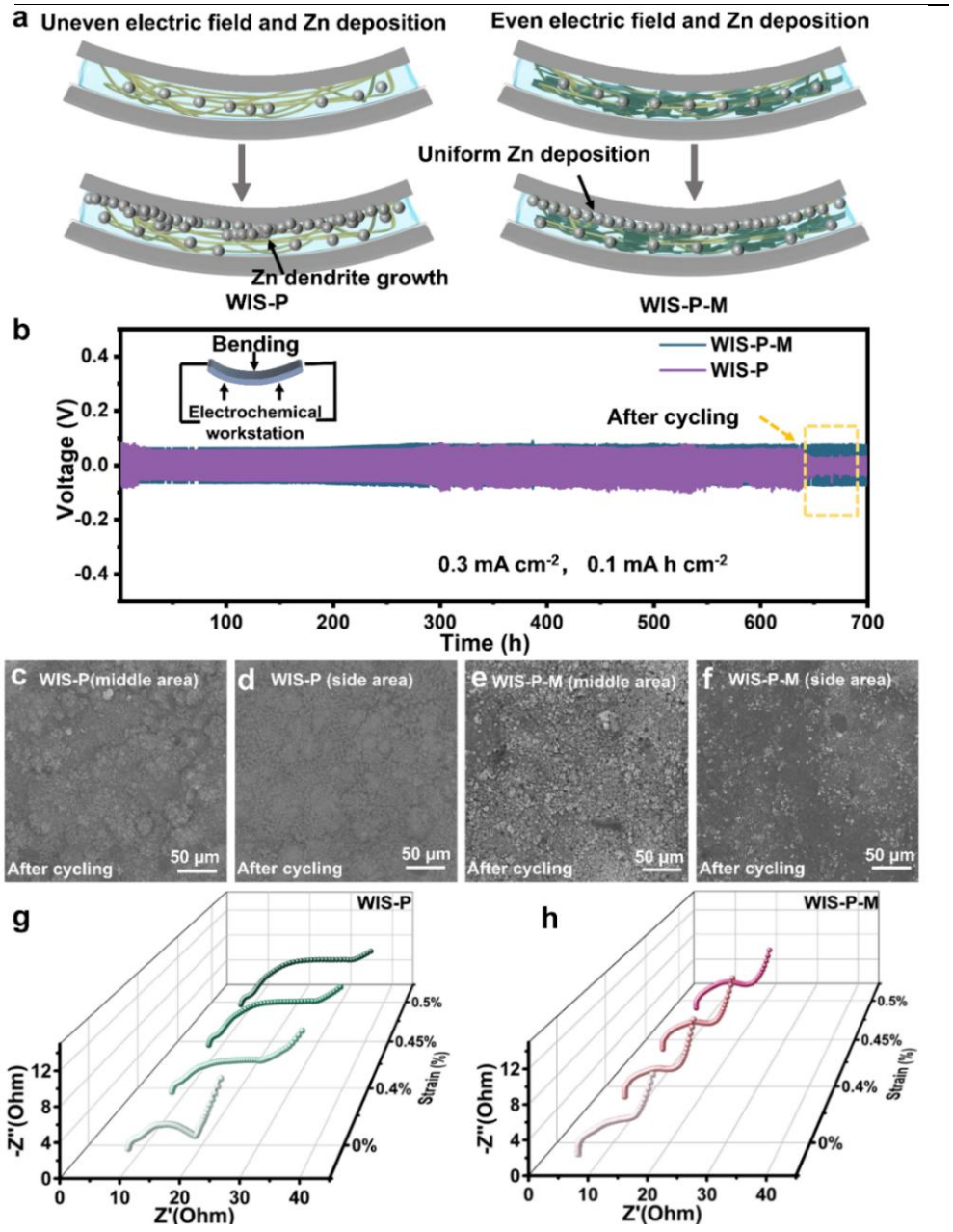


**Figure 6.11** Investigation of the Zn deposition and transport kinetics in WIS-P-M and WIS-P Zn|Zn symmetric device and CSSs. (a) Schematic illustration of the effect of electric field distribution on Zn deposition. (b) Voltage profile of WIS-P and WIS-P-

M Zn|Zn symmetric device. SEM images of cycled Zn in (c) middle area and (d) side area of WIS-P Zn|Zn symmetric device, and (e) middle area and (f) side area of WIS-P-M Zn|Zn symmetric device. EIS measurement for (g) WIS-P CSS and (h) WIS-P-M CSS under different strains.

To further investigate ion transport kinetics, in situ electrochemical impedance spectroscopy (EIS) measurements were conducted under varying bending stresses (Fig. 6.11g-h). The labels WIS-P-0% (WIS-P-M-0%), WIS-P-0.4% (WIS-P-M-0.4%), WIS-P-0.45% (WIS-P-M-0.45%), and WIS-P-0.5% (WIS-P-M-0.5%) represent CSSs under different strain levels of 0%, 0.4%, 0.45%, and 0.5%, respectively. The resulting EIS spectra were analyzed using the equivalent circuit model depicted in Fig. 6.10 and Table 6.2. High-frequency components, namely series resistance ($R_S$) and faradic charge-transfer resistance ($R_{ct}$), indicate charge transfer efficiency, while the low-frequency Warburg impedance ($Z_w$) represents diffusion resistance, collectively reflecting ion transport kinetics. As the strain increased from 0% to 0.5%, the WIS-P CSS exhibited a constant $R_S$ of 7.4 Ω. However, $R_{ct}$ and $Z_w$ increased substantially from 13.0 Ω and 5.8 Ω to 33.1 Ω and 59.8 Ω, respectively, indicating notable changes in ion transport and diffusion. In contrast, the WIS-P-M CSS displayed relatively stable $R_S$ (3.7 Ω), $R_{ct}$ (12.3 Ω), and $Z_w$ (5.3 Ω) at a strain of 0.5%, with only slight increases to 3.8 Ω, 16.9 Ω, and 16.6 Ω, respectively. These values remained consistently lower than those of the WIS-P CSS, highlighting the superior stability of the WIS-P-M CSS. These experimental findings align with the simulation results, suggesting that MXene incorporation promotes electric field homogenization, stabilizing faradic charge-transfer processes and ion diffusion. Additionally, the observed enhancement in ionic conductivity, achieved through MXene-mediated

optimization of the conductive medium, further emphasizes its critical role in improving the system's overall electrochemical performance.

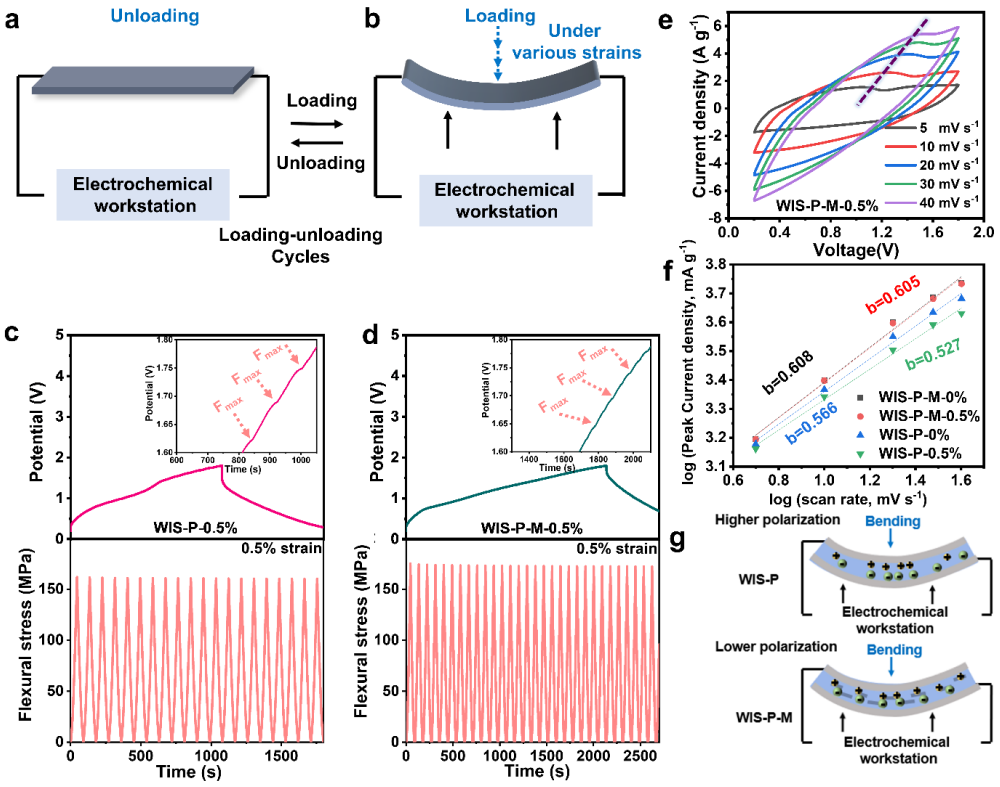


**Figure 6.12** Study of the effect of external deformation on electrochemical performance. Schematic of the in situ mechano-electrochemical test (a) before and (b) after loading. GCD curves showing successive bending cycles for (c) WIS-P CSS and (d) WIS-P-M CSS up to a strain level of 0.5% during the in situ mechano-electrochemical test and the amplified curve insets showing the fluctuations under an external force. (e) CV curves at different scan rates at a constant strain of 0.5% for the WIS-P CSS. (f) *log i* vs. *log v* plots for WIS-P-M and WIS-P CSSs at constant strains of 0% and 0.5%. (g) Schematic illustration of the polarization of WIS-P and WIS-P-

M CSSs during the in situ mechanical-electrochemical test.

An in situ mechano-electrochemical test was performed to investigate the influence of external mechanical stresses on the electrochemical performance of structural energy storage devices. The schematic of the experimental setup before and after mechanical loading is illustrated in Fig. 6.12a-b, respectively. To establish a performance baseline, Fig. 6.13a (WIS-P CSS) and Fig. 6.13b (WIS-P-M CSS) show stable and smooth galvanostatic charge-discharge (GCD) curves under load-free conditions, indicating uniform electric field distribution within the devices. Various strain levels were subsequently applied to examine the devices' response to mechanical stimuli, and the resulting charge-discharge curves were analyzed. For the WIS-P CSS, flexural stress increased from 128 MPa to 161 MPa as the applied strain rose from 0.4% to 0.5% (Fig. 6.12c, Fig. 6.14a-b). Subtle perturbations emerged in the GCD curves, exhibiting progressively amplified as the strain level increased. These cyclic perturbations correlate with the bending load cycles, appearing as concave curves under compressive force, which were shown during the test. In contrast, the WIS-P-M CSS device exhibited greater electrochemical stability under mechanical strain. Its GCD curves remained largely unaffected at a strain of 0.4% (Fig. 6.15a) and showed only minor deviations at a strain of 0.45% (Fig. 6.15b). Even at a strain of 0.5%, the amplitude of perturbations on the GCD curves of WIS-P-M CSS was significantly smaller than those observed in WIS-P CSS (Fig. 6.12d). These findings strongly suggest that the WIS-P-M CSS demonstrates superior electrochemical stability under external mechanical stresses. This can be attributed to the ability of MXene-based electrolyte to mitigate external stress-induced perturbations on the electrochemical performance of the WIS-P-M CSS.

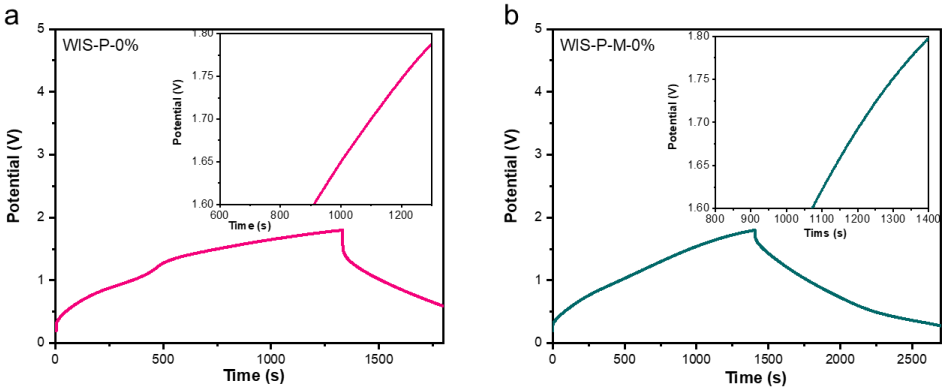


**Figure 6.13** GCD curve of (a) WIS-P-0% and (b) WIS-P-M-0% during in situ mechano-electrochemical measurement and the amplified curves insets showing the fluctuations under an external force.

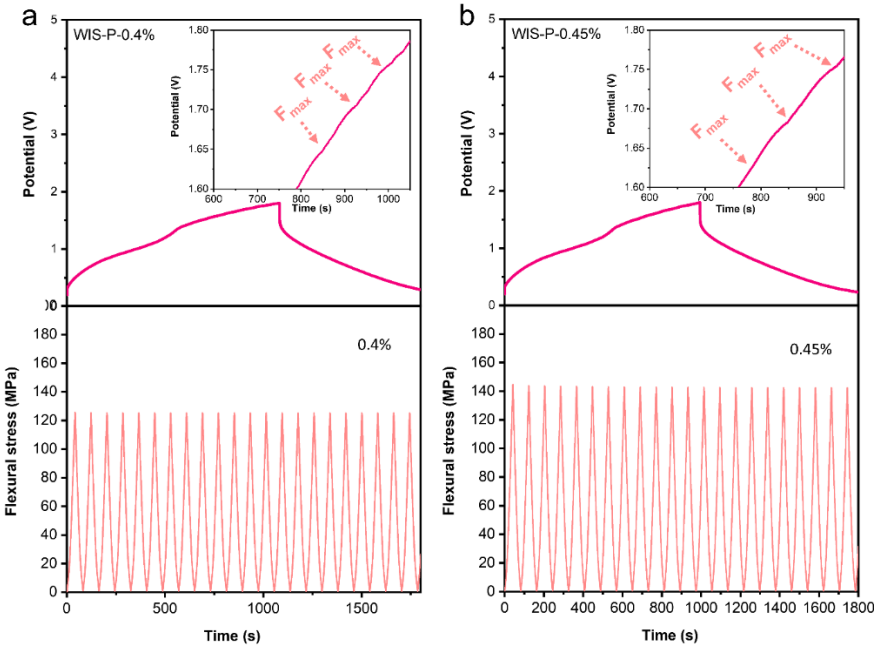


**Figure 6.14** In situ mechano-electrochemical measurements of WIS-P devices. GCD curves of (a) WIS-P-0.4% and (b) WIS-P-0.45% under cyclic bending tests and the amplified curves insets showing the fluctuations under an external force.

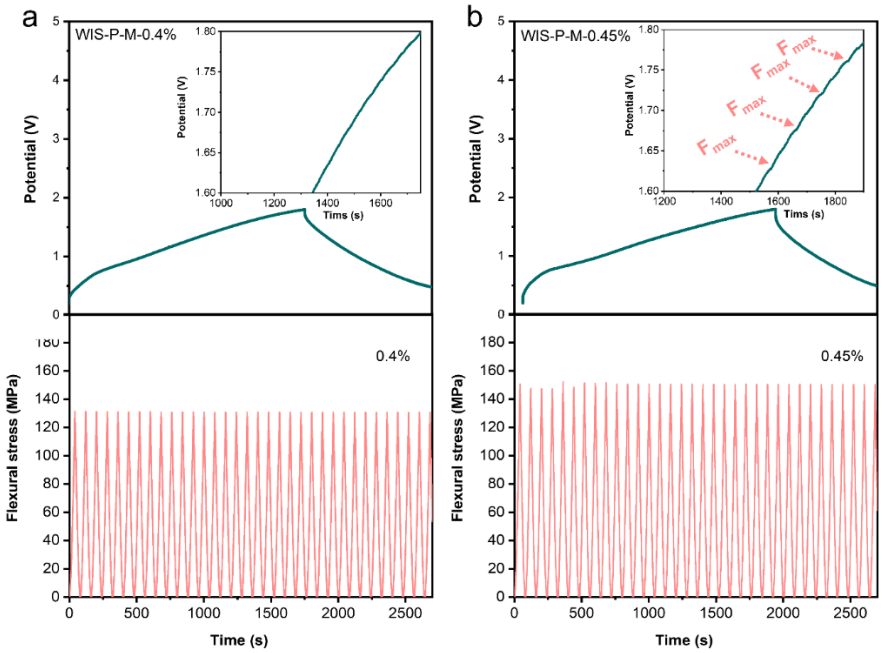


**Figure 6.15** In situ mechano-electrochemical measurements of WIS-P-M devices. GCD curves of (a) WIS-P-M-0.4% and (b) WIS-P-M-0.45% under cyclic bending tests and the amplified curves insets showing the fluctuations under an external force.

Cyclic voltammetry (CV) tests were performed at various scan rates under different applied strains to further elucidate electrochemical behavior under mechanical stress. The CV curves of both WIS-P-M and WIS-P CSSs consistently maintained their characteristic peak shapes and positions across various scan rates and strains, indicating excellent reaction kinetics (Fig. 6.12e and Fig. 6.16-6.19). This stability under mechanical deformation suggests that electrochemical functionality is well-preserved in both devices. The reaction processes of the two devices at strains of 0% and 0.5% were observed in Fig. 6.12f. According to the equation $i = av^b$, ($i$ and $v$ are the current and scan rate, respectively, and $a$ and $b$ are constants), the electrochemical reaction mechanism is classified as diffusion-controlled when $b$ is 0.5 and capacitive-controlled when $b$ is 1 [177]. The $b$ values of WIS-P-0%, WIS-P-0.5%, WIS-P-M-0%

and WIS-P-M-0.5% are 0.566, 0.527, 0.608 and 0.605 respectively, indicating the combination of diffusion-controlled and capacitive-controlled. As the strain increased from 0% to 0.5%, the *b* value for WIS-P CSS showed an obvious decrease. However, it remained unchanged for WIS-P-M, indicating a stabilized reaction process under external load. Incorporating MXene into the electrolyte significantly enhances the CV response to faster potential scans, thereby improving reaction kinetics and rate capability. This improvement can be attributed to the superior ion transport properties and uniform electric field provided with reduced polarization (Fig. 6.12g) by the MXene additive, as indicated by the EIS measurements and simulation results.

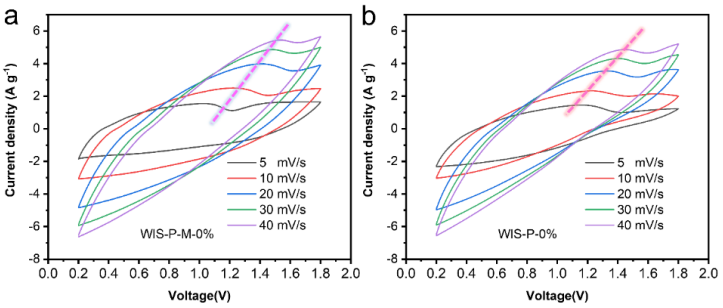


**Figure 6.16** CV curves scanned at the rate of 5-40 mV/s of (a) WIS-P-M-0% and (b) WIS-P-0%. The red dotted lines represent the line connecting the peak current at different rates.

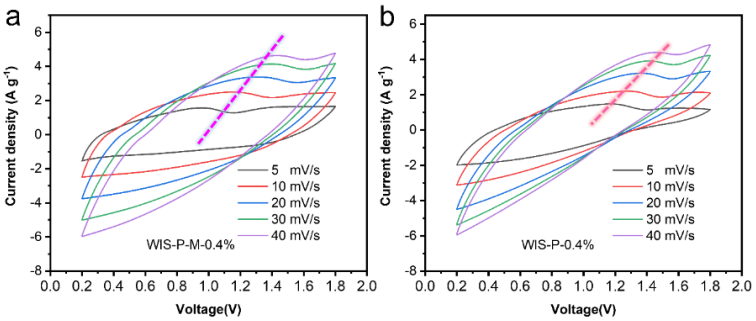


**Figure 6.17** CV curves scanned at the rate of 5-40 mV/s of (a) WIS-P-M-0.4% and (b)

WIS-P-0.4%.

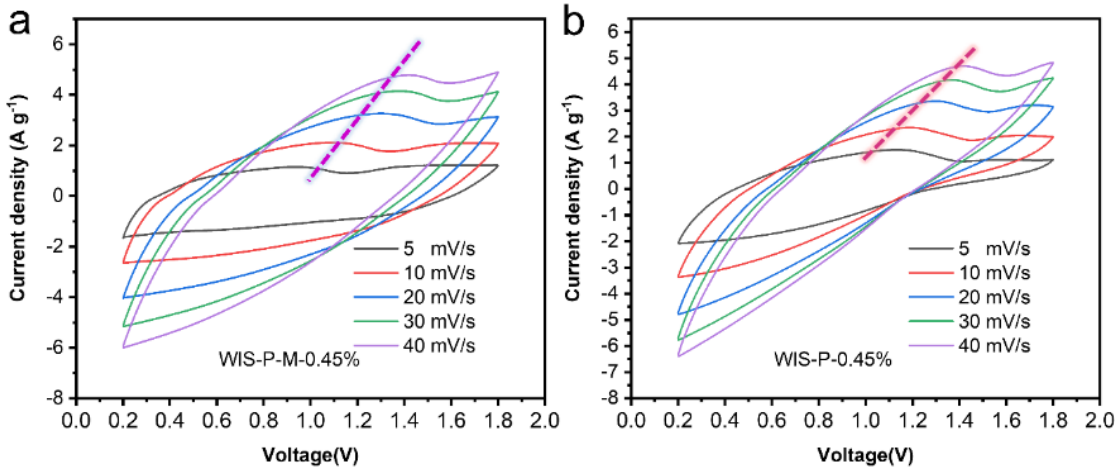


**Figure 6.18** CV curves scanned at the rate of 5-40 mV/s of (a) WIS-P-M-0.45% and (b) WIS-P-0.45%.

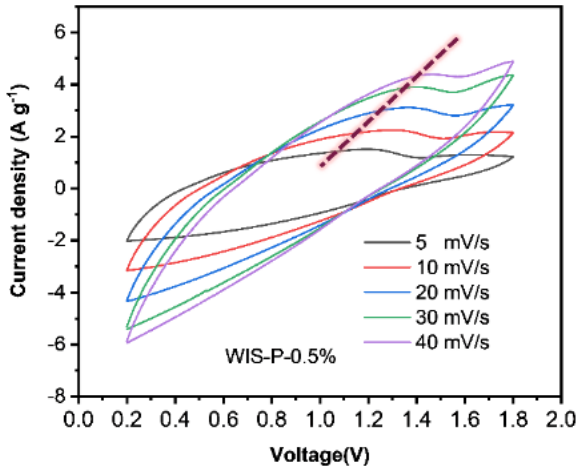


**Figure 6.19** CV curves scanned at the rate of 5-40 mV/s of WIS-P-0.5%.

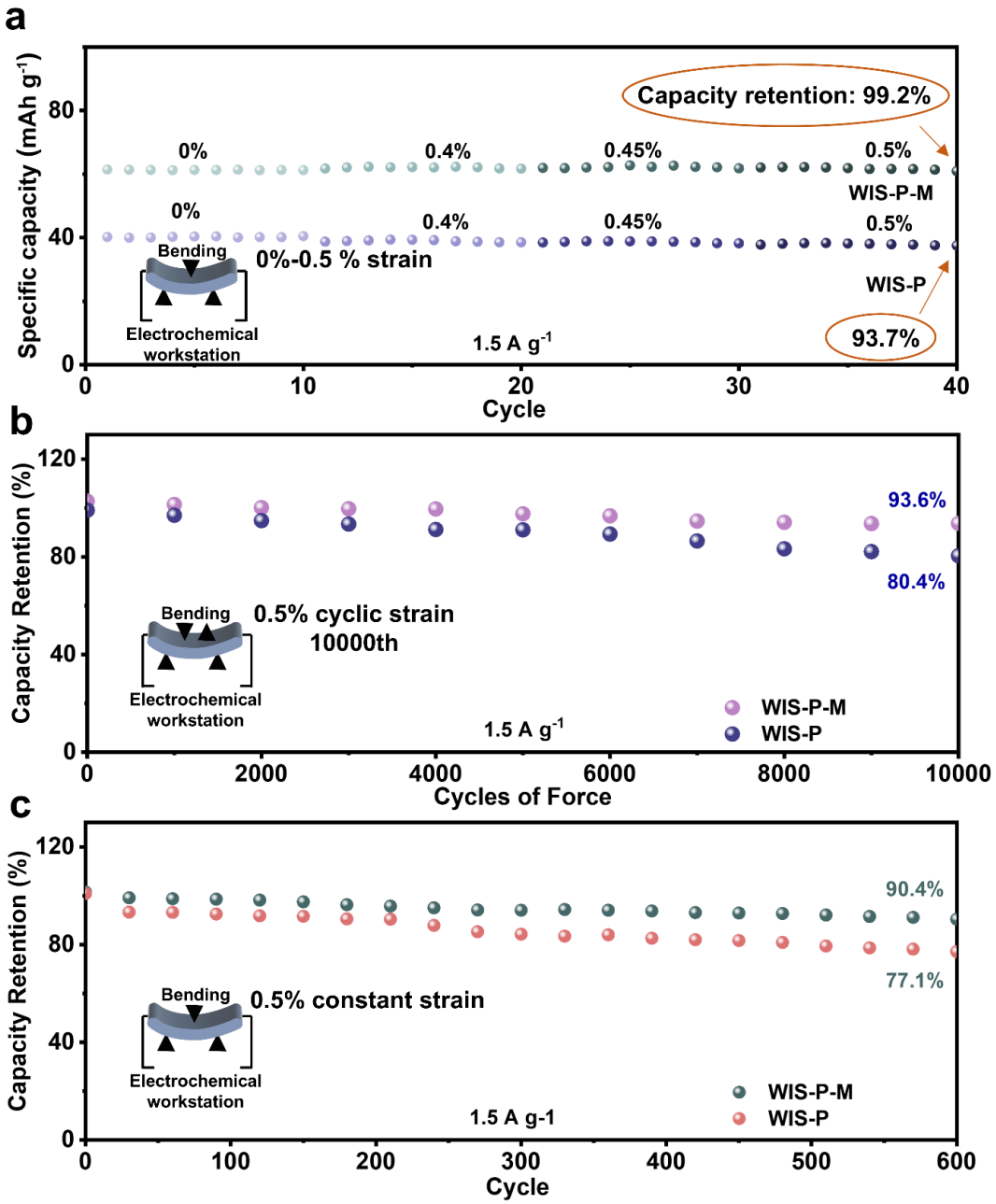


**Figure 6.20** Cyclic performance of WIS-P and WIS-P-M CSSs under a three-point bending test. (a) Cyclic performance of the WIS-P-M and WIS-P CSSs at different constant strains. (b) Capacity retention of the WIS-P-M and WIS-P CSSs under cyclic bending test with a maximum strain level of 0.5%. (c) Capacity retention of the WIS-P-M and WIS-P CSSs under static bending test at a strain level of 0.5%.

The electrochemical performance and mechanical durability of WIS-P-M and WIS-P CSSs were systematically investigated under various applied strains (0%, 0.4%, 0.45%, 0.5%) (Fig. 6.20a). The WIS-P-M CSS exhibited better capacity retention, maintaining stability even at a strain of 0.5% (99.2%), whereas the WIS-P CSS showed a progressive decline in capacity across the strain spectrum. At a strain of 0.5%, the WIS-P CSS delivered a capacity retention of 93.75%. Cyclic bending tests were conducted to evaluate the long-term durability. After 10,000 bending cycles, the WIS-P-M CSS retained 93.6% of its initial capacity, significantly outperforming the WIS-P CSS, which retained only 80.4% (Fig. 6.20b). Moreover, under a static bending test at a strain of 0.5%, the WIS-P-M demonstrated improved capacity retention (90.4%) compared to the WIS-P CSS (77.1%), as revealed in Fig. 6.20c. The enhanced electrochemical stability under mechanical stress is attributed to the more uniform electric field distribution within the WIS-P-M CSS.

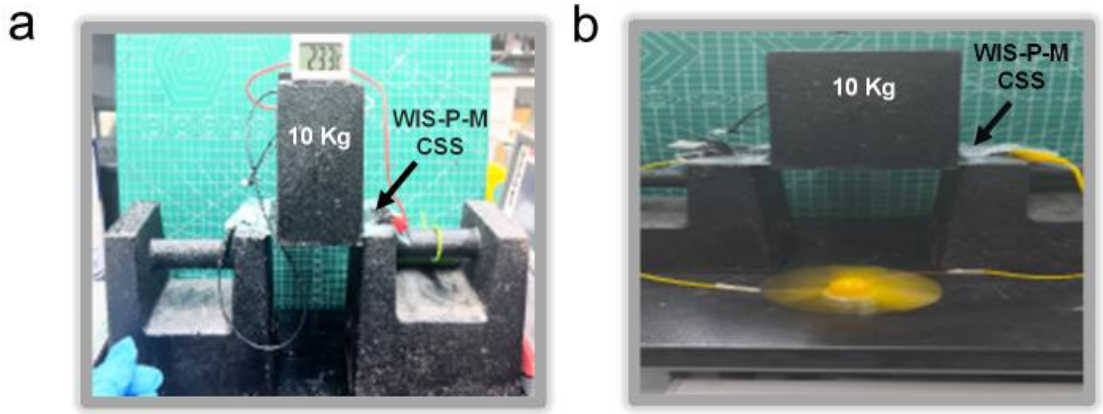


**Figure 6.21** The practical application of the WIS-P-M CSS that is (a) powering an electric thermometer and (b) driving a small fan.

Electrochemical performance tests under realistic load conditions were conducted to assess the practical viability of the devices. The WIS-P-M CSS was able to power an

electronic thermometer while subjected to a 10 kg load (Fig. 6.21a). Moreover, the device successfully powered a small fan under a substantial mechanical load (Fig. 6.21b). These observations confirm the mechanical robustness and electrochemical reliability of the WIS-P-M CSS, which are critical for real-world applications that require stable performance under mechanical stresses. The potential applications of the WIS-P-M CSS span multiple technological fields, including autonomous aerial vehicles, automotive systems, and aerospace engineering. Notably, the device's versatility extends to applications requiring custom-shaped fabrication and controlled deformation. This versatility underscores the significant potential of WIS-P-M CSS in advancing structural energy storage technologies. Future research directions may focus on optimizing the device's performance under diverse environmental stressors and exploring its integration into complex, shape-adaptive structures.

## 6.5 Summary

In conclusion, the MXene-based CSS demonstrates a high energy density of 80 Wh $kg^{-1}$ and a flexural modulus of 33.80 GPa. Furthermore, the MXene-based CSS maintains stable electrochemical behavior under load-induced deformation, which is attributed to the uniform electric field modulated by MXene. Specifically, the dipoles formed through hydrogen bonding between MXene and polymer chains accumulate, generating a polarized electric field that balances the overall electric field distribution. In situ mechano-electrochemical assessments and simulation results confirm that MXene-based CSS sustains a more consistent electric field and higher capacity retention under a strain of 0.5% compared to CSS without MXene. Notably, the device retains 90.4% of its initial capacity after 10,000 mechanical load cycles, indicating excellent long-term stability. The practical application of the prepared MXene-based

CSS underscores their superior performance and ability to maintain electrochemical properties by mitigating the effects of external mechanical forces. Additionally, the versatility of such devices may expand the use of CSSs in custom-shaped fabrication and scenarios requiring controlled deformation.

# Chapter 7 Stiff and Tough Anti-freezing Electrolyte

Applying Zn-ion based multifunctional composite structural hybrid supercapacitors (CSSs) at subzero temperature introduces significant constraints, primarily containing polymer electrolyte crystallization and structural deterioration under mechanical loading. The structural polymer electrolyte requires high ion conductivity and mechanical robustness, wherein stiffness and toughness are essential for transferring mechanical load between interlayers and preventing crack propagation. An unconventional Hofmeister effect of chaotropic $ClO_4^-$ anions was observed in anti-freezing ethylene glycol (EG)-polymer, leading to simultaneous enhancements in the stiffness and toughness of the polymer composite. The formation of strong and long hydrogen bonding (SHB) among $ClO_4^-$, EG, and the polymer matrix makes the material stiff and tough. Benefiting from the superior freeze resistance and mechanical strength, the fabricated CSS demonstrates exceptional electrochemical stability, maintaining 90.9% of its initial specific capacity (61.06 mAh $g^{-1}$) through 2000 cycles at 0.3 A $g^{-1}$ even under cyclic three-point bending test (at a strain of 0.6%) at subzero temperatures. Furthermore, this investigation enhances the understanding of CSS operation under both mechanical impact and subzero conditions, establishing design principles for CSS applications.

## 7.1 Introduction

The increasing demand for high energy density storage systems has driven the development of lightweight designs to extend the operational range of electric devices.

Multifunctional CSESDs offer an effective strategy to reduce system weight by integrating electrochemical and mechanical functionalities within a unified structure [178, 179]. This design enables the CSESD, which concurrently stores electrochemical energy and withstands mechanical stress, to serve as a viable alternative to traditional structural components in automotive frames and aircraft structures [11, 180]. In this way, the potential applications in volume- and weight-restricted fields, specifically in electric vehicles and aerospace systems are significantly expanded [181].

Integrating energy storage components, such as multifunctional electrodes, separators, and electrolytes, into CSESDs represents a rational strategy for achieving robust mechanical strength without compromising electrochemical performance [30, 36]. As energy storage units, zinc-ion batteries or hybrid supercapacitors have emerged as safer alternatives to lithium-ion or sodium-ion batteries, to overcome their inherent risks of thermal runaway due to structural failure under mechanical stress [30]. Zinc-ion hybrid supercapacitors (ZIHSCs) demonstrate superior power density, ion diffusion, and cycling stability relative to zinc-ion batteries, thereby facilitating their integration into structural systems and reducing the need for frequent replacement [36, 182]. For practical applications of CSESDs including zinc-ion based hybrid composite structural supercapacitors (CSSs), there is limited research on how to maintain excellent electrochemical stability under mechanical load and at low temperature. To achieve this requirement, the structural polymer electrolyte within CSSs should simultaneously exhibit superior ionic conductivity and mechanical strength at low temperatures.

The deterioration of electrochemical performance at subzero temperatures is primarily caused by the freezing of the electrolyte, resulting from the formation of hydrogen

bonds (HBs) between water molecules [183]. As a non-toxic, economically viable strategy for frost resistance, the introduction of low molecular vicinal alcohols, such as glycerol and ethylene glycol (EG), effectively disrupts the HB of water molecules [184]. However, attributed to their minimal molecular mass and deficiency of double bonds, the synthesis of EG molecules within polymer remains intricate and technically challenging. Copolymerization of monomers in an EG-water binary system is a reliable technique for fabricating polymer electrolytes. However, the mechanical properties inevitably deteriorate due to the HB interactions between residual EG and polymer chains, which disrupt the physically cross-linked polymer networks. Furthermore, the formation of EG-polymer HB is also susceptible to dissociation under deformation. To address the mechanical weakness, Mo *et al.* developed an EG-based anionic polyurethane acrylate (EG-waPUA) with robust extended chains, which are chemically anchored on the polymer chains, displaying notable mechanical flexibility and durability under cryogenic temperatures [102]. Nonetheless, the fabrication process requires precise control and rigorous conditions.

Recent studies have explored the Hofmeister effect to modulate polymer mechanical strength, specifically utilizing the "salting out" phenomenon induced by kosmotropes and the "salting in" effect caused by chaotropes. Conventionally, the chaotropic anions augment elastic strain while reducing stiffness through promoting water-polymer HB replacing polymer-polymer interactions [103, 185]. Conversely, kosmotropic anions exhibit opposite effects on these mechanical properties [103, 185]. It is challenging to simultaneously fulfill the dual mechanical requirements of stiffness and toughness for CSS electrolytes operating at low temperatures, where the high stiffness enables the electrolyte to effectively transfer mechanical load between layers, while the high

toughness prevents crack propagation under loading conditions.

A multifunctional freeze-tolerant CSS equipped with a rationally designed composite electrolyte with chaotropic $ClO_4^-$ additives was fabricated to exhibit stable cycling performance under mechanical stress at subzero temperatures. Unlike the conventional Hofmeister effect in which $ClO_4^-$ promotes elastic strain while compromising stiffness [103], the synergistic effect of $ClO_4^-$ and EG additives in our designed electrolyte results in increases of both elastic strain and stiffness, leading to enhanced toughness, compared to EG-based electrolytes in the absence of $ClO_4^-$. Density functional theory (DFT) calculations showed that the strong and long hydrogen-bonding (SHB) in polymer electrolyte containing $ClO_4^-$ possesses a higher bond-breaking energy (0.5 eV) than that of the weak hydrogen bonds in the $ClO_4^-$-free polymer (0.37 eV). Subsequently, this enhanced and lengthened hydrogen-bonding network enables superior mechanical stiffness and toughness. Under sub-zero temperatures, the CSS delivers a significant specific energy of 54.4 Wh $kg^{-1}$ and a flexural modulus of 29.28 GPa. More remarkably, the CSS maintains exceptional cycling stability with 90.9% capacity retention after 2000 cycles, substantially outperforming the $ClO_4^-$-free system (72.8% retention after 938 cycles) under cyclic three-point bending (at a strain of 0.6%) at -20 ℃. For practical applications, the CSS is still well-functioned when embedded in solid ice and subjected to impact and suspension conditions. This work comprehensively addresses the crucial balance between mechanical integrity and electrochemical performance in sub-zero environments, extending the potential application for structural energy storage.

## 7.2 Structural characteristics and performance of SE-PAM and CE-PAM

The polyacrylamide (PAM)-based polymer electrolytes were synthesized by adding AM monomer, APS initiator, and MBA crosslinker into different salts of ($ZnSO_4$ and $Zn(ClO_4)_2$) in EG-water binary or water solution, followed by thermal polymerization rather than utilizing the conventional soaking method. The electrolyte systems comprising $ZnSO_4$ and $Zn(ClO_4)_2$ in an EG-water binary mixture and $ZnSO_4$ in a water system are denoted as SE-PAM, CE-PAM, and SH-PAM, respectively. The introduction of chaotropic $ClO_4^-$ anions [103, 185] into electrolytes significantly modifies mechanical performance by modulating the molecular interactions. Digital images in Fig. 7.1 show that SH-PAM electrolyte exhibits significant shrinkage after 48h, whereas the SE-PAM and CE-PAM electrolytes maintain their volume with minimal changes. This stability is attributed to the hydrogen bonds formed between EG and water, which effectively retain moisture and preserve high ion conductivity.

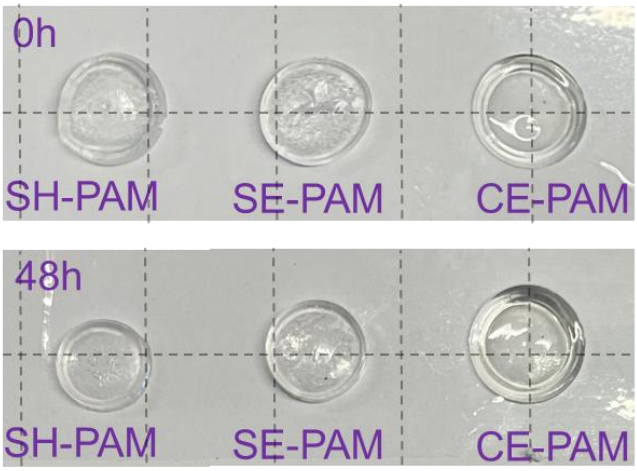


**Figure 7.1** Digital images of SH-PAM, SE-PAM, and CE-PAM electrolytes before and after 48h exposure to air at 20 ℃.

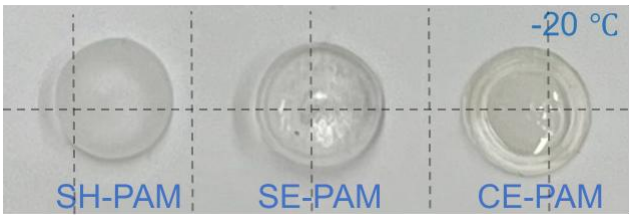


**Figure 7.2** Digital images of SH-PAM, SE-PAM, and CE-PAM electrolytes after cooling at -20 ℃ for 24 h.

The anti-freezing properties of SH-PAM, SE-PAM, and CE-PAM electrolytes are illustrated in Fig. 7.2. The SH-PAM without EG freezes into a solid at -20 ℃, whereas SE-PAM and CE-PAM do not freeze at -20 ℃. In consequence, the incorporation of EG into the electrolyte improved the anti-freezing property of the electrolyte due to the formation of hydrogen bonds between EG and water.

SH-PAM, SE-PAM, and CE-PAM electrolytes exhibit retarded kinetics for oxygen evolution reactions (OER) (Fig. 7.3a). At 20 ℃, the ionic conductivity of CE-PAM electrolytes reached 13.5 mS $cm^{-1}$ and maintained a high value (5.8 mS $cm^{-1}$) at -20 ℃ (Fig. 7.3b-c). The reduced ionic conductivity of CE-PAM electrolyte at -20 ℃ is primarily attributed to the restricted ion mobility at low temperatures. During the ice-melting process, there is a sharp endothermic peak in the DSC curve (Fig. 7.3d). The DSC curve exhibits a distinct endothermic peak at -18 ℃ for the SH-PAM electrolyte, which is significantly higher than those for SE-PAM and CE-PAM. This observation suggests that the introduction of EG molecules reduces the amount of free water by forming hydrogen bonds between EG and water. Therefore, the SE-PAM and CE-PAM demonstrate enhanced freezing resistance to lower temperatures

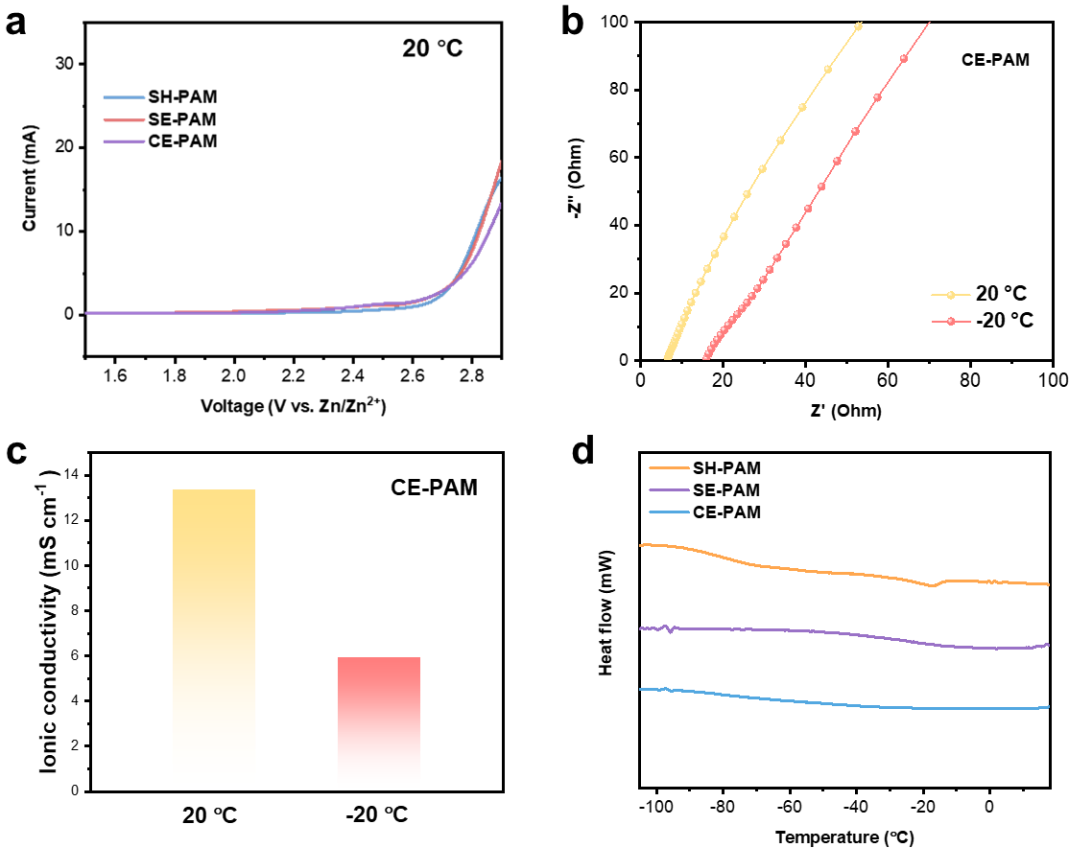


**Figure 7.3** (a) LSV curves of SH-PAM, SE-PAM, and CE-PAM electrolytes. (b) EIS for CE-PAM electrolyte at 20 ℃ and -20 ℃. (c) Ionic conductivity of CE-PAM electrolyte at -20 ℃ and 20 ℃. (d) DSC measurements for SH-PAM, SE-PAM, and CE-PAM electrolytes.

To demonstrate the molecular interactions, density functional theory (DFT) calculations were employed to determine the formation energy and binding energies ($E_b$) between PAM chains and EG with and without $ClO_4^-$ addictive in SE-PAM and CE-PAM electrolytes (Fig. 7.4a).

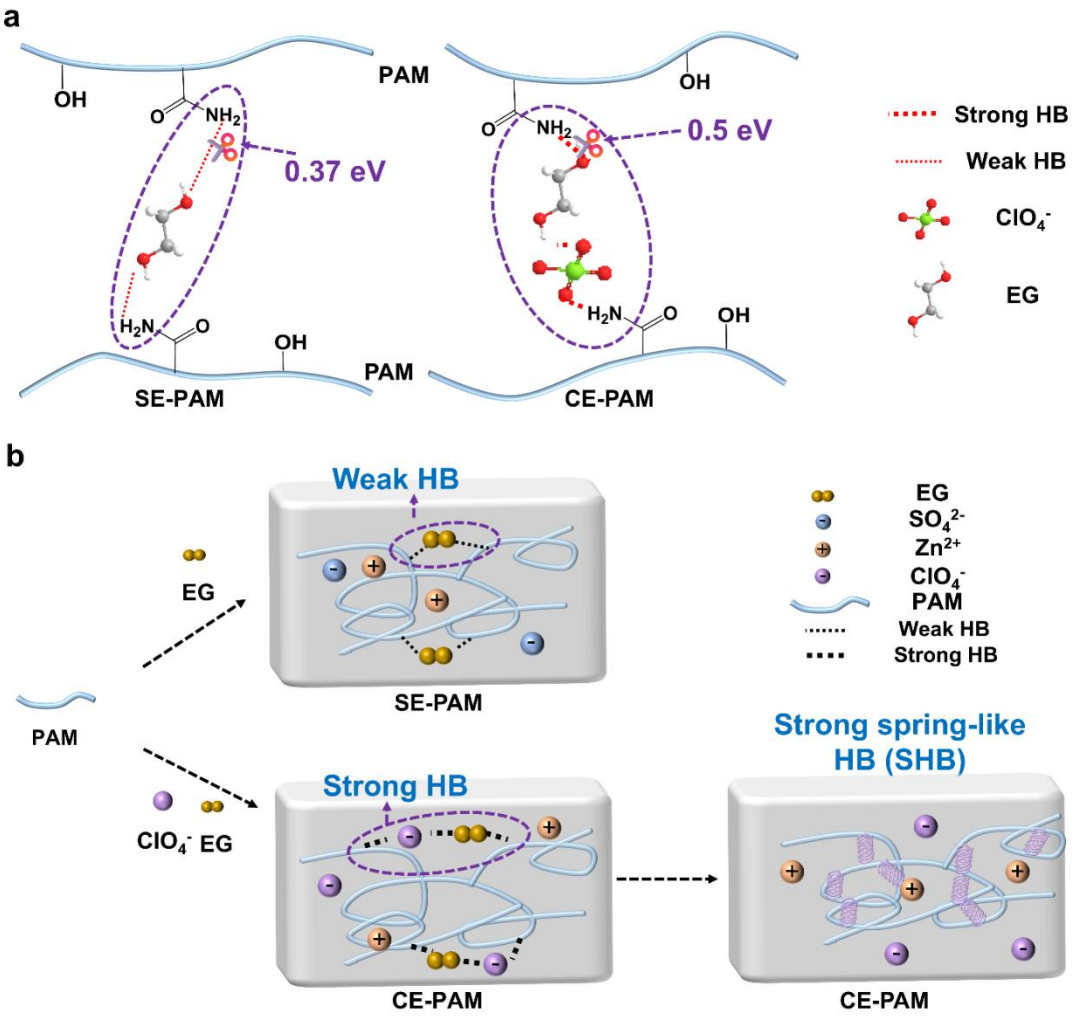


**Figure 7.4** Structural characteristics from DFT results of SE-PAM and CE-PAM electrolyte. (a) DFT results of binding energies ($E_b$) of PAM and EG molecules with and without $ClO_4^-$ additives. (b) Schematic illustration of weak HB interactions between EG and PAM chains in SE-PAM and strong HB among EG, $ClO_4^-$, and PAM chains in CE-PAM.

The computational results elucidate that breaking the HB between PAM and EG is an endothermic reaction for both systems. Notably, the computed $E_b$ for the CE-PAM system is 0.50 eV, which is much higher than that of SE-PAM ($E_b$ = 0.37 eV), indicating that the introduction of $ClO_4^-$ effectively enhances binding affinity between PAM and EG. These results verify the synergistic effect of chaotropic $ClO_4^-$ anions

and EG additives, which strengthens the interaction between polymer chains, in contrast to the traditional Hofmeister effect of $ClO_4^-$ that typically weakens such polymer-polymer interactions. Consequently, as illustrated in Fig. 7.4b, the weak HB between EG molecules and PAM chains exhibits a propensity for breaking during deformation [102]. The robust HBs among $ClO_4^-$, EG, and the polymer chains are capable of maintaining structural stability and elastic deformation under load-bearing, ensuring that the material can absorb and dissipate mechanical energy efficiently without experiencing permanent deformation or failure. This characteristic allows the CE-PAM to exhibit both resilience and strength, making it highly suitable for CSS applications where mechanical stresses are encountered.

The mechanical properties of composite electrolytes were evaluated at subzero temperatures. FTIR spectroscopy (Fig. 7.5a) suggests that the formation of strong HB interactions in polymer electrolyte with $ClO_4^-$ anions, where the N-H stretching bonds shift slightly to lower wavenumbers from 3478 and 3378 $cm^{-1}$ to 3468 and 3371 $cm^{-1}$ [176]. This shift can also be ascribed to the synergistic effect of $ClO_4^-$ and EG, which promotes the formation of strong hydrogen bonding among $ClO_4^-$, EG, and polymer chains. The elastic modulus and breaking energy are indicators for stiffness and toughness, respectively, which contribute to preventing deformation and crack-induced deterioration under loading. Fig 7.5b shows the tensile stress-strain curves of SE-PAM and CE-PAM electrolytes at -20 °C. The CE-PAM and SE-PAM indicate no substantial breaking at small elongation and elastic deformation. The CE-PAM polymer does not rupture until it reaches 888% elongation, with a tensile strength of 60.94 kPa, three times greater than that of SE-PAM with a comparatively low failure tensile strain of 531%. Correspondingly, both the elastic modulus and mechanical

toughness of polymer electrolytes considerably improved with the $ClO_4^-$ additive.

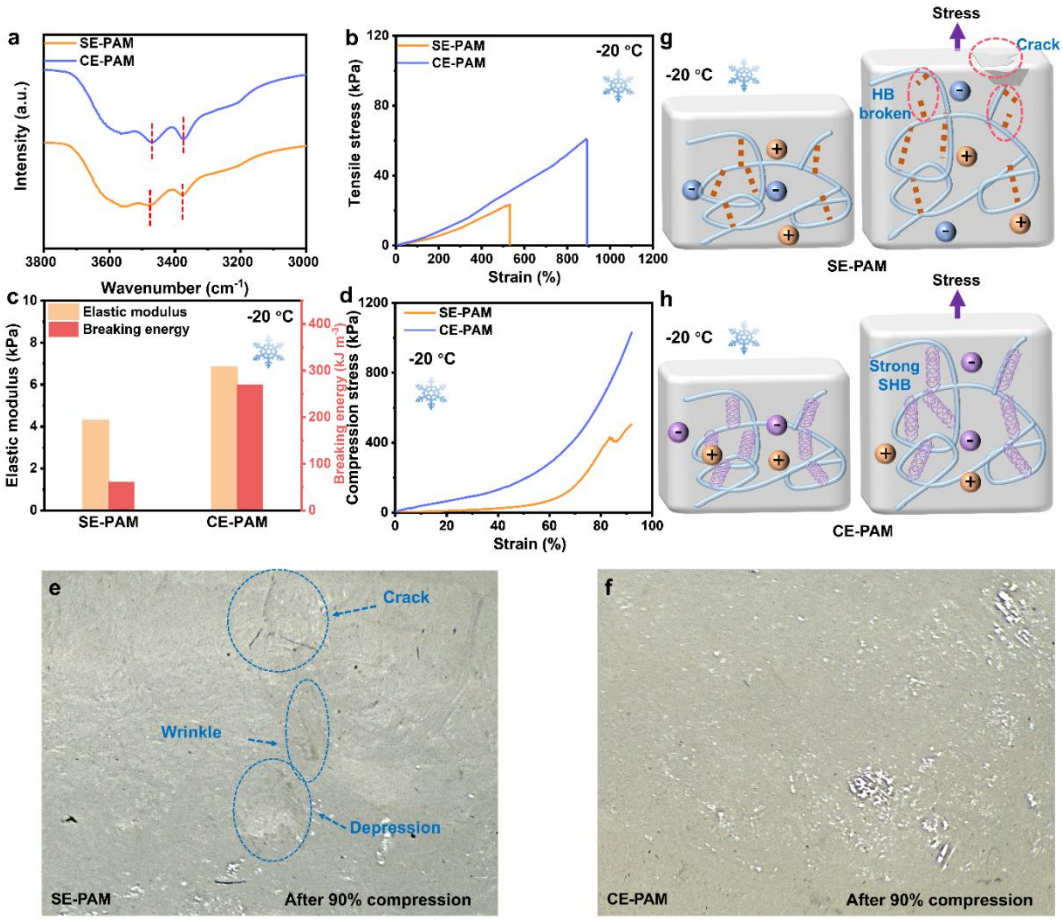


**Figure 7.5** Mechanical properties of SE-PAM and CE-PAM polymer electrolytes at low temperature. (a) FTIR spectra of SE-PAM and CE-PAM electrolytes. (b) Tensile stress-strain curves of SE-PAM and CE-PAM electrolytes at -20 ℃. (c) The corresponding elastic modulus and breaking energy. (d) Compressive stress-strain curves of SE-PAM and CE-PAM polymer at -20 ℃. (e-f) The optical images showing the surface morphologies of the SE-PAM and CE-PAM after compression. Illustration of the HB structures of the (g) SE-PAM and (h) CE-PAM electrolytes before and after elongation.

In Fig. 7.5c, the elastic modulus (Young's modulus) and breaking energy of SE-PAM

and CE-PAM at -20 ℃ were summarized. CE-PAM polymer demonstrates a much higher elastic modulus (6.8 kPa) and breaking energy (270 kJ $m^{-3}$) than those of SE-PAM, with an elastic modulus of 4.3 kPa and breaking energy of 61 kJ $m^{-3}$, indicating strong SHB formation among $ClO_4^-$, EG, and the polymer chains due to the synergistic effect of $ClO_4^-$ and EG molecules.

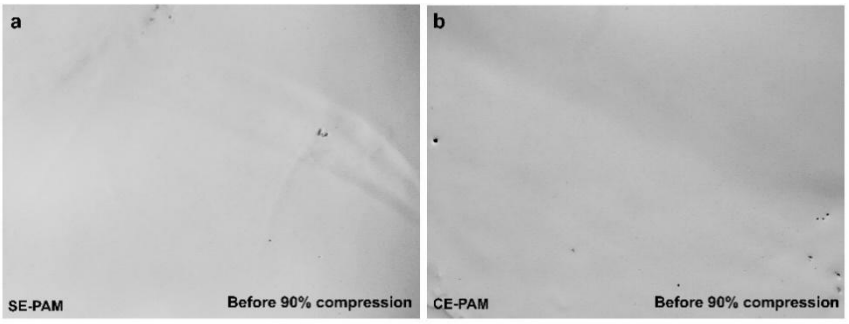


**Figure 7.6** The optical images showing the surface morphologies of the (a) SE-PAM and (b) CE-PAM before 90% compression.

The compression properties of electrolytes were further investigated under deformation of over 90% at -20 ℃. As displayed in Fig. 7.5d, the compressive stress-strain curve of SE-PAM fractured at a compressive strain of approximately 80% with low compressive stress because of the weak HB within the polymer matrix. However, the compressive stress of CE-PAM increased significantly, accompanied by a smooth compressive curve, displaying superior rigidity. The surface morphologies of the electrolytes before and after the compression tests are shown in Fig. 7.6 and Fig. 7.5e-f. Obviously, after compressing at a high strain of over 90%, the SE-PAM exhibited poor mechanical properties with the propagation and multiplication of cracks, wrinkles, and localized depressions on the surface, in contrast to the original smooth and flat morphology, which corresponded to the sharp decrease in the compressive curve. By

contrast, the CE-PAM sustained its original morphology after compression with the absence of any evident fracture, indicating enhanced mechanical performance. The improved mechanical strength is owing to the strong SHB that can maintain stability without significant damage under tensile load (Fig. 7.5g-h). The weak HB between EG and polymer chains fails to dissipate mechanical energy, causing energy accumulation and crack propagation. However, the SHB interactions of $ClO_4^-$, EG, and polymer efficiently dissipate mechanical load and absorb energy, demonstrating an unconventional Hofmeister effect of $ClO_4^-$. This unique HB maintains rigidity and network conformation while undergoing deformation, preventing the failure development. These results further demonstrate the synergistic effect of $ClO_4^-$ and EG, enhancing the hydrogen interaction with the polymer chains, compared to the $ClO_4^-$-free EG-polymer. Due to the robust and long HB absorbing and dissipating mechanical energy with significant elastic deformation, the developed CE-PAM electrolyte presents high elastic modulus and breaking energy, overcoming the trade-off between stiffness and toughness observed in conventional Hofmeister effect and enabling low-temperature CSS applications.

## 7.3 Electrochemical and mechanical characterization of CSSs

The electrochemical performance of CSSs with various electrolytes was evaluated. The fabrication of SH-PAM-CSS, SE-PAM-CSS, and CE-PAM-CSS was conducted by a wet lay-up method, enabling curing at ambient temperature under regulated vacuum conditions (Fig. 7.7a). This process involved sequential layering of epoxy-impregnated CFs and glass fibers (GFs), energy storage unit (CFs-AC cathode, composite electrolyte, and Zn foil anode), and epoxy-infused GFs/CFs layers. The integrated carbon fiber composite with an embedded energy storage unit using this

technique demonstrates significant potential for an industrial scale. To evaluate the ionic conductivity of CSS devices under extreme conditions, the electrochemical impedance spectroscopy (EIS) analysis was conducted at 20, 0, and -20 ℃ and the resulting data were fitted by an equivalent circuit (Fig. 7.8). Faradic charge-transfer resistance ($R_{ct}$) at high frequency reflects the efficiency of charge transfer. Over the temperature range of 20 ℃ to -20 ℃, the $R_{ct}$ values for CE-PAM-CSS and SE-PAM-CSS exhibit a moderate increase, rising from 149.8 Ω to 309.4 Ω and from 179.4 Ω to 320.9 Ω, respectively (Fig. 7.7b-c). Due to the anti-freezing properties of the CE-PAM and SE-PAM electrolytes, they exhibit high ionic conductivity even at -20 ℃. In contrast, the $R_{ct}$ for SH-PAM-CSS drastically increases from 85.89 Ω to 4709 Ω, implying that the electrolyte underwent freezing at low temperature (Fig. 7.7d). Therefore, the introduction of EG into the electrolyte promotes the formation of HB between EG and water molecules, thereby enhancing the low-temperature durability of the electrolyte.

The GCD curves at various current densities were analyzed (Fig. 7.9 for 20 ℃ and Fig. 7.7e for -20 ℃). The CE-PAM-CSS exhibits a slight decrease in specific capacity and power density from 80.71 mAh $g^{-1}$ and 64 Wh $kg^{-1}$ at 20 ℃, respectively, to 68.9 mAh $g^{-1}$ and 54.4 Wh $kg^{-1}$ at -20 ℃. The CV profile of CE-PAM-CSS measured at -20 ℃ exhibits a similar shape to that measured at 20 ℃, demonstrating excellent ionic conductivity (Fig. 7.10a). The maintenance of a good rate performance of CE-PAM-CSS at -20 ℃ (Fig. 7.10b) implies the superior ion transport kinetics of CE-PAM electrolyte at sub-zero temperatures. Fig. 7.7f presents the sequential cycling of CE-PAM-CSS at temperatures ranging from 20 ℃ to -20 ℃. When tested at -20 ℃, the CE-PAM-CSS device retains approximately 85% of its original capacity at 20 ℃.

Upon returning to 20 °C, the CE-PAM-CSS exhibits no significant capacity degradation. The corresponding GCD results during the cooling-heating process are shown in Fig. 7.7g.

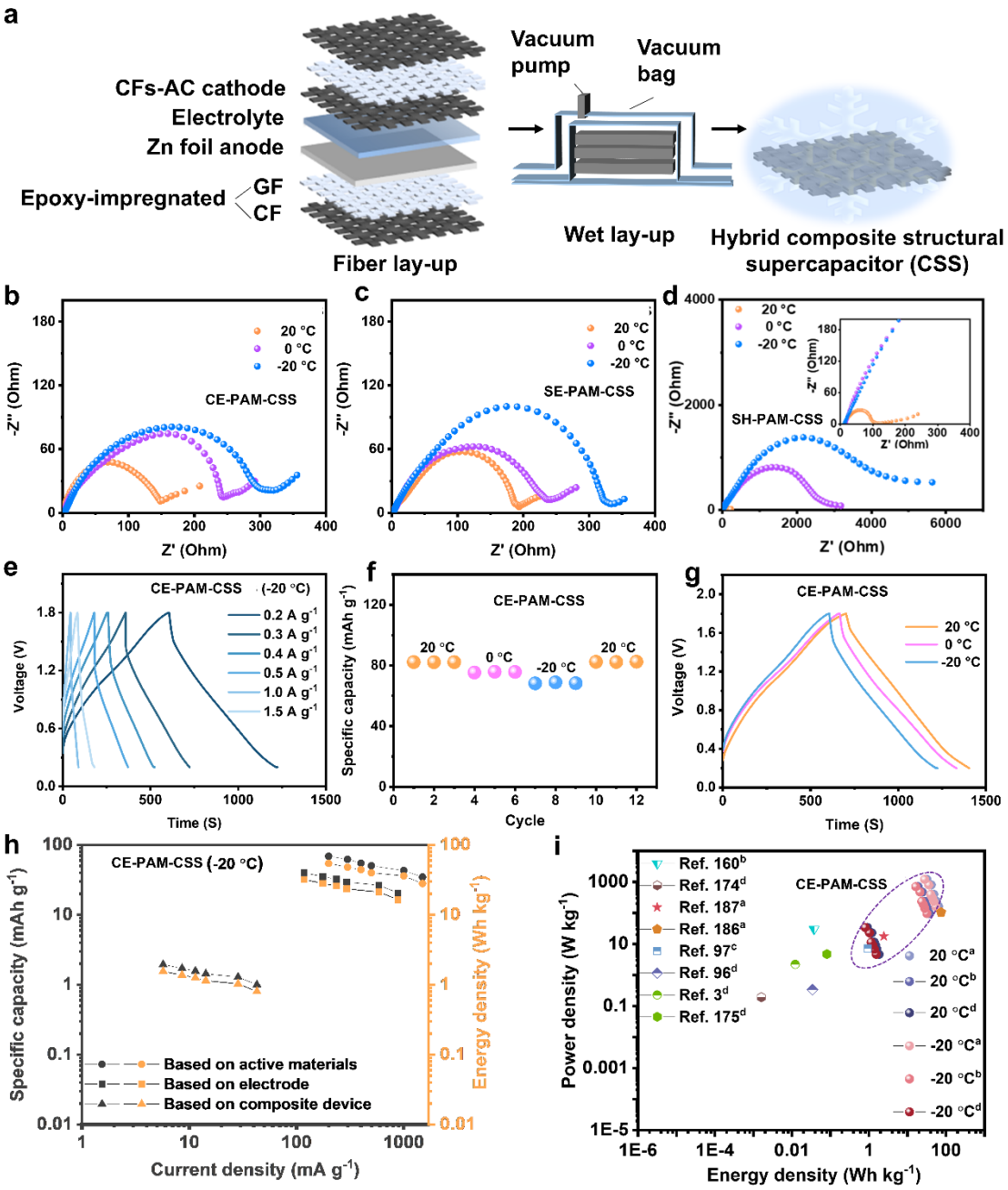


**Figure 7.7** Fabrication and electrochemical characterization of CSSs with various electrolytes. (a) Schematic illustration of the preparation of CSSs. EIS curves for (b) CE-PAM-CSS (c) SE-PAM-CSS (d) SH-PAM-CSS at -20 °C, 0 °C and 20 °C. (e)

Galvanostatic charge-discharge (GCD) curves of CE-PAM-CSS at -20 ℃. (f) Cycling performance of CE-PAM-CSS during the cooling-heating process. (g) The corresponding GCD curves of CE-PAM-CSS during the cooling-heating process. (h) Specific capacity and energy density of CE-PAM-CSS at -20 ℃ at different current densities. (i) Ragone plot of mass specific power and energy densities of CE-PAM-CSS at -20 ℃ and 20 ℃ compared with other reported values (based on [a] active materials; [b] electrode; [c] total energy storage unit mass of electrodes, electrolyte, and separator; [d] composite device)

Moreover, to provide a multifaceted analysis, the specific capacities and energy densities were further calculated by mass, volume, and area based on active materials, electrodes, or composite devices at 20 ℃ and -20 ℃ (Fig. 7.11-7.12 and Fig. 7.7h). Notably, at -20 ℃, the CE-PAM-CSS can deliver a specific capacity of 34.65 mAh $g^{-1}$ even at 1.5 A $g^{-1}$, manifesting exceptional rate performance. When evaluated as an integrated device, the CE-PAM-CSS maintains high values for gravimetric/volumetric/areal specific capacities (1.9 mAh $g^{-1}$/3.8 mAh $cm^{-3}$/1.3 F $cm^{-2}$), energy densities (1.6 Wh $Kg^{-1}$/3.0 Wh $cm^{-3}$/0.5 Wh $cm^{-2}$), and power densities (4.7 W $Kg^{-1}$/7.7 W $cm^{-3}$/1.4 W $cm^{-2}$) at -20 ℃. Ragone plot based on weight, area, and volume [96, 98, 152, 153] (Fig. 7.7i, Table 7.1, and Fig. 7.13a-b) reveals that the CE-PAM-CSS maintains superior energy density at low temperature, surpassing other research work reported in the literature. Its energy density is even comparable to that of structural batteries at room temperature [186].

**Table 7.1** Comparison of energy density and power density of different composite

structural supercapacitors (CSSs).

| CSSs | Energy density ($Wh \cdot kg^{-1}$) | Power density ($W \cdot kg^{-1}$) | Ref. |
|---|---|---|---|
| CNT fiber/Polymer electrolyte interleaves | 0.375[b] | 30[b] | [160] |
| CF-CSS | 0.0016[d] | 0.193[d] | [174] |
| N-doped CF | 1.93[a] | 39.2[a] | [187] |
| CF-structural battery | 75[a] | 105[a] | [186] |
| 5:5 NiCo-LDH-CSS | 0.191[d] | 1.508[d] | [97] |
| LEID-3 | 0.034[d] | 0.34[d] | [96] |
| CF/$MnO_2$ | 0.0122[d] | 2.21[d] | [3] |
| MnOOH-NWs@WCF | 0.00812[d] | 4.7368[d] | [175] |
| CE-PAM-CSS (20 ℃) | 64[a] | 163.17[a] | This work |
| | 18.824[b] | 47.99[b] | |
| | 1.829[d] | 4.661[d] | |
| CE-PAM-CSS (-20 ℃) | 54.4[a] | 163.2[a] | |
| | 16[b] | 48[b] | |

| | | | |
|---|---|---|---|
| | | 1.554[d] | 4.663[d] |

[a] Normalized based on active materials.

[b] Normalized based on electrode weight.

[c] Normalized based on total cell weight of electrodes, electrolyte, and separator.

[d] Normalized based on composite device.

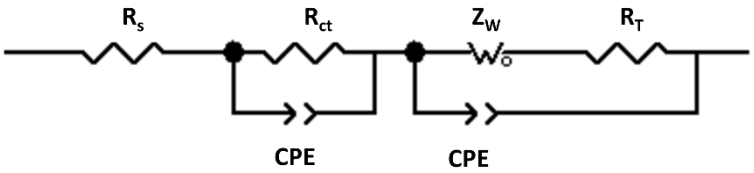


**Figure 7.8** Schematic of the equivalent circuit used in the EIS measurements.

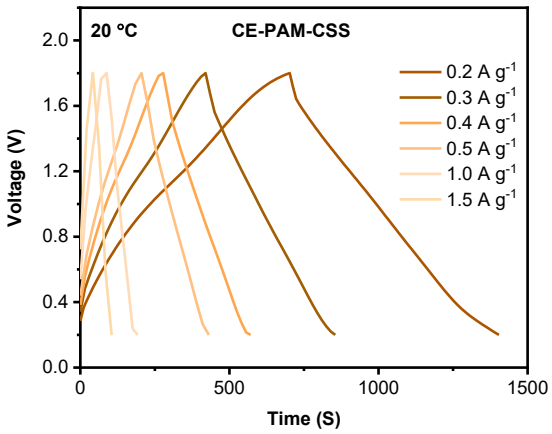


**Figure 7.9** GCD profiles of CE-PAM-CSS at different current densities at 20 °C.

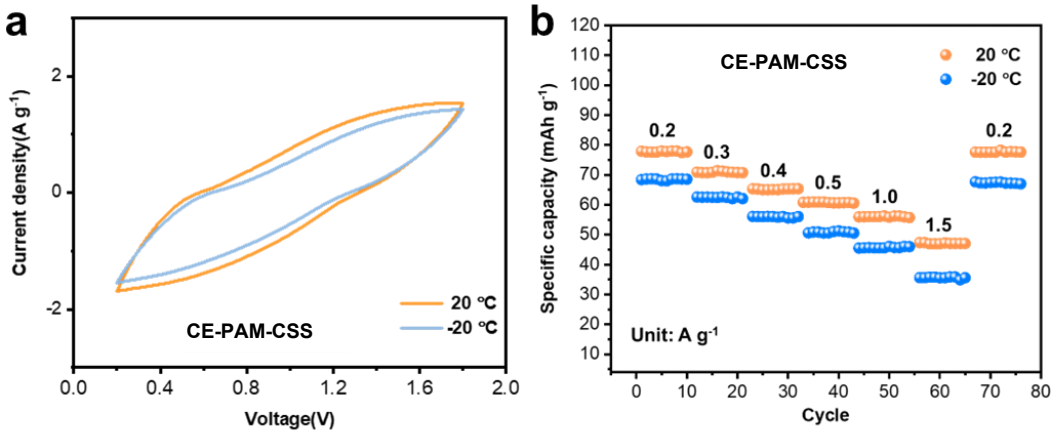


**Figure 7.10** (a) CV curves of CE-PAM-CSS at -20 ℃ and 20 ℃ scanned at the rate of 5 mV $s^{-1}$. (b) Rate performance of CE-PAM-CSS at -20 ℃ and 20 ℃.

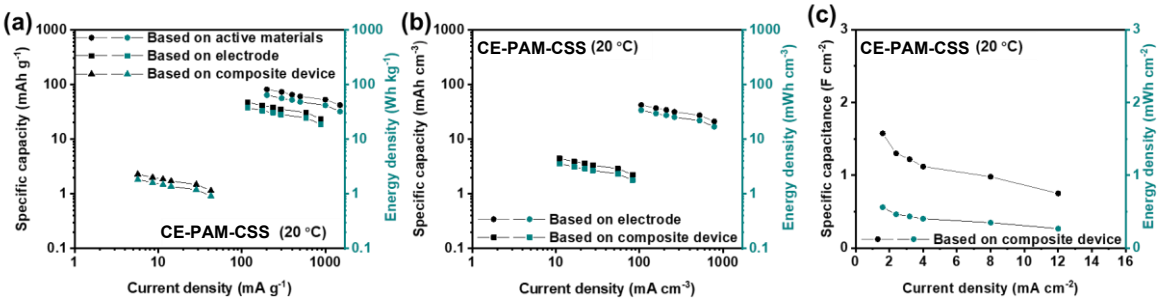


**Figure 7.11** (a) Gravimetric, (b) volumetric, and (c) areal capacity and energy density of CE-PAM-CSS at 20 ℃.

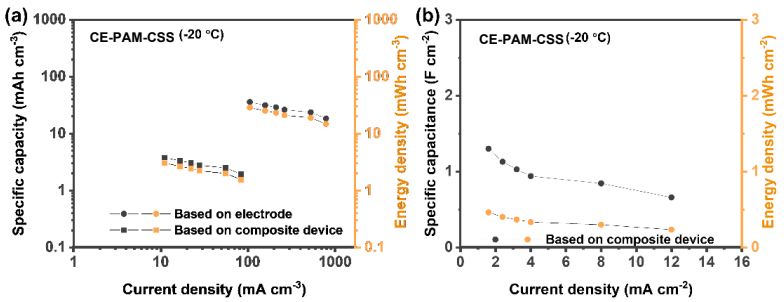


**Figure 7.12** (a) Volumetric and (b) areal capacity and energy density of CE-PAM-CSS at -20 ℃.

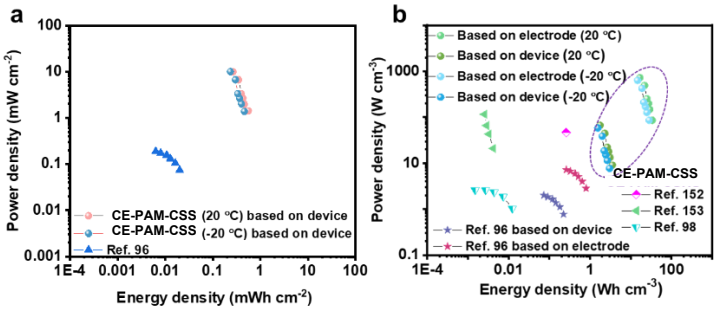


**Figure 7.13** Ragone plot of (a) areal energy density and (b) power density for CE-PAM-CSS at -20 ℃ and 20 ℃ compared to literature data.

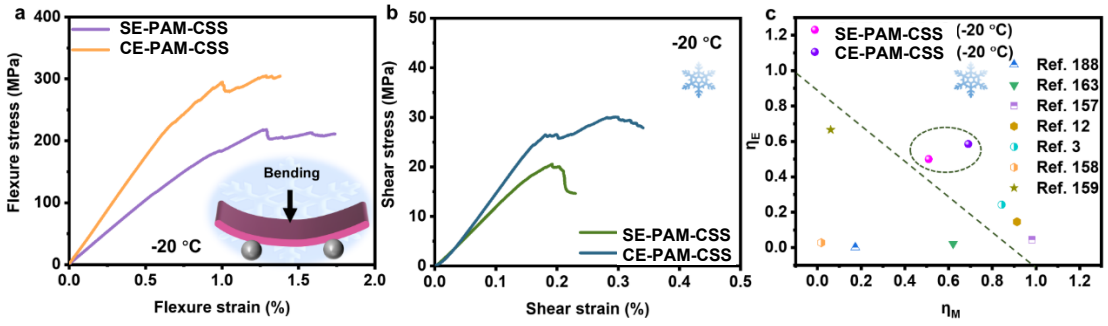


**Figure 7.14** The multifunctionality evaluation of CSSs at -20 ℃. (a) Three-point bending tests of SE-PAM-CSS and CE-PAM-CSS. (b) Shear stress curves of SE-PAM-CSS and CE-PAM-CSS. (c) Ragone plot of the re ($\eta_{ME}$) of SE-PAM-CSS and CE-PAM-CSS compared with other devices reported in the literature.

The mechanical properties of the CSSs were studied, followed by an in-depth evaluation of their multifunctionality. Results from the three-point bending tests indicate that the CE-PAM-CSS sample outperforms the SE-PAM-CSS, with a flexural strength of 293.78 MPa and a flexural modulus of 29.28 GPa, compared to 218.1 MPa and 16.91 GPa, respectively, of the SE-PAM-CSS (Fig. 7.14a). This enhancement can be ascribed to the formation of SHB induced by the synergistic effect of $ClO_4^-$ and EG.

Moreover, shear stress is another key factor affecting mechanical strength, as it directly correlates with the interfacial adhesion forces between composite layers. These adhesion forces, in turn, control the efficiency of load transfer across the device structure. As shown in Fig. 7.14b, the CE-PAM-CSS exhibited a shear stress of 26.45 MPa, exceeding that of SE-PAM-CSS (20.55 MPa), thereby significantly improving its overall mechanical strength due to the formation of SHB in composite electrolyte.

Based on the combined assessment of electrochemical and mechanical performance, the concept of multifunctional efficiency $\eta_{ME}$ [5] was introduced, which can be described as $\eta_{ME} = \eta_M + \eta_E$, where $\eta_M$ is the mechanical efficiency, and $\eta_E$ presents the electrochemical efficiency. Specifically, $\eta_M$ is the ratio of the mechanical performance (e.g., flexural modulus and strength) of the structural device to that of a pure carbon fiber composite, while $\eta_E$ compares the electrochemical capacity of the CSSs with that of a Zn-ion hybrid supercapacitor using liquid electrolyte, both under zero external load. Previous studies suggest that an $\eta_{ME}$ value greater than 1 signifies that multifunctional energy storage devices provide a weight-saving benefit over traditional monofunctional systems [3]. Quantitative analysis shows that the CE-PAM-CSS device achieves 69.0% of the flexural strength and 54.1% of the areal capacitance relative to the baseline samples, resulting in an $\eta_{ME}$ of 1.23, higher than that of the SE-PAM-CSS (1.09). In Fig. 7.14c, the $\eta_{ME}$ of CE-PAM-CSS exhibits superior performance compared to previously reported systems [3, 12, 157-159, 188], indicating a significant advancement achieved by CE-PAM-CSS in integrating mechanical and electrochemical functionalities.

## 7.4 In situ mechano-electrochemical tests of CSSs

An in situ mechano-electrochemical analysis was implemented to characterize the long-term durability of CSSs under cyclic three-point bending tests at subzero temperatures. As for the loading-unloading process, the time for one mechanical cycle is about 1000 s. As displayed in Fig. 7.15a, the SE-PAM-CSS exhibits a capacity retention of 111.2% after 2000 cycles at -20 °C. However, under cyclic loading-unloading process, this value declines to 72.8% after 938 cycles, with notable fluctuations in stability. In contrast, the CE-PAM-CSS displays exceptional cycling stability, maintaining a capacity retention of 103.1% after 2000 cycles, with only a slight decrease to 90.9% under identical stress conditions (Fig. 7.15b) at -20 °C. In the corresponding successive bending cycle tests, the SE-PAM-CSS shows an almost plateau with a certain degree of reduction in maximum stress in the final several cycles, while the CE-PAM-CSS demonstrates a plateau with no significant decline. In the corresponding final ten mechanical stress cycles, SE-PAM-CSS and CE-PAM-CSS both display integrality and symmetry, consistent with the first ten cycles (Fig. 7.16a-b), indicating the durability of the entire device. Following mechanical stress cycling, obvious ripple propagation is observed in the GCD curves of SE-PAM-CSS (Fig. 7.16c), whereas only moderate ripples appear on that of CE-PAM-CSS at the 2000th electrochemical cycles (Fig. 7.15c). The CE-PAM-CSS exhibits stable repeatability in the associated cyclic flexural stress-strain curves (Fig. 7.15d).

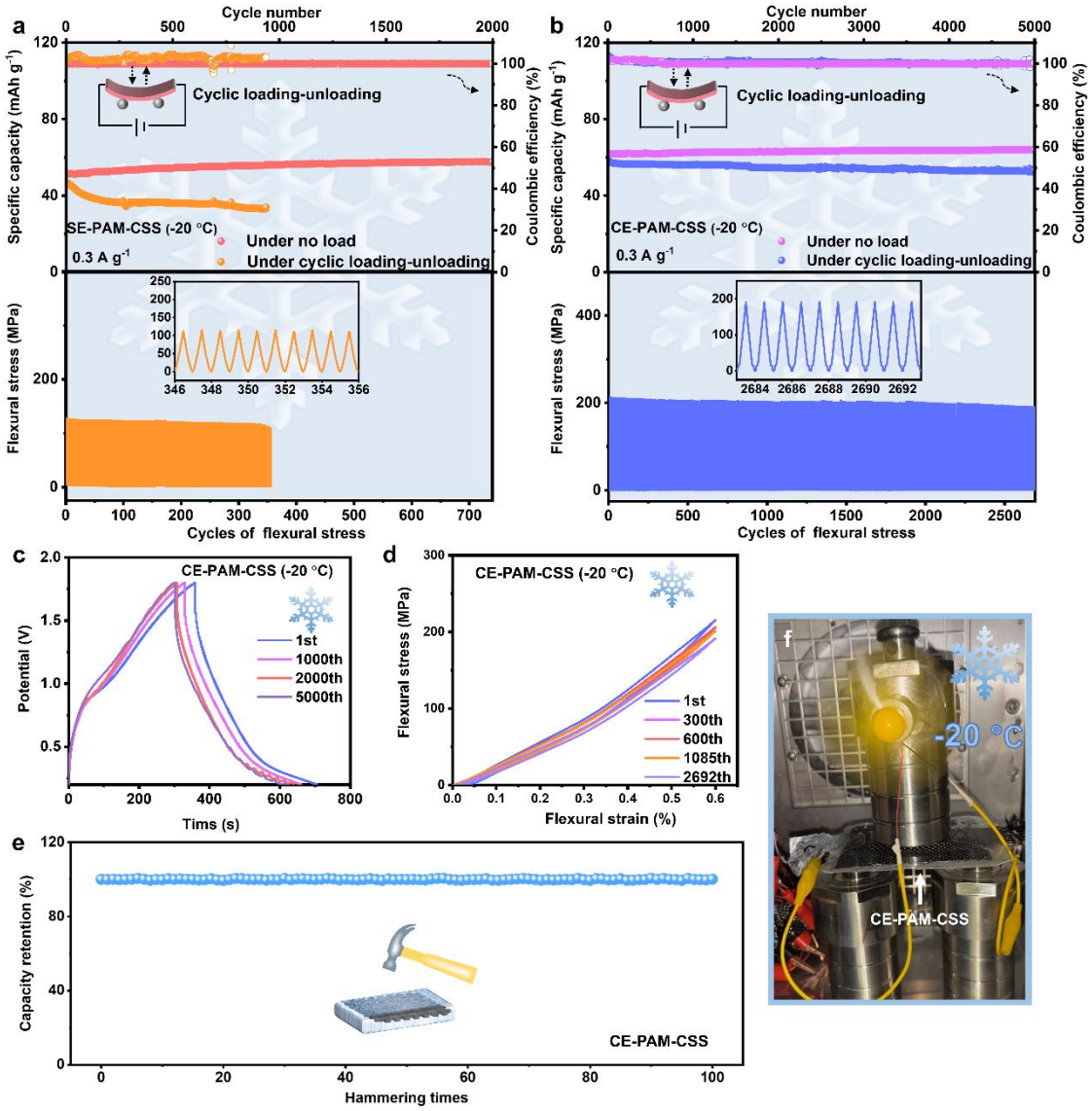


**Figure 7.15** In situ mechano-electrochemical tests of SE-PAM-CSS and CE-PAM-CSS under cyclic external force at subzero temperature. Cycling stability of (a) SE-PAM-CSS and (b) CE-PAM-CSS under no load or cyclic loading-unloading process up to a flexural strain of 0.6% during the in situ mechano-electrochemical test at -20 °C. (c) Related GCD curves of CE-PAM-CSS at different cycles under cyclic stress at -20 °C. (d) Associated cyclic flexural stress-strain curves of CE-PAM-CSS at differential stress cycles at -20 °C. (e) Capacity retention of CE-PAM-CSS encased in ice subjected to repeated violent hammer strikes. (f) Practical application of suspended CE-PAM-CSS at -20 °C.

In Fig. 7.16d, the flexural stress-strain curves of SE-PAM-CSS decrease in maximum stress from the first stress cycle to the 356th cycle. Scanning electron microscopy (SEM) was employed to examine the cross-sectional morphology of SE-PAM-CSS and CE-PAM-CSS before and after loading-unloading cycling. SEM picture of initial SE-PAM-CSS reveals a uniform and dense composite structure (Fig. 7.17a). However, after loading-unloading and charge-discharge cycling, the device exhibits significant cracks within the SE-PAM electrolyte matrix and along the electrode-electrolyte interface (Fig. 7.17b). Conversely, the CE-PAM-CSS device demonstrates remarkable structural stability, with only minor cracks developed in the electrolyte (Fig. 7.18a-b). This enhanced electrochemical cycling stability under cyclic mechanical stress at low temperature can be ascribed to the low temperature tolerance of the strong SHB interaction in the CE-PAM that simultaneously enhances the mechanical stiffness and toughness of the composite electrolyte.

The functionality of CE-PAM-CSS under mechanical stress at low temperature was evaluated. It shows remarkable stability throughout 100 cycles of high-intensity hammer strikes (Fig. 7.15e). As displayed in Fig. 7.15f, the suspended CE-PAM-CSS is capable of operating a small fan at subzero temperatures.

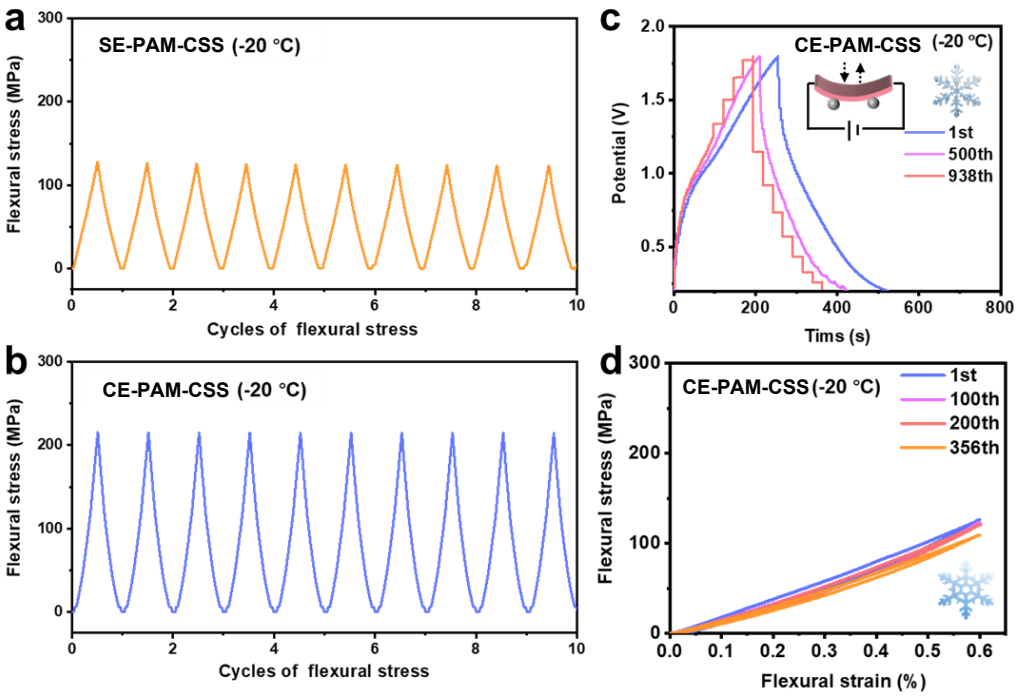


**Figure 7.16** (a) Successive bending cycle curves of SE-PAM-CSS during the first ten cycles at -20 ℃. (b) Successive bending cycle curves of CE-PAM-CSS during the first ten cycles at -20 ℃. (c) Related GCD curves of SE-PAM-CSS at different cycles under cyclic stress at -20 ℃. (d) Cyclic flexural stress-strain curves of SE-PAM-CSS at different stress cycles at -20 ℃.

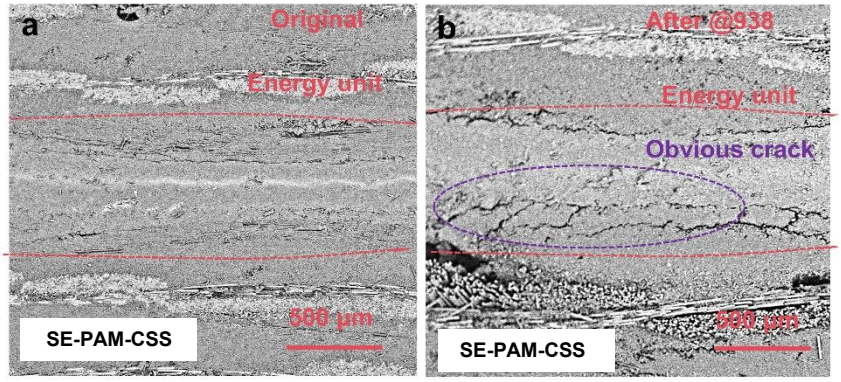


**Figure 7.17** Cross-sectional SEM images of SE-PAM-CSS (a) before and (b) after

cycling.

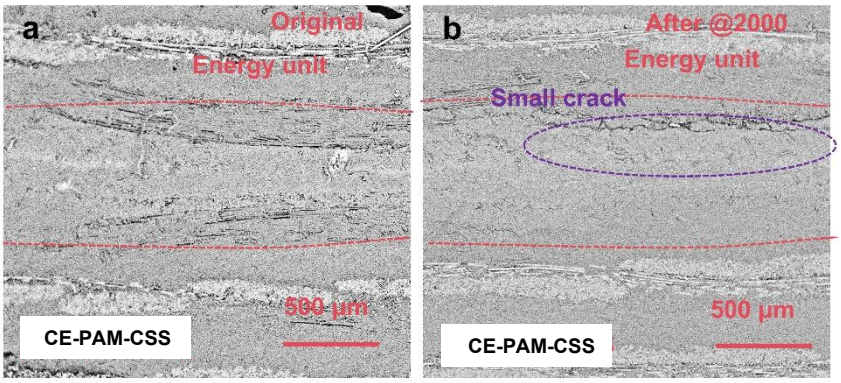


**Figure 7.18** Cross-sectional SEM images of CE-PAM-CSS (a) before and (b) after cycling.

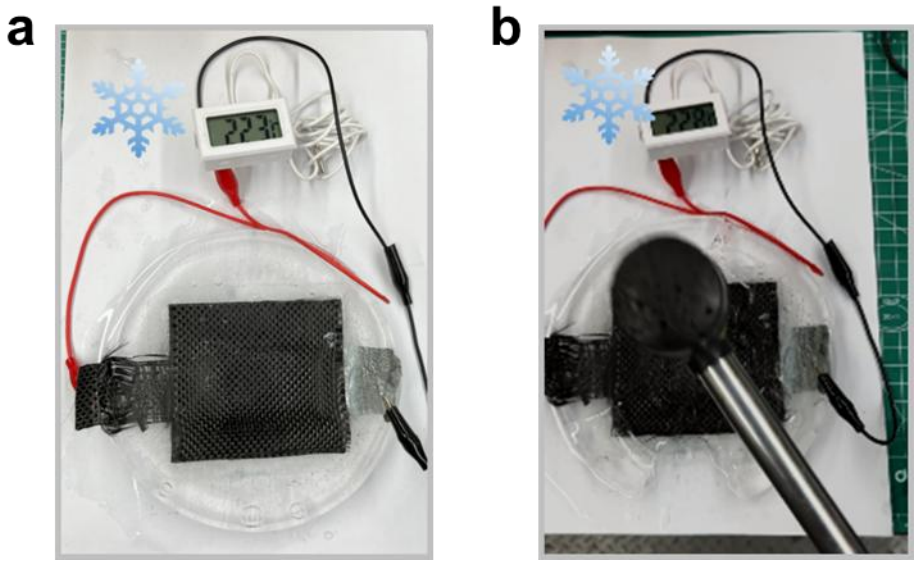


**Figure 7.19** (a) Application of CE-PAM-CSS sealed in solid ice and (b) subjected to repeated violent hammer strikes.

In Fig. 7.19a-b, CE-PAM-CSS encased in ice can light up an electronic thermometer

and still work under repeated hammer strikes. These results provide compelling evidence that the CE-PAM-CSS can sustain both exceptional mechanical and electrochemical performance at subzero temperatures. This work provides valuable insights for the design optimization of CSSs, potentially expanding their applicability at subzero temperatures.

## 7.5 Summary

The synergistic effect of chaotropic $ClO_4^-$ anions and EG was elucidated that it can break the trade-off between stiffness and toughness in CE-PAM polymer electrolyte. Simulation results confirm that the mechanical enhancement is attributed to the strong HB among the $ClO_4^-$, EG molecules, and polymer chains, replacing the weak HB formed between the EG and polymer chains in anti-freezing EG-based electrolyte without $ClO_4^-$. The composite electrolyte, with enhanced and elongated HB, requires greater force to deform and absorbs more energy, allowing for significant without fracture. The CE-PAM electrolyte exhibits improved elastic modulus (6.8 kPa) and breaking energy (270 kJ $m^{-3}$), demonstrating the enhanced stiffness and toughness. The energy density of the fabricated CE-PAM-CSS reaches 54.4 Wh $kg^{-1}$ at the power density of 163.2 W $kg^{-1}$ at subzero temperatures. The CSS displays flexural modulus and flexural strength values of 29.28 GPa and 293.78 MPa, respectively. In-situ mechano-electrochemical testing reveals that, due to the robust SHB in electrolyte, the developed device maintains 90% of its initial capacity after 2000 cycles under cyclic mechanical stress at -20 ℃. The capability of the CSS to simultaneously maintain mechanical integrity and electrochemical functionality at subzero temperatures presents feasible approaches to design and fabrication of CSSs.

# Chapter 8 Conclusion and Recommendations for Future Work

## 8.1 Conclusion

Considering the demand for high energy density, lightweight energy devices have attracted considerable attention from researchers. In this thesis, the design of multifunctional CSSs was proposed to optimize the balance between electrochemical performance and mechanical properties. The coupling effects between electrochemical and mechanical performance, structural failure mechanisms, and capacity decay under mechanical loads and other extreme conditions were systematically investigated. Thus, firstly, it was proposed that external mechanical stress accelerates energy unit failure caused by the electrochemical cycling. In the second study, a snap-on electrode/electrolyte interface was designed to reinforce the structural integrity of the energy storage unit, thereby enhancing electrochemical cycling stability under external stress. In the third study, the impact of deformation induced by external loads on the electric field was examined and MXene-based composite electrolyte was fabricated to uniformly distribute the electric field. In the fourth study, an anti-freezing stiff and tough composite electrolyte was developed to maintain stable electrochemical cycling performance and high mechanical strength under bending stress at low temperatures. The key findings from each study are outlined below:

Despite some advancements in CSSs, research on the effect of electrochemical cycling on structural failure, particularly under applied loads, remains limited. Some dedicated simulations for CSSs also remain rare. The electrochemical cycling-induced fatigue

failure of an all-solid-state Zn-ion CSSs integrating the composite electrodes and electrolytes was investigated. It was demonstrated that the electrochemical cycling process induces mechanical-like fatigue stress as a result of volume changes caused by the ion concentration gradient. Furthermore, the combination of charge-discharge fatigue stress and applied loads leads to a greater cumulative fatigue stress, which ultimately promotes structural degradation and electrochemical deterioration.

The snap-on structure was designed to interlock the electrode/electrolyte interface, thereby preventing sliding between multiple layers in the energy storage unit. The unique energy storage unit structure was fabricated by the in-situ polymerization process. The snap-on structure of the CSS can enhance adhesive bonding at the electrolyte and electrode interface, resulting in improved shear stress. The strong shear strength enables the multiple layers to share a nearly common neutral axis, thereby allowing effective load transfer in the battery laminate during a three-point bending test, ultimately enhancing the overall mechanical properties. The interlocked interface more effectively transfers load than the sandwich structure. The strong adhesive bonding of the structural supercapacitors provides high specific capacitance and stable cycling performance, even under external bending.

Deformation in CSSs under external loading induces heterogeneous electric field distributions. Therefore, maintaining a uniform electric field is essential for improving the electrochemical performance of CSSs. A Zn-ion material-level hybrid CSS system with an MXene-based electrolyte was fabricated to mitigate the perturbations in electric field. The polarized electric field, generated through hydrogen bonds between MXene and polymer chains, effectively modulates the electric field distribution within CSS under mechanical stress. Furthermore, MXene significantly enhances the ionic

conductivity of electrolytes and improves mechanical properties.

It is challenging to simultaneously fulfill the dual mechanical requirements of stiffness and toughness for composite electrolytes operating at low temperatures, where the high stiffness enables the electrolyte to effectively transfer mechanical load between layers, while the high toughness prevents crack propagation under loading conditions.

A multifunctional freeze-tolerant structural supercapacitor equipped with a rationally designed composite electrolyte with chaotropic $ClO_4^-$ additives exhibiting stable cycling performance under mechanical stress at subzero temperatures. Unlike the conventional Hofmeister effect in which $ClO_4^-$ promotes elastic strain while compromising stiffness [103], the synergistic effect of $ClO_4^-$ and EG additives in the designed electrolyte results in increases of both elastic strain and stiffness, leading to enhanced toughness, compared to EG-based electrolytes in the absence of $ClO_4^-$.

For the scalability, it is important to maintain the stable and consistent properties of the device, while minimizing the variation of water content, size, and state of the hydrogel that may significantly affect the properties. The cost of the device ranges from 1071-1428 $.

## 8.2 Recommendations for Future Work

Fundamental understanding of mechano-electrochemical coupling remains a critical area of research in CSESDs. In such systems, the interactions between applied mechanical stress/strain and electrochemical processes are complex and often lead to structural failure and deterioration in electrochemical performance. Investigating mechano-electrochemical coupling is an essential strategy for optimizing both the design and application of CSESDs. Volume changes in the electrodes during

charge/discharge cycling can lead to the debonding of the electrode/electrolyte interface or the formation of cracks in both the electrode and electrolyte materials. This degradation significantly increases impedance and reduces system performance, resulting in additional heterogeneity of stress distribution and reaction dynamics. Moreover, the accumulation of point defects and dislocations in both the electrode and electrolyte matrices, which are influenced by the applied mechanical loads, further exacerbates these effects. There is a clear need for further research to explore the coupling between mechanical forces and electrochemical performance, with a particular focus on the distinct failure mechanisms induced by external mechanical forces versus electrochemical cycling. Furthermore, understanding the mechanisms of crack propagation under the combined influence of electrochemical and mechanical loading is crucial, as well as examining the roles of varying voltages, currents, and external forces in these processes. To minimize mass and achieve optimal multifunctional performance, CSESDs must simultaneously exhibit both superior mechanical and electrochemical properties. These systems are typically required to possess high mechanical strength in multiple directions. Despite the use of CFs, conventional rectangular-shaped batteries often meet only the tensile and shear strength requirements, while their bending strength remains relatively low. Thus, to address this limitation, strategies such as incorporating binders and adopting solid-state electrolytes are essential for improving both mechanical durability and electrochemical performance in CSESDs [55]. CSESDs are typically required to demonstrate a cycle life of hundreds or even thousands of cycles. However, CF-based electrodes generally exhibit a cycle life limited to only tens of cycles. Therefore, further modifications, such as exploring surface coating like $Al_2O_3$ on carbon fibers on enhance cycling stability, are necessary to enhance their cycling performance [133].

Currently, most studies on CSESDs remain in the early stages of concept demonstration, with limited consideration of management and cooling systems in practical applications. CSESDs are often subjected to more extreme operating conditions, and their performance stability under mechanical loads is crucial for real-world implementation. For instance, continuous external loads and resulting deformations can lead to misalignment and the formation of cracks within the energy unit. Therefore, the design of structural batteries must account for these challenges.

Conversely, electrochemical cycling can also compromise mechanical performance. The volume changes of electrodes during charge-discharge cycles can adversely affect the interfaces between electrode particles and other components [163, 189], and result in worse mechanical performance, especially flexural properties. Similarly, the evolution of the solid electrolyte interphase (SEI) can also influence the interfaces within the system. Repeated lithiation and delithiation cycles can degrade CFs, potentially resulting in the mechanical failure of the entire device. Although such fatigue tests have seldom been included in previous studies, they should be given greater emphasis in future research.

Safety is even more critical for CSESDs due to the mechanically demanding operating conditions they endure. Consequently, safety requirements for structural batteries should be more stringent than those for conventional batteries. Additionally, the mass and volume of any additional protective measures must be considered when evaluating the multifunctional efficiency of the entire system. As discussed in the studies [156], safety tests should be indispensable when the field approaches practical applications. To achieve a high multifunctional efficiency and enhanced safety simultaneously, researchers may consider adopting nonflammable liquid electrolytes, solid-state

electrolytes, thermally stable separators and binders, smart designs of current collectors, and strong and lightweight external protections.

The integration of CF current collectors with active electrode materials in a scalable and cost-effective manner remains a significant challenge. Additionally, the maintenance and replacement of these systems must be considered for practical applications. For instance, the maintenance or repair of CSESDs embedded in aircraft wings or vehicle chassis is likely to be far more complex than that of CSESDs used in portable electronics. Particularly, when multiple cells are integrated into a single structural unit, it may be necessary to replace all cells and even the structural components, even if only one cell experiences a mechanical or electrochemical malfunction. [86]. Therefore, the development of advanced battery management systems and a comprehensive understanding of maintenance are crucial, given the strong coupling between electrochemical and mechanical processes [95]. Certain applications, such as those in aviation and military sectors, can accommodate higher costs. However, for large-scale applications like electric vehicles, the cost of structural batteries must be reduced to a more economically feasible level.

# References

[1] D. Carlstedt, L.E. Asp, Performance analysis framework for structural battery composites in electric vehicles, Composites, Part B 186 (2020).

[2] L.E. Asp, M. Johansson, G. Lindbergh, J. Xu, D. Zenkert, Structural battery composites: a review, Funct. Compos. Struct. 1(4) (2019).

[3] Z. Sha, F. Huang, Y. Zhou, J. Zhang, S. Wu, J. Chen, S.A. Brown, S. Peng, Z. Han, C.-H. Wang, Synergies of vertical graphene and manganese dioxide in enhancing the energy density of carbon fibre-based structural supercapacitors, Compos. Sci. Technol. 201 (2021).

[4] H. Zhou, H. Li, L. Li, T. Liu, G. Chen, Y. Zhu, L. Zhou, H. Huang, Structural composite energy storage devices — a review, Mater. Today Energy 24 (2022).

[5] M.F. Ashby, Multi-objective optimization in material design and selection, Acta Mater. 48(1) (2000) 359-369.

[6] Y. Xu, W. Lu, G. Xu, T.-W. Chou, Structural supercapacitor composites: A review, Compos. Sci. Technol. 204 (2021).

[7] S. Yadav, Z. Kamble, B.K. Behera, Advances in multifunctional textile structural power composites: a review, J. Mater. Sci. 57(36) (2022) 17105-17138.

[8] B. Tynan, Y. Zhou, S.A. Brown, L. Dai, A.N. Rider, C.H. Wang, Structural supercapacitor electrodes for energy storage by electroless deposition of MnO2 on carbon nanotube mats, Compos. Sci. Technol. 238 (2023).

[9] T. Pereira, Z. Guo, S. Nieh, J. Arias, H.T. Hahn, Embedding thin-film lithium energy cells in structural composites, Compos. Sci. Technol. 68(7-8) (2008) 1935-1941.

[10] K.-J. Wu, W.-B. Young, C. Young, Structural supercapacitors: A mini-review of their fabrication, mechanical & electrochemical properties, J. Energy Storage 72 (2023).

[11] L.E. Asp, K. Bouton, D. Carlstedt, S. Duan, R. Harnden, W. Johannisson, M. Johansen, M.K.G. Johansson, G. Lindbergh, F. Liu, K. Peuvot, L.M. Schneider, J. Xu, D. Zenkert, A Structural Battery and its Multifunctional Performance, Adv. Energy Sustainability Res. 2(3)

(2021).

[12] B.K. Deka, A. Hazarika, J. Kim, Y.-B. Park, H.W. Park, Multifunctional CuO nanowire embodied structural supercapacitor based on woven carbon fiber/ionic liquid–polyester resin, Composites, Part A 87 (2016) 256-262.

[13] W. Johannisson, D. Zenkert, G. Lindbergh, Model of a structural battery and its potential for system level mass savings, Multifunct. Mater. 2(3) (2019).

[14] T. Jin, G. Singer, K. Liang, Y. Yang, Structural batteries: Advances, challenges and perspectives, Mater. Today 62 (2023) 151-167.

[15] R. Chaudhary, J. Xu, Z. Xia, L.E. Asp, Unveiling the Multifunctional Carbon Fiber Structural Battery, Adv. Mater. 36(48) (2024) e2409725.

[16] P. Attar, J. Galos, A.S. Best, A.P. Mouritz, Compression properties of multifunctional composite structures with embedded lithium-ion polymer batteries, Compos. Struct. 237 (2020).

[17] K. Pattarakunnan, J. Galos, R. Das, A.P. Mouritz, Tensile properties of multifunctional composites embedded with lithium-ion polymer batteries, Composites, Part A 136 (2020).

[18] L. Zhang, S. Lu, X. Wang, K. Ma, H. Liu, L. Zhou, Manufacture and mechanical properties of sandwich structure-battery composites, J. Polym. Eng. 39(9) (2019) 838-843.

[19] J.P. Thomas, S.M. Qidwai, W.R. Pogue, G.T. Pham, Multifunctional structure-battery composites for marine systems, J. Compos. Mater. 47(1) (2012) 5-26.

[20] J. Galos, A. Khatibi, A. Mouritz, Vibration and acoustic properties of composites with embedded lithium-ion polymer batteries, Compos. Struct. 220 (2019) 677-686.

[21] J. Galos, A.S. Best, A.P. Mouritz, Multifunctional sandwich composites containing embedded lithium-ion polymer batteries under bending loads, Mater. Des. 185 (2020).

[22] F. Wang, Q. Han, Z. Yi, D. Geng, X. Li, Z. Wang, L. Wang, Synthesis and performances of carbon fiber@Co3O4 based on metal organic frameworks as anode materials for structural lithium-ion battery, J. Electroanal. Chem. 807 (2017) 196-202.

[23] P. Ladpli, R. Nardari, F. Kopsaftopoulos, F.-K. Chang, Multifunctional energy storage

composite structures with embedded lithium-ion batteries, J. Power Sources 414 (2019) 517-529.

[24] E. Jacques, M. Hellqvist Kjell, D. Zenkert, G. Lindbergh, M. Behm, Expansion of carbon fibres induced by lithium intercalation for structural electrode applications, Carbon 59 (2013) 246-254.

[25] S. Duan, A.H.S. Iyer, D. Carlstedt, F. Rittweger, A. Sharits, C. Maddox, K.-R. Riemschneider, D. Mollenhauer, M. Colliander, F. Liu, L.E. Asp, Effect of lithiation on the elastic moduli of carbon fibres, Carbon 185 (2021) 234-241.

[26] S.A. Mirdehghan, Fibrous polymeric composites, Engineered Polymeric Fibrous Materials2021, pp. 1-58.

[27] G. Fredi, S. Jeschke, A. Boulaoued, J. Wallenstein, M. Rashidi, F. Liu, R. Harnden, D. Zenkert, J. Hagberg, G. Lindbergh, P. Johansson, L. Stievano, L.E. Asp, Graphitic microstructure and performance of carbon fibre Li-ion structural battery electrodes, Multifunct. Mater. 1(1) (2018).

[28] K. Moyer, C. Meng, B. Marshall, O. Assal, J. Eaves, D. Perez, R. Karkkainen, L. Roberson, C.L. Pint, Carbon fiber reinforced structural lithium-ion battery composite: Multifunctional power integration for CubeSats, Energy Storage Mater. 24 (2020) 676-681.

[29] Z. Zhang, W. Yang, L. Cheng, W. Cao, M. Sain, J. Tan, A. Wang, H. Jia, Carbon Fibers with High Electrical Conductivity: Laser Irradiation of Mesophase Pitch Filaments Obtains High Graphitization Degree, ACS Sustainable Chem. Eng. 8(48) (2020) 17629-17638.

[30] J.S. Sanchez, J. Xu, Z. Xia, J. Sun, L.E. Asp, V. Palermo, Electrophoretic coating of LiFePO4/Graphene oxide on carbon fibers as cathode electrodes for structural lithium ion batteries, Compos. Sci. Technol. 208 (2021).

[31] J.M. Pappas, A.R. Thakur, X. Dong, Effects of cathode doping on 3D printed continuous carbon fiber structural battery composites by UV-assisted coextrusion deposition, J. Compos. Mater. 55(26) (2021) 3893-3908.

[32] K. Moyer, N.A. Boucherbil, M. Zohair, J. Eaves-Rathert, C.L. Pint, Polymer reinforced

carbon fiber interfaces for high energy density structural lithium-ion batteries, Sustainable Energy Fuels 4(6) (2020) 2661-2668.

[33] D.K. Lee, H.S. Ryu, C.W. Ahn, H.-J. Jeon, Combining electrospinning and sputtering to improve rechargeable lithium battery cathodes: coating carbon fibre felt with nickel sulfide, Phys. Scr. 91(11) (2016).

[34] C. Shi, M. Yu, Flexible solid-state lithium-sulfur batteries based on structural designs, Energy Storage Mater. 57 (2023) 429-459.

[35] Y.-H. Liu, T. Takasaki, K. Nishimura, M. Yanagida, T. Sakai, Development of fiber-type potassium-based cathode for sodium ion battery, Mater. Lett. 177 (2016) 132-134.

[36] W. Huang, P. Wang, X. Liao, Y. Chen, J. Borovilas, T. Jin, A. Li, Q. Cheng, Y. Zhang, H. Zhai, A. Chitu, Z. Shan, Y. Yang, Mechanically-robust structural lithium-sulfur battery with high energy density, Energy Storage Mater. 33 (2020) 416-422.

[37] J. Chen, Y. Zhou, M.S. Islam, X. Cheng, S.A. Brown, Z. Han, A.N. Rider, C.H. Wang, Carbon fiber reinforced Zn–MnO2 structural composite batteries, Compos. Sci. Technol. 209 (2021).

[38] G. Jiang, N. Jiang, N. Zheng, X. Chen, J. Mao, G. Ding, Y. Li, F. Sun, Y. Li, MOF-derived porous Co3O4-NC nanoflake arrays on carbon fiber cloth as stable hosts for dendrite-free Li metal anodes, Energy Storage Mater. 23 (2019) 181-189.

[39] B.K. Emerson, M.H. Benson, B.J. Neudecker, Power Fibers: Thin-Film Batteries on Fiber Substrates, ITN Energy Systems Inc Littleton Co (2003).

[40] A. Thakur, X. Dong, Printing with 3D continuous carbon fiber multifunctional composites via UV-assisted coextrusion deposition, Manuf. Lett. 24 (2020) 1-5.

[41] G.J.H. Lim, R. Chua, J.J. Koh, K.K. Chan, E.J.J. Tang, V. Teh, M. Srinivasan, Structural and conformable designs for aqueous multifunctional batteries, Mater. Today Energy 33 (2023).

[42] J. Hagberg, H.A. Maples, K.S.P. Alvim, J. Xu, W. Johannisson, A. Bismarck, D. Zenkert, G. Lindbergh, Lithium iron phosphate coated carbon fiber electrodes for structural lithium ion

batteries, Compos. Sci. Technol. 162 (2018) 235-243.

[43] K. Evanoff, J. Benson, M. Schauer, I. Kovalenko, D. Lashmore, W.J. Ready, G. Yushin, Ultra strong silicon-coated carbon nanotube nonwoven fabric as a multifunctional lithium-ion battery anode, ACS Nano 6(11) (2012) 9837-45.

[44] K. Narita, M.A. Citrin, H. Yang, X. Xia, J.R. Greer, 3D Architected Carbon Electrodes for Energy Storage, Adv. Energy Mater. 11(5) (2020).

[45] L.H. Acauan, Y. Zhou, E. Kalfon-Cohen, N.K. Fritz, B.L. Wardle, Multifunctional nanocomposite structural separators for energy storage, Nanoscale 11(45) (2019) 21964-21973.

[46] D. Bresser, D. Buchholz, A. Moretti, A. Varzi, S. Passerini, Alternative binders for sustainable electrochemical energy storage – the transition to aqueous electrode processing and bio-derived polymers, Energy Environ. Sci. 11(11) (2018) 3096-3127.

[47] I. Kovalenko, B. Zdyrko, A. Magasinski, B. Hertzberg, Z. Milicev, R. Burtovyy, I. Luzinov, G. Yushin, A major constituent of brown algae for use in high-capacity Li-ion batteries, Science 334(6052) (2011) 75-9.

[48] L. Liu, Z. Li, Q. Che, Multilayered Membrane Electrolytes Based on Aramid Nanofibers for High-Temperature Proton Exchange Membrane Fuel Cells, ACS Appl. Nano Mater. 2(4) (2019) 2160-2168.

[49] J. Yoon, J. Lee, H. Kim, J. Kim, H.J. Jin, Polymeric Binder Design for Sustainable Lithium-Ion Battery Chemistry, Polymers (Basel) 16(2) (2024).

[50] Z. Zhang, S. Yang, P. Zhang, J. Zhang, G. Chen, X. Feng, Mechanically strong MXene/Kevlar nanofiber composite membranes as high-performance nanofluidic osmotic power generators, Nat. Commun. 10(1) (2019) 2920.

[51] Y. Zhao, X. Li, J. Shen, C. Gao, B. Van der Bruggen, The potential of Kevlar aramid nanofiber composite membranes, J. Mater. Chem. A 8(16) (2020) 7548-7568.

[52] Z. Li, Y. Zhang, T. Liu, X. Gao, S. Li, M. Ling, C. Liang, J. Zheng, Z. Lin, Silicon Anode with High Initial Coulombic Efficiency by Modulated Trifunctional Binder for High-Areal-

Capacity Lithium-Ion Batteries, Adv. Energy Mater. 10(20) (2020).

[53] M. Yang, K. Cao, L. Sui, Y. Qi, J. Zhu, A. Waas, E.M. Arruda, J. Kieffer, M.D. Thouless, N.A. Kotov, Dispersions of aramid nanofibers: a new nanoscale building block, ACS Nano 5(9) (2011) 6945-54.

[54] A. Patel, K. Wilcox, Z. Li, I. George, R. Juneja, C. Lollar, S. Lazar, J. Grunlan, W.E. Tenhaeff, J.L. Lutkenhaus, High Modulus, Thermally Stable, and Self-Extinguishing Aramid Nanofiber Separators, ACS Appl. Mater. Interfaces 12(23) (2020) 25756-25766.

[55] T. Jin, Y. Ma, Z. Xiong, X. Fan, Y. Luo, Z. Hui, X. Chen, Y. Yang, Bioinspired, Tree-Root-Like Interfacial Designs for Structural Batteries with Enhanced Mechanical Properties, Adv. Energy Mater. 11(25) (2021).

[56] L. Valentini, S. Bittolo Bon, S. Signetti, N.M. Pugno, Graphene-Based Bionic Composites with Multifunctional and Repairing Properties, ACS Appl. Mater. Interfaces 8(12) (2016) 7607-12.

[57] X. Han, L. Lv, D. Yu, X. Wu, C. Li, Conductive Core-Shell Aramid Nanofibrils: Compromising Conductivity with Mechanical Robustness for Organic Wearable Sensing, ACS Appl. Mater. Interfaces 11(3) (2019) 3466-3473.

[58] F. Wang, Y. Wu, Y. Huang, Novel application of graphene oxide to improve hydrophilicity and mechanical strength of aramid nanofiber hybrid membrane, Composites, Part A 110 (2018) 126-132.

[59] M. Wang, C. Wang, Z. Fan, G. Wu, L. Liu, Y. Huang, Aramid nanofiber-based porous membrane for suppressing dendrite growth of metal-ion batteries with enhanced electrochemistry performance, Chem. Eng. J. 426 (2021).

[60] X.-B. Cheng, C.-Z. Zhao, Y.-X. Yao, H. Liu, Q. Zhang, Recent Advances in Energy Chemistry between Solid-State Electrolyte and Safe Lithium-Metal Anodes, Chem 5(1) (2019) 74-96.

[61] Q. Cheng, T. Jin, Y. Miao, Z. Liu, J. Borovilas, H. Zhang, S. Liu, S.-Y. Kim, R. Zhang, H. Wang, X. Chen, L.-Q. Chen, J. Li, W. Min, Y. Yang, Stabilizing lithium plating in polymer

electrolytes by concentration-polarization-induced phase transformation, Joule 6(10) (2022) 2372-2389.

[62] L. Yue, J. Ma, J. Zhang, J. Zhao, S. Dong, Z. Liu, G. Cui, L. Chen, All solid-state polymer electrolytes for high-performance lithium ion batteries, Energy Storage Mater. 5 (2016) 139-164.

[63] A. Manthiram, X. Yu, S. Wang, Lithium battery chemistries enabled by solid-state electrolytes, Nat. Rev. Mater. 2(4) (2017).

[64] J. Lee, T. Howell, M. Rottmayer, J. Boeckl, H. Huang, Free-Standing PEO/LiTFSI/LAGP Composite Electrolyte Membranes for Applications to Flexible Solid-State Lithium-Based Batteries, J. Electrochem. Soc. 166(2) (2019) A416-A422.

[65] V.A. Soloukhin, J.C.M. Brokken-Zijp, O.L.J. van Asselen, G. de With, Physical Aging of Polycarbonate: Elastic Modulus, Hardness, Creep, Endothermic Peak, Molecular Weight Distribution, and Infrared Data, Macromolecules 36(20) (2003) 7585-7597.

[66] J.F. Snyder, R.H. Carter, E.D. Wetzel, Electrochemical and Mechanical Behavior in Mechanically Robust Solid Polymer Electrolytes for Use in Multifunctional Structural Batteries, Chem. Mater. 19(15) (2007) 3793-3801.

[67] J.F. Snyder, E.D. Wetzel, C.M. Watson, Improving multifunctional behavior in structural electrolytes through copolymerization of structure- and conductivity-promoting monomers, Polymer 50(20) (2009) 4906-4916.

[68] N. Boaretto, L. Meabe, M. Martinez-Ibañez, M. Armand, H. Zhang, Review—Polymer Electrolytes for Rechargeable Batteries: From Nanocomposite to Nanohybrid, J. Electrochem. Soc. 167(7) (2020).

[69] S. Fu, L.-L. Zuo, P.-S. Zhou, X.-J. Liu, Q. Ma, M.-J. Chen, J.-P. Yue, X.-W. Wu, Q. Deng, Recent advancements of functional gel polymer electrolytes for rechargeable lithium–metal batteries, Mater. Chem. Front. 5(14) (2021) 5211-5232.

[70] X. Cheng, J. Pan, Y. Zhao, M. Liao, H. Peng, Gel Polymer Electrolytes for Electrochemical Energy Storage, Adv. Energy Mater. 8(7) (2017).

[71] M. Wang, D. Vecchio, C. Wang, A. Emre, X. Xiao, Z. Jiang, P. Bogdan, Y. Huang, N.A. Kotov, Biomorphic structural batteries for robotics, Sci Robot 5(45) (2020).

[72] L. Yao, K. Zheng, N. Koripally, N. Eedugurala, J.D. Azoulay, X. Zhang, T.N. Ng, Structural pseudocapacitors with reinforced interfaces to increase multifunctional efficiency, Sci. Adv. 9(25) (2023) eadh0069.

[73] W. Johannisson, N. Ihrner, D. Zenkert, M. Johansson, D. Carlstedt, L.E. Asp, F. Sieland, Multifunctional performance of a carbon fiber UD lamina electrode for structural batteries, Compos. Sci. Technol. 168 (2018) 81-87.

[74] S. Sasidharan, A. Anand, Epoxy-Based Hybrid Structural Composites with Nanofillers: A Review, Industrial & Engineering Chemistry Research 59(28) (2020) 12617-12631.

[75] N. Ihrner, W. Johannisson, F. Sieland, D. Zenkert, M. Johansson, Structural lithium ion battery electrolytesviareaction induced phase-separation, J. Mater. Chem. A 5(48) (2017) 25652-25659.

[76] L.M. Schneider, N. Ihrner, D. Zenkert, M. Johansson, Bicontinuous Electrolytes via Thermally Initiated Polymerization for Structural Lithium Ion Batteries, ACS Appl. Energy Mater. 2(6) (2019) 4362-4369.

[77] K.G. Schell, F. Lemke, E.C. Bucharsky, A. Hintennach, M.J. Hoffmann, Microstructure and mechanical properties of Li0.33La0.567TiO3, J. Mater. Sci. 52(4) (2016) 2232-2240.

[78] Z. Gao, H. Sun, L. Fu, F. Ye, Y. Zhang, W. Luo, Y. Huang, Promises, Challenges, and Recent Progress of Inorganic Solid-State Electrolytes for All-Solid-State Lithium Batteries, Adv. Mater. 30(17) (2018) e1705702.

[79] S.D. Jackman, R.A. Cutler, Effect of microcracking on ionic conductivity in LATP, J. Power Sources 218 (2012) 65-72.

[80] F. Gasco, P. Feraboli, Manufacturability of composite laminates with integrated thin film Li-ion batteries, J. Compos. Mater. 48(8) (2013) 899-910.

[81] H. Chen, C.J. Zhou, X.R. Dong, M. Yan, J.Y. Liang, S. Xin, X.W. Wu, Y.G. Guo, X.X. Zeng, Revealing the Superiority of Fast Ion Conductor in Composite Electrolyte for Dendrite-

Free Lithium-Metal Batteries, ACS Appl. Mater. Interfaces 13(19) (2021) 22978-22986.

[82] X. Ao, X. Wang, J. Tan, S. Zhang, C. Su, L. Dong, M. Tang, Z. Wang, B. Tian, H. Wang, Nanocomposite with fast Li+ conducting percolation network: Solid polymer electrolyte with Li+ non-conducting filler, Nano Energy 79 (2021).

[83] W. Liao, C. Liu, Structural Design of Composite Polymer Electrolytes for Solid-state Lithium Metal Batteries, ChemNanoMat 7(11) (2021) 1177-1187.

[84] A. Li, X. Liao, H. Zhang, L. Shi, P. Wang, Q. Cheng, J. Borovilas, Z. Li, W. Huang, Z. Fu, M. Dontigny, K. Zaghib, K. Myers, X. Chuan, X. Chen, Y. Yang, Nacre-Inspired Composite Electrolytes for Load-Bearing Solid-State Lithium-Metal Batteries, Adv. Mater. 32(2) (2020) e1905517.

[85] S. Zekoll, C. Marriner-Edwards, A.K.O. Hekselman, J. Kasemchainan, C. Kuss, D.E.J. Armstrong, D. Cai, R.J. Wallace, F.H. Richter, J.H.J. Thijssen, P.G. Bruce, Hybrid electrolytes with 3D bicontinuous ordered ceramic and polymer microchannels for all-solid-state batteries, Energy Environ. Sci. 11(1) (2018) 185-201.

[86] T. Dong, J. Zhang, G. Xu, J. Chai, H. Du, L. Wang, H. Wen, X. Zang, A. Du, Q. Jia, X. Zhou, G. Cui, A multifunctional polymer electrolyte enables ultra-long cycle-life in a high-voltage lithium metal battery, Energy Environ. Sci. 11(5) (2018) 1197-1203.

[87] F. Huang, G. Singer, Y. Zhou, Z. Sha, J. Chen, Z. Han, S.A. Brown, J. Zhang, C.H. Wang, Creating ionic pathways in solid-state polymer electrolyte by using PVA-coated carbon nanofibers, Compos. Sci. Technol. 207 (2021).

[88] G.-H. Dong, Y.-Q. Mao, G.-M. Yang, Y.-Q. Li, S.-F. Song, C.-H. Xu, P. Huang, N. Hu, S.-Y. Fu, High-Strength Poly(ethylene oxide) Composite Electrolyte Reinforced with Glass Fiber and Ceramic Electrolyte Simultaneously for Structural Energy Storage, ACS Appl. Energy Mater. 4(4) (2021) 4038-4049.

[89] D. Safanama, S.W. Chien, K. Jenssen, M.Y. Tan, N. Ding, D.W.H. Fam, Fibre-reinforced multifunctional composite solid electrolytes for structural batteries, Compos. Sci. Technol. 241 (2023).

[90] M. Wang, A. Emre, S. Tung, A. Gerber, D. Wang, Y. Huang, V. Cecen, N.A. Kotov, Biomimetic Solid-State Zn(2+) Electrolyte for Corrugated Structural Batteries, ACS Nano 13(2) (2019) 1107-1115.

[91] H. Zhou, Y. Su, J. Zhang, H. Li, L. Zhou, H. Huang, A novel embedded all-solid-state composite structural supercapacitor based on activated carbon fiber electrode and carbon fiber reinforced polymer matrix, Chem. Eng. J. 454 (2023).

[92] X. Liu, H. Li, J. Wang, Q. Han, C. Liu, Achieving mechanically sturdy properties and high energy density for Zn-ion structural batteries based on carbon-fiber-reinforced composites, Compos. Sci. Technol. 218 (2022).

[93] R. Pejman, J. Gorman, A.R. Najafi, Multi-physics design of a new battery packaging for electric vehicles utilizing multifunctional composites, Composites, Part B 237 (2022).

[94] B. Nie, M. Li, T. Yao, H. Yang, L. Duan, J. Zhang, G. Xin, T. Liu, H. Sun, J. Lian, Alignment does matter: Design thick electrodes to improve the comprehensive lithium storage performance, Carbon 206 (2023) 105-113.

[95] J. Xu, Z. Geng, M. Johansen, D. Carlstedt, S. Duan, T. Thiringer, F. Liu, L.E. Asp, A multicell structural battery composite laminate, EcoMat 4(3) (2022).

[96] J. Zhang, J. Yan, Y. Zhao, Q. Zhou, Y. Ma, Y. Zi, A. Zhou, S. Lin, L. Liao, X. Hu, H. Bai, High-strength and machinable load-bearing integrated electrochemical capacitors based on polymeric solid electrolyte, Nat. Commun. 14(1) (2023) 64.

[97] H. Zhou, A. Duongthipthewa, J. Zhang, H. Li, L. Peng, Y. Fu, H. Huang, L. Zhou, A composite structural supercapacitor based on Ni–Co-layered double hydroxide–coated carbon cloth electrodes, Compos. Sci. Technol. 240 (2023).

[98] E. Senokos, Y. Ou, J.J. Torres, F. Sket, C. Gonzalez, R. Marcilla, J.J. Vilatela, Energy storage in structural composites by introducing CNT fiber/polymer electrolyte interleaves, Sci. Rep. 8(1) (2018) 3407.

[99] P. Liu, E. Sherman, A. Jacobsen, Design and fabrication of multifunctional structural batteries, J. Power Sources 189(1) (2009) 646-650.

[100] B.K. Deka, A. Hazarika, O. Kwon, D. Kim, Y.-B. Park, H.W. Park, Multifunctional enhancement of woven carbon fiber/ZnO nanotube-based structural supercapacitor and polyester resin-domain solid-polymer electrolytes, Chem. Eng. J. 325 (2017) 672-680.

[101] W. Chen, X. Yang, T. Huang, Y. Li, X. Ren, S. Ye, Q. Zhang, J. Liu, Constructing flexible composite electrodes of low crystalline cobalt (Oxy)hydroxides nanosheet grown on carbon fiber cloth via self-reconstruction for electrochemical nitrate-to-ammonia conversion, Compos. Commun. 43 (2023).

[102] F. Mo, G. Liang, Q. Meng, Z. Liu, H. Li, J. Fan, C. Zhi, A flexible rechargeable aqueous zinc manganese-dioxide battery working at −20 °C, Energy Environ. Sci. 12(2) (2019) 706-715.

[103] Q. Liu, Z. Yu, Q. Zhuang, J.K. Kim, F. Kang, B. Zhang, Anti-Fatigue Hydrogel Electrolyte for All-Flexible Zn-Ion Batteries, Adv. Mater. 35(36) (2023).

[104] B. Wu, W. Lu, A consistently coupled multiscale mechanical–electrochemical battery model with particle interaction and its validation, J. Mech. Phys. Solids 125 (2019) 89-111.

[105] Z. Hong, Z. Hu, R. Yang, J. You, Y. Fu, L. Zhou, S. Yin, Multiphysics modeling framework for composite structural batteries with modified carbon fibers as electrodes, Compos. Commun. 27 (2021).

[106] U.K. Komal, A.H. Siddiqui, A. Tewari, Investigation of the structural performance and failure mechanisms of 3D printed continuous carbon fiber-based composites, Polym. Compos. 46(9) (2025) 8597-8613.

[107] S.H.B. E. K. Njim, M. Al-Waily, A study on the influence of stress ratio and loading mode on fatigue life characteristics of porous functionally graded polymeric materials, Int. J. Energy Environ. no. 2(12) (2021) 115.

[108] F. Neese, The ORCA program system, WIREs Comput. Mol. Sci. 2(1) (2011) 73-78.

[109] S. Grimme, J. Antony, S. Ehrlich, H. Krieg, A consistent and accurateab initioparametrization of density functional dispersion correction (DFT-D) for the 94 elements H-Pu, The Journal of Chemical Physics 132(15) (2010).

[110] F. Weigend, R. Ahlrichs, Balanced basis sets of split valence, triple zeta valence and quadruple zeta valence quality for H to Rn: Design and assessment of accuracy, Physical Chemistry Chemical Physics 7(18) (2005).

[111] N. Shirshova, A. Bismarck, S. Carreyette, Q.P.V. Fontana, E.S. Greenhalgh, P. Jacobsson, P. Johansson, M.J. Marczewski, G. Kalinka, A.R.J. Kucernak, J. Scheers, M.S.P. Shaffer, J.H.G. Steinke, M. Wienrich, Structural supercapacitor electrolytes based on bicontinuous ionic liquid–epoxy resin systems, J. Mater. Chem. A 1(48) (2013).

[112] T. Khadiran, M.Z. Hussein, Z. Zainal, R. Rusli, Advanced energy storage materials for building applications and their thermal performance characterization: A review, Renewable Sustainable Energy Rev. 57 (2016) 916-928.

[113] N. Shirshova, H. Qian, M. Houlle, J.H. Steinke, A.R. Kucernak, Q.P. Fontana, E.S. Greenhalgh, A. Bismarck, M.S. Shaffer, Multifunctional structural energy storage composite supercapacitors, Faraday Discuss. 172 (2014) 81-103.

[114] A. Javaid, K.K.C. Ho, A. Bismarck, J.H.G. Steinke, M.S.P. Shaffer, E.S. Greenhalgh, Carbon fibre-reinforced poly(ethylene glycol) diglycidylether based multifunctional structural supercapacitor composites for electrical energy storage applications, J. Compos. Mater. 50(16) (2015) 2155-2163.

[115] N. Lingappan, S. Lim, G.-H. Lee, H.T. Tung, V.H. Luan, W. Lee, Recent advances on fiber-reinforced multifunctional composites for structural supercapacitors, Funct. Compos. Struct. 4(1) (2022).

[116] N. Shirshova, A. Bismarck, E.S. Greenhalgh, P. Johansson, G. Kalinka, M.J. Marczewski, M.S.P. Shaffer, M. Wienrich, Composition as a Means To Control Morphology and Properties of Epoxy Based Dual-Phase Structural Electrolytes, The Journal of Physical Chemistry C 118(49) (2014) 28377-28387.

[117] K.-Y. Chan, B. Jia, H. Lin, N. Hameed, J.-H. Lee, K.-T. Lau, A critical review on multifunctional composites as structural capacitors for energy storage, Compos. Struct. 188 (2018) 126-142.

[118] J. Galos, C. Fredriksson, R. Das, Multifunctional sandwich panel design with lithium-ion polymer batteries, Journal of Sandwich Structures & Materials 23(8) (2020) 3794-3813.

[119] M.Y. Tan, D. Safanama, S.S. Goh, J.Y.C. Lim, C.H. Lee, J.C.C. Yeo, W. Thitsartarn, M. Srinivasan, D.W.H. Fam, Concepts and Emerging Trends for Structural Battery Electrolytes, Chem Asian J 17(21) (2022) e202200784.

[120] J. Xu, G. Lindbergh, J. Varna, Multiphysics modeling of mechanical and electrochemical phenomena in structural composites for energy storage: Single carbon fiber micro-battery, J. Reinf. Plast. Compos. 37(10) (2018) 701-715.

[121] D. Carlstedt, E. Marklund, L.E. Asp, Effects of state of charge on elastic properties of 3D structural battery composites, Compos. Sci. Technol. 169 (2019) 26-33.

[122] G. Bucci, T. Swamy, Y.-M. Chiang, W.C. Carter, Modeling of internal mechanical failure of all-solid-state batteries during electrochemical cycling, and implications for battery design, J. Mater. Chem. A 5(36) (2017) 19422-19430.

[123] Y. Xiong, J. Hu, X. Nie, D. Wei, N. Zhang, S. Peng, X. Dong, Y. Li, P. Fang, One-step firing of carbon fiber and ceramic precursors for high performance electro-thermal composite: Influence of graphene coating, Mater. Des. 191 (2020).

[124] W. Dong, J.L. Shi, T.S. Wang, Y.X. Yin, C.R. Wang, Y.G. Guo, 3D zinc@carbon fiber composite framework anode for aqueous Zn-MnO(2) batteries, RSC Adv. 8(34) (2018) 19157-19163.

[125] H. Okuda, R.J. Young, D. Wolverson, F. Tanaka, G. Yamamoto, T. Okabe, Investigating nanostructures in carbon fibres using Raman spectroscopy, Carbon 130 (2018) 178-184.

[126] B. Dilasari, Y. Jung, K. Kwon, Effect of water on the stability of zinc in 1-butyl-1-methylpyrrolidinium bis(trifluoromethylsulfonyl)imide ionic liquid, J. Ind. Eng. Chem. 45 (2017) 375-379.

[127] D. Xu, D. Fan, W. Shen, Catalyst-free direct vapor-phase growth of Zn1-xCuxO micro-cross structures and their optical properties, Nanoscale Res. Lett. 8(1) (2013) 46.

[128] J. Sun, V. Gargitter, S. Pei, T. Wang, Y. Yan, S.G. Advani, L. Wang, T.-W. Chou,

Mechanical and electrochemical performance of hybrid laminated structural composites with carbon fiber/ solid electrolyte supercapacitor interleaves, Compos. Sci. Technol. 196 (2020).

[129] M.H. Kjell, E. Jacques, D. Zenkert, M.r. Behm, G.r. Lindbergh, PAN-Based Carbon Fiber Negative Electrodes for Structural Lithium-Ion Batteries, J. Electrochem. Soc. 158(12) (2011).

[130] N.S. Hudak, A.D. Schlichting, K. Eisenbeiser, Structural Supercapacitors with Enhanced Performance Using Carbon Nanotubes and Polyaniline, J. Electrochem. Soc. 164(4) (2017) A691-A700.

[131] M.H. Kjell, E. Jacques, D. Zenkert, M. Behm, G. Lindbergh, PAN-Based Carbon Fiber Negative Electrodes for Structural Lithium-Ion Batteries, J. Electrochem. Soc. 158(12) (2011) A1455-A1460.

[132] Y. Yan, R.-S. Kühnel, A. Remhof, L. Duchêne, E.C. Reyes, D. Rentsch, Z. Łodziana, C. Battaglia, A Lithium Amide-Borohydride Solid-State Electrolyte with Lithium-Ion Conductivities Comparable to Liquid Electrolytes, Advanced Energy Materials 7(19) (2017) 1700294.

[133] S. Yin, Z. Hong, Z. Hu, B. Liu, X. Gao, Y. Li, J. Xu, Fabrication and multiphysics modeling of modified carbon fiber as structural anodes for lithium-ion batteries, J. Power Sources 476 (2020).

[134] F. Santos, J.P. Tafur, J. Abad, A.J. Fernández Romero, Structural modifications and ionic transport of PVA-KOH hydrogels applied in Zn/Air batteries, J. Electroanal. Chem. 850 (2019).

[135] E.K. Njim, Sadeq H. Bakhy, A study on the influence of stress ratio and loading mode on fatigue life characteristics of porous functionally graded polymeric materials, Int. J. Energy Environ. (12.2) (2021) 115-128.

[136] C. Liu, F. Li, L.P. Ma, H.M. Cheng, Advanced materials for energy storage, Adv. Mater. 22(8) (2010) E28-62.

[137] Y. Miao, P. Hynan, A. von Jouanne, A. Yokochi, Current Li-Ion Battery Technologies

in Electric Vehicles and Opportunities for Advancements, Energies 12(6) (2019).

[138] Y. Chen, A. Amiri, J.G. Boyd, M. Naraghi, Promising Trade-Offs Between Energy Storage and Load Bearing in Carbon Nanofibers as Structural Energy Storage Devices, Adv. Funct. Mater. 29(33) (2019).

[139] W. Zschiebsch, Y. Sturm, M. Kucher, D.P. Hedayati, T. Behnisch, N. Modler, R. Bohm, Multifunctionality Analysis of Structural Supercapacitors- A Review, Materials (Basel) 17(3) (2024).

[140] K.C.S. Lakshmi, B. Vedhanarayanan, High-Performance Supercapacitors: A Comprehensive Review on Paradigm Shift of Conventional Energy Storage Devices, Batteries 9(4) (2023).

[141] H. Zhang, J. Zhang, X. Gao, L. Wen, W. Li, D. Zhao, Advances in materials and structures of supercapacitors, Ionics 28(2) (2021) 515-531.

[142] S. Kumar, S. Kumar, Compulsive Use of Social Media and Unrestrained Buying Behavior: Delineating the Role of Social Comparison, Fear of Missing Out and Self Esteem, Journal of Internet Commerce 23(4) (2024) 503-532.

[143] F. Khan, N. Hossain, J.J. Mim, S.M.M. Rahman, M.J. Iqbal, M. Billah, M.A. Chowdhury, Advances of composite materials in automobile applications – A review, Journal of Engineering Research 13(2) (2025) 1001-1023.

[144] A. Pradysti, H.J. Kim, W.J. Hyun, M.H. Kim, Synthesis of Pd–AuAg trimetal nanohybrids with controlled heterostructures and their application in the continuous flow catalytic reduction of Cr(vi), J. Mater. Chem. A 11(21) (2023) 11388-11400.

[145] Y. Zhang, J. Ma, A.K. Singh, L. Cao, J. Seo, C.D. Rahn, C.E. Bakis, M.A. Hickner, Multifunctional structural lithium-ion battery for electric vehicles, J. Intell. Mater. Syst. Struct. 28(12) (2017) 1603-1613.

[146] S.C. Roberts, G.S. Aglietti, Structural performance of a multifunctional spacecraft structure based on plastic lithium-ion batteries, Acta Astronaut. 67(3-4) (2010) 424-439.

[147] H. Ren, E.S. Takeuchi, A.C. Marschilok, K.J. Takeuchi, E. Reichmanis, Enhancing

composite electrode performance: insights into interfacial interactions, Chem Commun (Camb) 60(15) (2024) 1979-1998.

[148] X. Pu, S. Zhang, D. Zhao, Z.-L. Xu, Z. Chen, Y. Cao, Building the Robust Fluorinated Electrode–Electrolyte Interface in Rechargeable Batteries: From Fundamentals to Applications, Electrochem. Energy Rev. 7(1) (2024).

[149] B. Feng, J. Cao, Y. Wang, J. Feng, Enhanced Adhesive Bonding Based on Surface Modification with Silicon Nanowire Arrays, ECS J. Solid State Sci. Technol. 5(2) (2015) P41-P46.

[150] H.-Y. Lee, Y.-H. Kim, Y.-K. Chang, Fracture behaviors of nanowire-coated metal/polymer systems under mode-I loading condition, Acta Mater. 52(20) (2004) 5815-5828.

[151] Y.C. Wang, Deflection of Steel-Concrete Composite Beams with Partial Shear Interaction, J. Struct. Eng. 124(10) (1998) 1159-1165.

[152] Y. Zhou, X. Cheng, B. Tynan, Z. Sha, F. Huang, M.S. Islam, J. Zhang, A.N. Rider, L. Dai, D. Chu, D.-W. Wang, Z. Han, C.-H. Wang, High-performance hierarchical MnO2/CNT electrode for multifunctional supercapacitors, Carbon 184 (2021) 504-513.

[153] N. Muralidharan, E. Teblum, A.S. Westover, D. Schauben, A. Itzhak, M. Muallem, G.D. Nessim, C.L. Pint, Carbon Nanotube Reinforced Structural Composite Supercapacitor, Sci. Rep. 8(1) (2018) 17662.

[154] M.H. Ryou, J. Kim, I. Lee, S. Kim, Y.K. Jeong, S. Hong, J.H. Ryu, T.S. Kim, J.K. Park, H. Lee, J.W. Choi, Mussel-inspired adhesive binders for high-performance silicon nanoparticle anodes in lithium-ion batteries, Adv. Mater. 25(11) (2013) 1571-6.

[155] Z. Chen, L. Christensen, J.R. Dahn, Large-volume-change electrodes for Li-ion batteries of amorphous alloy particles held by elastomeric tethers, Electrochem. Commun. 5(11) (2003) 919-923.

[156] E.S. Greenhalgh, J. Ankersen, L.E. Asp, A. Bismarck, Q.P.V. Fontana, M. Houlle, G. Kalinka, A. Kucernak, M. Mistry, S. Nguyen, H. Qian, M.S.P. Shaffer, N. Shirshova, J.H.G. Steinke, M. Wienrich, Mechanical, electrical and microstructural characterisation of

multifunctional structural power composites, J. Compos. Mater. 49(15) (2014) 1823-1834.

[157] H. Qian, A.R. Kucernak, E.S. Greenhalgh, A. Bismarck, M.S.P. Shaffer, Multifunctional Structural Supercapacitor Composites Based on Carbon Aerogel Modified High Performance Carbon Fiber Fabric, ACS Appl. Mater. Interfaces 5(13) (2013) 6113-6122.

[158] A. Javaid, O. Khalid, A. Shakeel, S. Noreen, Multifunctional structural supercapacitors based on polyaniline deposited carbon fiber reinforced epoxy composites, J. Energy Storage 33 (2021).

[159] A. Ganguly, A. Karakassides, J. Benson, S. Hussain, P. Papakonstantinou, Multifunctional Structural Supercapacitor Based on Urea-Activated Graphene Nanoflakes Directly Grown on Carbon Fiber Electrodes, ACS Appl. Energy Mater. 3(5) (2020) 4245-4254.

[160] E. Senokos, Y. Ou, J.J. Torres, F. Sket, C. González, R. Marcilla, J.J. Vilatela, Energy storage in structural composites by introducing CNT fiber/polymer electrolyte interleaves, Sci. Rep. 8(1) (2018).

[161] B.K. Deka, A. Hazarika, J. Kim, N. Kim, H.E. Jeong, Y.-B. Park, H.W. Park, Bimetallic copper cobalt selenide nanowire-anchored woven carbon fiber-based structural supercapacitors, Chem. Eng. J. 355 (2019) 551-559.

[162] O. Kwon, B.K. Deka, J. Kim, H.W. Park, Electrochemical performance evaluation of tin oxide nanorod-embedded woven carbon fiber composite supercapacitor, Int. J. Energy Res. 42(2) (2018) 490-498.

[163] N. Shirshova, H. Qian, M.S.P. Shaffer, J.H.G. Steinke, E.S. Greenhalgh, P.T. Curtis, A. Kucernak, A. Bismarck, Structural composite supercapacitors, Composites, Part A 46 (2013) 96-107.

[164] X. Liu, J. Li, Y. Liu, L. Zhou, Achieving enhanced multifunctional performance for structural composite supercapacitors by reinforcing interfaces with polymer coating, J. Colloid Interface Sci. 665 (2024) 603-612.

[165] M. Heidari-Rarani, M. Sayedain, Finite element modeling strategies for 2D and 3D delamination propagation in composite DCB specimens using VCCT, CZM and XFEM

approaches, Theor. Appl. Fract. Mech. 103 (2019).

[166] K. Liu, Y. Liu, D. Lin, A. Pei, Y. Cui, Materials for lithium-ion battery safety, Sci. Adv. 4(6) (2018).

[167] C. González, J.J. Vilatela, J.M. Molina-Aldareguía, C.S. Lopes, J. Llorca, Structural composites for multifunctional applications: Current challenges and future trends, Prog. Mater Sci. 89 (2017) 194-251.

[168] R. Chaudhary, J. Xu, Z. Xia, L.E. Asp, Unveiling the Multifunctional Carbon Fiber Structural Battery (Adv. Mater. 48/2024), Adv. Mater. 36(48) (2024).

[169] Q. Li, D. Wang, B. Yan, Y. Zhao, J. Fan, C. Zhi, Dendrite Issues for Zinc Anodes in a Flexible Cell Configuration for Zinc-Based Wearable Energy-Storage Devices, Angew. Chem. Int. Ed. 61(25) (2022).

[170] P. Zou, R. Zhang, L. Yao, J. Qin, K. Kisslinger, H. Zhuang, H.L. Xin, Ultrahigh-Rate and Long-Life Zinc–Metal Anodes Enabled by Self-Accelerated Cation Migration, Adv. Energy Mater. 11(31) (2021).

[171] J. Feng, D. Ma, K. Ouyang, M. Yang, Y. Wang, J. Qiu, T. Chen, J. Zhao, B. Yong, Y. Xie, H. Mi, L. Sun, C. He, P. Zhang, Multifunctional MXene-Bonded Transport Network Embedded in Polymer Electrolyte Enables High-Rate and Stable Solid-State Zinc Metal Batteries, Adv. Funct. Mater. 32(45) (2022).

[172] B. Zhang, Y. Su, Y. Chen, S. Qi, M. Li, W. Zou, G. Jiang, W. Zhang, Y. Gao, C. Pan, H. Song, Z. Cui, C. Zhang, Z. Liang, L. Du, A Dielectric MXene-Induced Self-Built Electric Field in Polymer Electrolyte Triggering Fast Lithium-Ion Transport and High-Voltage Cycling Stability, Angew. Chem. Int. Ed. 63(25) (2024).

[173] A. Javaid, M. Irfan, Multifunctional structural supercapacitors based on graphene nanoplatelets/carbon aerogel composite coated carbon fiber electrodes, Mater. Res. Express 6(1) (2018).

[174] E. Senokos, D.B. Anthony, N. Rubio, M.C. Ribadeneyra, E.S. Greenhalgh, M.S.P. Shaffer, Robust Single-Walled Carbon Nanotube-Infiltrated Carbon Fiber Electrodes for

Structural Supercapacitors: from Reductive Dissolution to High Performance Devices, Adv. Funct. Mater. 33(16) (2023).

[175] Y. Zhao, H. Xu, G. Cai, C. Yan, D. Liu, G. Chen, Y. Zhu, Multi-functional structural supercapacitor based on manganese oxide-hydroxide nanowires modified carbon fiber fabric electrodes, Polym. Compos. 43(11) (2022) 8458-8470.

[176] J. Huang, Y. Hu, J. Li, H. Wang, T. Wang, H. Wu, Y. Li, M. Wang, J. Zhang, A Flexible Supercapacitor with High Energy Density Driven by MXene/Deep Eutectic Solvent Gel Polyelectrolyte, ACS Energy Lett. 8(5) (2023) 2316-2324.

[177] R.K. Mishra, G.J. Choi, H.J. Choi, J. Singh, F.S. Mirsafi, H.-G. Rubahn, Y.K. Mishra, S.H. Lee, J.S. Gwag, Voltage holding and self-discharge phenomenon in ZnO-Co3O4 core-shell heterostructure for binder-free symmetric supercapacitors, Chem. Eng. J. 427 (2022).

[178] T. Xu, H. Du, H. Liu, W. Liu, X. Zhang, C. Si, P. Liu, K. Zhang, Advanced Nanocellulose-Based Composites for Flexible Functional Energy Storage Devices, Adv. Mater. 33(48) (2021).

[179] N.A. Chernova, M.F.V. Hidalgo, C. Kaplan, K. Lee, I. Buyuker, C. Siu, B. Wen, J. Ding, M. Zuba, K.M. Wiaderek, I.D. Seymour, S. Britto, L.F.J. Piper, S.P. Ong, K.W. Chapman, C.P. Grey, M.S. Whittingham, Vanadyl Phosphates AxVOPO4 (A = Li, Na, K) as Multielectron Cathodes for Alkali-Ion Batteries, Adv. Energy Mater. 10(47) (2020).

[180] Y. Zhou, H. Qi, J. Yang, Z. Bo, F. Huang, M.S. Islam, X. Lu, L. Dai, R. Amal, C.H. Wang, Z. Han, Two-birds-one-stone: multifunctional supercapacitors beyond traditional energy storage, Energy Environ. Sci. 14(4) (2021) 1854-1896.

[181] F. Rubino, A. Nisticò, F. Tucci, P. Carlone, Marine Application of Fiber Reinforced Composites: A Review, J. Mar. Sci. Eng. 8(1) (2020).

[182] M. Song, H. Tan, D. Chao, H.J. Fan, Recent Advances in Zn-Ion Batteries, Adv. Funct. Mater. 28(41) (2018).

[183] J. Lu, X. Zhong, X. Lin, J. Gui, M. Zheng, Y. Liu, Y. Liang, Nanoconfined carbonization enabling high-density porous carbon for jointly superior gravimetric and volumetric zinc-ion

storage, Energy Environ. Sci. 17(18) (2024) 6833-6843.

[184] R.M. Kumar, P. Baskar, K. Balamurugan, S. Das, V. Subramanian, On the Perturbation of the H-Bonding Interaction in Ethylene Glycol Clusters upon Hydration, The Journal of Physical Chemistry A 116(17) (2012) 4239-4247.

[185] Y. Shang, C. Wu, C. Hang, H. Lu, Q. Wang, Hofmeister-Effect-Guided Ionohydrogel Design as Printable Bioelectronic Devices, Adv. Mater. 32(30) (2020).

[186] R. Chaudhary, J. Xu, Z. Xia, L.E. Asp, Unveiling the Multifunctional Carbon Fiber Structural Battery, Adv. Mater. 36(48) (2024).

[187] B.K. Deka, A. Hazarika, M.-J. Kwak, D.C. Kim, A.P. Jaiswal, H.G. Lee, J. Seo, C. Jeong, J.-H. Jang, Y.-B. Park, H.W. Park, Triboelectric nanogenerator-integrated structural supercapacitor with in situ MXene-dispersed N-doped Zn–Cu selenide nanostructured woven carbon fiber for energy harvesting and storage, Energy Storage Mater. 43 (2021) 402-410.

[188] J.F. Snyder, E.B. Gienger, E.D. Wetzel, Performance metrics for structural composites with electrochemical multifunctionality, J. Compos. Mater. 49(15) (2015) 1835-1848.

[189] H. Qian, A.R. Kucernak, E.S. Greenhalgh, A. Bismarck, M.S. Shaffer, Multifunctional structural supercapacitor composites based on carbon aerogel modified high performance carbon fiber fabric, ACS Appl. Mater. Interfaces 5(13) (2013) 6113-22.